

Large Eddy Simulation of Flow around Bridge Abutments



Ken Vui Chua

School of Engineering

Cardiff University, Wales, UK

Supervised by:

Prof. Thorsten Stoesser

This thesis is submitted in partial fulfilment of the requirements
for the degree of

Doctor of Philosophy (Ph.D.)

2018

DECLARATION

This work has not been submitted in substance for any other degree or award at this or any other university or place of learning, nor is being submitted concurrently in candidature for any degree or other award.

Signed (candidate) Date

STATEMENT 1

This thesis is being submitted in partial fulfilment of the requirements for the degree of PhD.

Signed (candidate) Date

STATEMENT 2

This thesis is the result of my own independent work/investigation, except where otherwise stated, and the thesis has not been edited by a third party beyond what is permitted by Cardiff Universitys Policy on the Use of Third Party Editors by Research Degree Students. Other sources are acknowledged by explicit references. The views expressed are my own.

Signed (candidate) Date

STATEMENT 3

I hereby give consent for my thesis, if accepted, to be available online in the Universitys Open Access repository and for inter-library loan, and for the title and summary to be made available to outside organisations.

Signed (candidate) Date

Acknowledgements

First of all, I would like express my sincere and deepest gratitude to my supervisor Professor Thorsten Stoesser for giving me this research opportunity four years ago. I always consider myself lucky to be able to work under Prof. Stoesser during my MSc project, which subsequently landed me this PhD opportunity. Prof. Stoesser trusted, supported, and motivated me through my ups and downs over the years, flooding me with his immense knowledge and experience in hydraulic engineering. This thesis without his guidance would not exist in its present form.

I am very grateful to my workmates who assisted and guided me through countless hours of code learning and post-processing. Special thanks to Pablo Ouro, Bruño Fraga and Richard McSherry for their generous support and great patience over the years. My research journey without their help would be unimaginably difficult and clueless.

Many thanks to the American Association of State Highway and Transportation Officials (AASHTO) and Federal Highway Administration for their generous sponsor towards this work. I would like to acknowledge the support of the Supercomputing Wales project, which provided all the supercomputing power required in this project.

Special thanks to my girlfriend, Sarah Chin for being the best companion and supporter during this long journey. Last but not least, I am very thankful to my parents in Malaysia, Chua Yong Chiang and Chan Sau Mui, for giving me the freedom and support I needed to pursue my dreams while being far away from home for so many years. Also, my greatest appreciation to my siblings, Sylvia, Alex,

and Cadee for taking care of my parents while I am away. Their unlimited support towards this youngest member of the family has been the key of my accomplishments. Thank you very much.

Cardiff, 2018

Ken Vui Chua

Abstract

Extreme hydrological events have increased the frequency of flooding scenarios in recent years, resulting in significant bridge inundation and associated damages. Turbulence structures within the flow field are highly energetic and possess high sediment entrainment capacity which will lead to the scour formation around the bridge foundation and consequently causes structural instability or even failure of the structure. This research employs the method of Large Eddy Simulation (LES) to elucidate the complex flow mechanisms around bridge abutments in changing conditions. The level set method (LSM) is adopted in LES code to predict the complex water surface profiles and an extensive validation of the method against complementary experiment is presented. A faithful representation of a natural river which consists of an asymmetrical compound channel with a parabolic main channel and two variable-length abutments with sloped sidewalls and rounded corners, and a bridge deck is presented in this thesis. The LES code is used to analyse the effect of bridge abutment length on the turbulence structure and flow field through the bridge opening. Extensive analysis by means of streamwise velocity contours, 2D and 3D streamlines, isosurfaces of Q-criterion, contours of wall-normal vorticity, probability density functions, quadrant analysis, power density spectra, and water surface elevation contours has been carried out and have shown significant differences between the different abutment lengths. The findings attempt to contribute to the design of resilient hydraulic structures especially on considering the shape and size of an abutment. The investigation of flow mechanisms around bridge abutments under different scour conditions (i.e. pre-scour and equilibrium scour) is presented in the later part of the thesis. Through 3D streamlines and contours of vertical velocity and turbulent kinetic energy, the equilibrium scour case reveals an increase in the three-dimensionality of the flow around the left abutment in the scour region when compared with the flat bed case. Focusing on the near bed quantities, i.e. bed shear stress and near bed turbulent kinetic energy, the equilibrium scour case shows a significant relaxation at the vicinity of the left abutment, indicating a drastic reduction in sediment activities.

Contents

Declaration	iii
Acknowledgements	vi
Abstract	ix
Contents	ix
Related Publications	xiv
Nomenclature	xiv
List of Figures	xviii
List of Tables	xxiv
1 Introduction	1
1.1 Motivation	1
1.2 Objectives and thesis structure	3
2 Literature Review	8
2.1 Bridge Abutment Hydraulics	8
2.1.1 Horseshoe vortex system	10
2.1.2 Flow contraction	12
2.1.3 Abutment form	13

2.1.4	Compound channel	14
2.2	Bridge Abutment Scour	16
2.2.1	Sediment transport theory	16
2.2.2	Types of scour at bridge abutment	19
2.2.3	Experimental approach on scour prediction	22
2.2.4	Numerical approach on scour prediction	27
2.3	Free Surface Flow	30
2.3.1	Rigid lid approximation	31
2.3.2	Interface tracking methods	32
2.3.3	Interface capturing methods	35
3	Numerical Framework	41
3.1	Large Eddy Simulation	41
3.2	Governing Equations	42
3.3	Fractional-step method	45
3.4	Level set method	47
3.5	Immersed boundary method	49
4	Level Set Method Validation Case¹	54
4.1	Objectives	54
4.2	Experimental set-up	55
4.3	Numerical setup	58
4.4	Results and Validation	60
4.5	Closure	71
5	The Effect of Bridge Abutment Length on the Turbulence Structure and the Flow Through the Opening²	74
5.1	Motivation and Objectives	74
5.2	Numerical and Experimental Setup	75
5.3	Results and Discussion	77

¹Results from this chapter are directly adopted from the 2nd journal paper listed in the section of related publications.

²Results from this chapter are directly adopted from the 3rd journal paper listed in the section of related publications.

5.3.1	Validation	77
5.3.2	Flow Separation	81
5.3.3	Instantaneous Secondary Flow	87
5.3.4	Shear Layer Oscillation and Vortex Shedding	90
5.4	Closure	103
6	Free Surface Flow around Bridge Abutment on Pre-scour and Equilibrium Scour Condition¹	106
6.1	Motivation and Objectives	106
6.2	Numerical and Experimental Setup	107
6.3	Results and Discussion	109
6.3.1	Validation	109
6.3.2	Flow separation	111
6.3.3	Free surface	115
6.3.4	Bed shear stress	119
6.3.5	Near-bed turbulent kinetic energy	122
6.4	Closure	126
7	Conclusions, contribution of thesis, and outlook	129
7.1	Conclusions	129
7.2	Contributions of Thesis	131
7.3	Outlook	132
	References	135

¹Results from this chapter are directly adopted from the 4th journal paper listed in the section of related publications.

The publications derived from the work undertaken in this thesis are listed as follows:

Journal papers

1. Richard McSherry, **Ken Vui Chua**, Thorsten Stoesser, and Saad Mulahasan. Free surface flow over square bars at intermediate relative submergence. *Journal of Hydraulic Research*, pages 1-19, 2018. ISSN 0022-1686. doi: 10.1080/00221686.2017.1413601
2. Richard McSherry, **Ken Vui Chua**, and Thorsten Stoesser. Large eddy simulation of free-surface flows. *Journal of Hydrodynamics*, pages 1-12, 2017. ISSN 1001-6058. doi: 10.1016/S1001-6058(16)60712-6
3. **Ken Vui Chua**, Bruno Fraga, Thorsten Stoesser, Seungho Hong, and Terry Sturm. The effect of bridge abutment length on the turbulence structure and flow through the opening. *Journal of Hydraulic Engineering*. Accepted. Awaiting publication.
4. **Ken Vui Chua**, Bruno Fraga, Thorsten Stoesser, Seungho Hong, and Terry Sturm. Free surface flow around bridge abutment on pre-scour and equilibrium scour condition. *Journal of Hydraulic Engineering*. Under review.

Reports

1. Terry Sturm, Irfan Abid, Bruce Melville, Xiaozhou Xiong, Thorsten Stoesser, Bruno Fraga Bugallo, **Ken Vui Chua**, Steven Abt, and Seungho Hong. Combining Individual Scour Components to Determine Total Scour. National Cooperative Highway Research Program Report, 2017. Transportation Research Board.

Nomenclature

Abbreviations

CFD	Computational Fluid Dynamics
CFL	Courant-Friedrichs-Lewy
CICSAM	Compressive interface Capturing Scheme for Arbitrary Mesh
CLSVOF	Coupled Level Set Volume of Fluid Method
CV	Corner Vortex
DB	Deformed Bed
DES	Detached Eddy Simulation
DF	Direct Forcing method
DNS	Direct Numerical Simulation
FB	Flat Bed
FCT	Flux-corrected Transport Method
HV	Horseshoe Vortex
IB	Immersed Boundary
IBM	Immersed Boundary Method
IV	Interface Vortex
LCS	Lagrangian Coherent Structure
LES	Large Eddy Simulation
LMR	Local Mesh Refinement
LSB	Long Setback
LSM	Level Set Method
MAC	Marker-and-cell
MV	Main Vortex
NV	Necklace Vortex

PDF	Probability Density Function
PIV	Particle Image Velocimetry
PLIC	Piecewise Linear Interface Calculation
PLSM	Particle Level Set Method
RANS	Reynolds Averaged Navier Stokes
SGS	Sub-Grid Scale
SLIC	Simple Line Interface Calculation
SSB	Short Setback
SSL	Separated Shear Layer
SV	Surface Vortex
TKE	turbulent kinetic energy
URANS	Unsteady Reynolds Averaged Navier Stokes
VOF	Volume of Fluid
WALE	Wall-adapting Local Eddy viscosity model
WENO	Weighted, Essentially Non-oscillatory scheme

Dimensionless parameters

Fr	Froude number
Re	Reynolds number

Greek Symbols

α	maximum angle of inclined surface with the horizontal
ϵ	half of interface thickness
Γ	gas-liquid interface
γ	specific weight of fluid
γ_s	specific weight of sediment
λ	bar spacings
μ	dynamic viscosity
ν	kinematic viscosity
ν_τ	eddy viscosity
ω	vorticity
Ω_{gas}	gas domain
Ω_{liquid}	fluid domain
ϕ	level set signed distance function
ρ	density

ρ_s	density of sediment
σ_g	grain size distribution
τ_c	critical shear stress for incipient sediment motion
$\tau_{*c,0}$	critical shear stress for incipient sediment motion on a flat bed
τ_{*c}	Shields parameter
τ_{ij}	SGS stress
θ	angle of repose for the sediment

Roman Symbols

H	heaviside function
B	channel width
B_f	width of left floodplain
B_m	Main channel width
D	water depth
d_*	dimensionless grain diameter
d_{50}	median sediment grain size
F_L	Lagrangian force
g	gravitational acceleration
H_b	Distance from initial bed to the bridge low chord in floodplain
k	roughness height
K_d	Sediment size factor
k_f	Roughness height of floodplain
K_G	Channel geometry factor
K_I	Approach flow intensity factor
k_m	Roughness height of main channel
K_s	Abutment shape factor
K_θ	Factor accounting for the abutment alignment to the flow
K_{yL}	Abutment length factor
L_a	Abutment Length
p	Pressure
Q	Q-criterion
SG	Specific Gravity
t	time
u_*	shear velocity

U_b	Bulk velocity
U_L	Lagrangian velocity
u_{*c}	critical value of shear velocity for initiation of motion
V_1	Approach flow velocity
V_L	Lagrangian volume
V_{c1}	Critical approach velocity
W_e	Width of abutment in flow direction
y_{f1}	Flow depth in the bridge approach section upstream of abutment
y_{fmax}	Maximum depth of flow after scour

Superscripts

$(\cdot)'$	Fluctuation value
$(\cdot)^+$	Variable in wall-units

Subscripts

$(\cdot)_{RMS}$	Root Mean Square
-----------------	------------------

List of Figures

1.1	(a) Contraction scour; (b) Local Abutment Scour; (c) Local Pier Scour; ((a)-(c) Courtesy of U. S. Geological Survey) and (d) Railway bridge failure in Feltham, UK in 2009 caused by local scour (RAIB [2010])	2
1.2	Causes of bridge failures in the United States from 1966-2005. (adapted from Hunt [2009])	4
2.1	Flow around a bridge abutment and embankment in a compound channel. (Ettema et al. [2010])	9
2.2	General pattern of the horseshoe vortex system. (Dargahi [1989]) .	11
2.3	Streamlines of the time-averaged flow over a submerged bridge. (a) Oblique view from behind and (b) in a horizontal plane near the bed (Kara et al. [2015b])	14
2.4	Types of side wall mounted hydraulic structures: (a) spur dike; (b) wing-wall abutment; (c) sloped side-wall abutment; and (d) spill-through abutment with rounded corners	15
2.5	Shields diagram for direct determination of critical shear stress (Sturm [2001])	18
2.6	Time development of clear-water and live-bed scour (Chabert and Engeldinger [1956])	21
2.7	Definition sketch for abutment scour in a compound channel. (Sturm et al. [2011])	25
2.8	Typical cases of abutment positions in compound channels. (Melville and Coleman [2000])	27

2.9	Distribution of normalised turbulent kinetic energy in a horizontal plane near the bed at $z/H = 0.1$ as computed by (a) free-surface-resolved simulation; (b) rigid-lid simulation (Kara et al. [2015a]) .	33
3.1	Concept of Large Eddy Simulation in relation to energy flux and energy spectrum (adapted from Breuer [2002])	43
3.2	Two-dimensional representation of the Cartesian staggered grid. The neighbours used in the interpolation for a Lagrangian marker (filled red circle) are the black-filled symbols within the square boundary. x represents pressure nodes, \square are x-velocity nodes, \circ are y-velocity nodes, and red circles are the Lagrangian markers. ΔV_L denotes the Lagrangian marker volume.	51
4.1	Experimental set-up. (a) the flume equipped with square bars, (b) the two geometries, with velocity measurement locations denoted by dashed lines.	55
4.2	(a) Post-processed camera image from side view and (b) visualisation of 3D instantaneous free surface profiles from side view for LES results, $\lambda/k = 10.4$, $H/k = 2.4$	57
4.3	Computational domain with instantaneous free surface response. (a) $\lambda/k = 5.2$; (b) $\lambda/k = 10.4$	59
4.4	Volume fraction vs height above bed for the six LES cases.	61
4.5	Variation of friction factor with relative submergence for the flume experiments.	62
4.6	Measured and computed longitudinal profiles of temporal and spanwise mean free surface elevation of the six flow cases	64
4.7	Vertical profiles of temporal and spanwise mean streamwise velocity, \bar{u} : $\lambda/k = 5.2$	65
4.8	Vertical profiles of temporal and spanwise mean streamwise velocity, \bar{u} : $\lambda/k = 10.4$	66
4.9	Contours of the temporal and spanwise mean streamwise velocity, normalised on bulk velocity for six cases, C1-C6.	68
4.10	Contours of the temporal and spanwise mean streamfunction for six cases, C1-C6.	70

4.11	Streamwise variation of spanwise mean normalised distance from the wall to the first computational grid point. (a) $\lambda/k = 5.2$; (b) $\lambda/k = 10.4$ The grey shaded regions denote the locations of the bars.	71
5.1	Computational domains: (a) Long-setback abutment case, LSB, (b) Short-setback abutment case, SSB, (c) Cross-section including its dimensions.	78
5.2	Definition sketch of the abutments and bridge area. The intersections between horizontal numbered lines (1-5) and vertical solid (LSB) and dashed (SSB) lines indicate the locations at which time-averaged streamwise velocity profiles (a)-(h) were measured experimentally.	79
5.3	Computed and measured time-averaged streamwise velocity profiles at locations (a)-(h) (as described in Fig. 5.2) in cross-sections 2-4 of the LSB case. Experimental data (circles), coarser-mesh LES (dashed line), and finer-mesh LES (solid line).	80
5.4	Computed and measured time-averaged streamwise velocity profiles at locations [a]-[h] (as described in Fig. 5.2) in cross-sections 2-4 of the SSB case. Experimental data (circles), coarser-mesh LES (dashed line), and finer-mesh LES (solid line).	82
5.5	Computed (solid line) and measured (circles) profiles of the water surface for the LSB case at cross-section 2-4.	83
5.6	Computed (solid line) and measured (circles) profiles of the water surface for the SSB case at cross-section 2-4.	83
5.7	LES-predicted streamwise velocity contours in a selected horizontal plane: (a) instantaneous (b) time-averaged velocity for the LSB case.	84
5.8	LES-predicted streamwise velocity contours in a selected horizontal plane: (a) instantaneous (b) time-averaged velocity for the SSB case.	85
5.9	2D streamlines near the abutment for (a) the LSB case and (b) the SSB case, 3D streamtraces colour-coded with time-averaged streamwise velocity for (c) the LSB case and (d) the SSB case. . .	86

5.10	Isosurfaces of the Q-criterion together with contours of the streamwise vorticity in selected cross-sections: (a) LSB case, (b) SSB case.	89
5.11	Water surface deformation represented by zero level set and colour-coded by water depth for (a) LSB case and (b) SSB case.	90
5.12	LSB case: (a) Locations along the estimated separated shear layer where velocity time signals are recorded. (b) Probability density function of streamwise velocity fluctuation normalised by the root-mean-square of the streamwise velocity fluctuation near the left abutment at all locations and (c) Probability density function of streamwise velocity fluctuation at all location in the vicinity of the right abutment. All sampling data are taken at approximately mid depth of the floodplain.	91
5.13	(a) SSB case: (a) Locations along the estimated separated shear layer where velocity time signals are recorded. (b) Probability density function of streamwise velocity fluctuation normalised by the root-mean-square of the streamwise velocity fluctuation near the left abutment at all locations and (c) Probability density function of streamwise velocity fluctuation at all locations in the vicinity of the right abutment. All sampling data are taken at approximately mid depth of the floodplain.	93
5.14	Quadrant analysis of the streamwise and spanwise velocity fluctuation normalised with u'_{RMS} for the LSB case.	95
5.15	Quadrant analysis of the streamwise and spanwise velocity fluctuation normalised with u'_{RMS} for the SSB case.	95
5.16	Power spectra of a streamwise and spanwise velocity fluctuation time series at location L7: (a) in log-log scale, (b) in semi-log scale, (c) wall-normal vorticity contours in a horizontal plane near the water surface and (d) water surface represented by zero level set colour-coded by the water depth for the LSB case.	97

5.17	Power spectra of a streamwise and spanwise velocity fluctuation time series at location R5: (a) in log-log scale, (b) in semi-log scale, (c) wall-normal vorticity contours in a horizontal plane near the water surface and (d) water surface represented by zero level set colour-coded by the water depth for the LSB case.	99
5.18	Power spectra of a streamwise and spanwise velocity fluctuation time series at location L7: (a) in log-log scale, (b) in semi-log scale, (c) wall-normal vorticity contours in a horizontal plane near the water surface and (d) water surface represented by zero level set colour-coded by the water depth for the SSB case.	100
5.19	Time series of the streamwise velocity at location L7 of the SSB case and streamwise velocity contours at six selected instants in time labeled t_1 - t_6	101
5.20	Power spectra of a streamwise and spanwise velocity fluctuation time series at location R5: (a) in log-log scale, (b) in semi-log scale, (c) wall-normal vorticity contours in a horizontal plane near the water surface and (d) water surface represented by zero level set colour-coded by the water depth for the SSB case.	102
6.1	Computational Setup: (a) Flat bed case, FB; (b) Zoomed-in view of the scour bathymetry near the left abutment colour-coded with depth, z in the deformed bed case, DB. White columns are the markers of locations for the time-averaged streamwise velocity profile comparisons.	110
6.2	Validation of LES time-averaged streamwise velocities with experimental data for FB case near the left abutment; Circle represents experimental data and solid line represents LES; Locations of profiles (a)-(f) are marked in the bottom right sub-figure.	112
6.3	Time-averaged 3D streamtraces colour-coded by time-averaged streamwise velocity; On the left, top-down views of (a) FB and (c) DB; on the right, zoomed-in views of (b) FB and (d) DB, near left abutment.	114

6.4	(a)-(b) Non-dimensional time-averaged vertical velocity contours for FB (left) and DB (right), respectively; (c)-(d) Non-dimensional turbulent kinetic energy contours for FB and DB, respectively; All contours on four XZ slices near left abutment.	116
6.5	Time-averaged streamwise velocity profiles at 20 locations labeled in Fig. 6.1(b) for FB (dashed line) and DB (solid line).	117
6.6	Water surface deformation (represented by zero level set) colour-coded by the normalised water depth, z/h near the left abutment, (a)FB, (b) DB.	119
6.7	Instantaneous water surface profiles at transverse planes (x1)-(x2) and longitudinal planes (y1)-(y2) for FB (solid lines) and DB (circles with solid lines).	120
6.8	Instantaneous (top) and time-averaged (bottom) normalised bed shear stress distribution near the left abutment for FB (left) and DB (right).	122
6.9	Time-averaged normalised bed shear stress profiles at transverse planes(x1)-(x2) and longitudinal planes (y1)-(y2) for FB (solid lines) and DB (circles with solid lines).	123
6.10	Near-bed normalised turbulent kinetic energy distribution near left abutment for (a) FB and (b) DB.	124
6.11	Near-bed normalised turbulent kinetic energy profiles at transverse planes(x1)-(x2) and longitudinal planes (y1)-(y2) for FB (solid lines) and DB (circles with solid lines).	125

List of Tables

2.1	Properties of sediment adopted in this study.	17
2.2	Abutment shape factors, K_s for Melville scour formula.	26
4.1	Hydraulic conditions and computational details.	56

Chapter 1

Introduction

1.1 Motivation

Scour is a natural phenomenon caused by the erosive action of flowing stream on erodible beds. Scour can be categorised into three types namely, general scour, contraction scour and local scour. General scour is the long term aggradation or degradation which represents changes in bottom elevation alongside with a gradual change in the width of the river over a long period of time due to geomorphic adjustments irrespective of the existence of any in-stream structure (e.g. bridge, embankment, abutment, and pier). Contraction scour occurs when a flow is restricted by natural causes such as the narrowing of a natural channel or the existence of any obstruction like an embankment and the resulting flow constriction through the bridge opening. Local scour around the bridge foundation is caused by an obstruction to the flow such as a pier or abutment, and is therefore localised in the immediate vicinity of the obstruction in the main channel and floodplain of the river. Scour will lead to the loss of support at the bridge foundation and consequently may cause the bridge to fail. Photos of contraction scour, local scour (both abutment and pier scours), and a recent railway bridge failure in Feltham, UK are presented in Fig. [1.1](#).

During flood events, the scouring phenomenon at bridge piers and abutments is magnified and has attracted the attentions of engineers and researchers to

1. INTRODUCTION



Figure 1.1: (a) Contraction scour; (b) Local Abutment Scour; (c) Local Pier Scour; ((a)-(c) Courtesy of U. S. Geological Survey) and (d) Railway bridge failure in Feltham, UK in 2009 caused by local scour (RAIB [2010])

take on the challenge of reducing the rate of bridge failures. [Shirole and Holt \[1991\]](#) were one of the earliest research groups to collect data up to 1000 cases of bridge failures over the last 30 years prior to 1991 in the United States and have concluded that 60% of those failures were due to scour at bridge foundations. 500 failures of bridge structures in the United States between 1989 and 2000 were studied by [Wardhana and Hadipriono \[2003\]](#). They found that over 53% bridge failures were attributed to scour due to floods and other hydraulics factors. [Fig. 1.2](#) listed out all the possible causes of the documented bridge failures with their respective percentages from year 1966 to 2005. Out of the 1502 documented bridge failures, 58% were the result of hydraulic conditions, followed substantially behind by collisions (by ships, trucks or trains) and overload ([Hunt \[2009\]](#)). The more recent study of bridge failures by [Lin et al. \[2014\]](#) presented a detailed analysis on 36 bridge failures from New Zealand (20), USA (14) and Canada (2). They found that local scours at abutments and piers account for 64% of the bridge failures while only 4% of the failures were caused by contraction scour. Other factors such as the soil types, foundation types and failure modes related to the cases were also examined.

1.2 Objectives and thesis structure

The main objective of the present research is to better understand the complex hydrodynamics around bridge abutments using the numerical method of large eddy simulation (LES) with an emphasis on visualising the coherent structures around the abutments. By adopting the level set method (LSM) as an interface capturing tool, the water surface deformation are simulated to provide a better understanding of the effect of the abutment length and bed deformation on the water surface. The structure of this thesis is as follows:

- [Chapter 2](#): an extensive literature review is presented for past research works on bridge abutment hydraulics ([Sec. 2.1](#)), bridge abutment scour ([Sec. 2.2](#)), and free surface flow ([Sec. 2.3](#)). In [Sec. 2.1](#), the three-dimensional flow field around a hydraulic structure is described, which is mainly composed of the localised horseshoe vortex system and the contrac-

1. INTRODUCTION

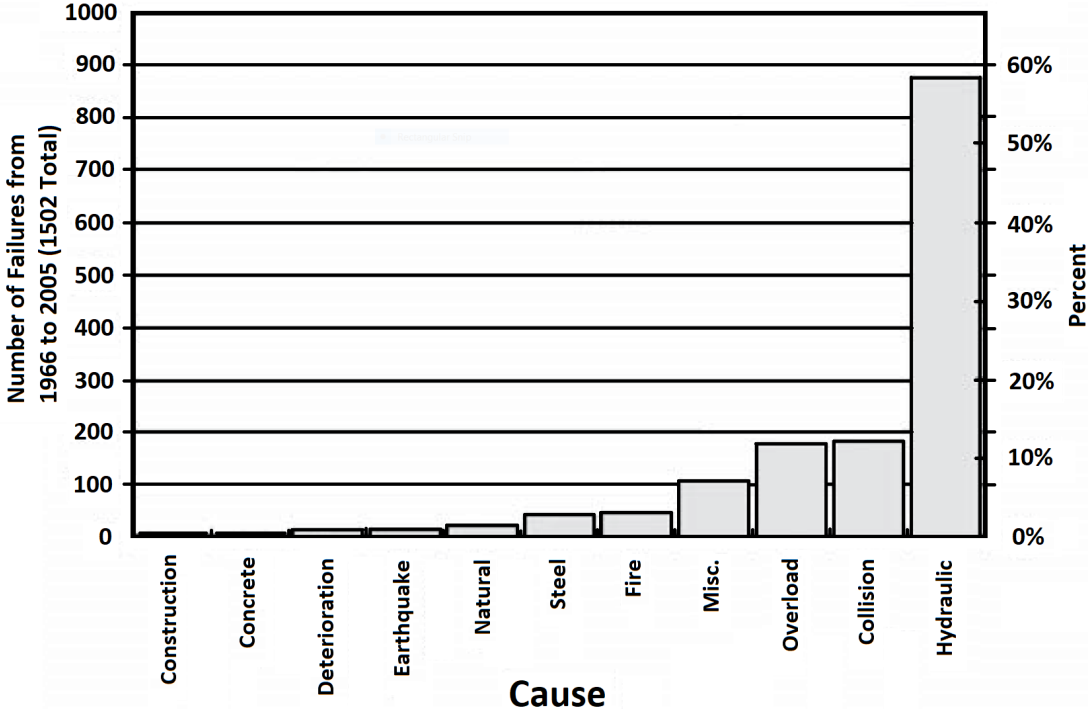


Figure 1.2: Causes of bridge failures in the United States from 1966-2005. (adapted from [Hunt \[2009\]](#))

1. INTRODUCTION

tion flow generated by the large flow blockage in the channel. The following section discusses the types of scour around an abutment, an example of scour prediction formula obtained from experiments and the numerical approach in predicting scour. Lastly, three main numerical approaches on treating the free surface are discussed: the rigid lid approximation, the interface tracking methods and the interface capturing methods.

- Chapter 3: descriptions of the concept of large eddy simulation method is presented. The governing Navier-Stokes equations used in the in-house code HYDRO3D are shown together with the description of the fractional-step method adopted. The level set method, which is used to capture the free surface, is described. Finally, the descriptions of the immersed boundary method employed to represent in-stream bodies are presented.
- Chapter 4: the validity of using level set method as an interface capturing tool for the water surface is investigated. Large eddy simulations and complementary experiments were carried out on six flow cases, with varying relative submergence and roughness types. The LES-computed streamwise velocity profiles and free surface elevations were plotted against the experimental data.
- Chapter 5: large eddy simulations of the turbulent flow around bridge abutments of different lengths are performed. A faithful representation of a natural river is achieved by employing a computational domain that consists of an asymmetrical compound geometry with a parabolic main channel in which two variable-length abutments with sloped sidewalls and round corners are placed. Mean flow patterns between the two abutment configurations are discussed, focusing on the effect of increasing contraction on the extent of the recirculation vortices and the oscillation of the shear layer between this recirculation and main channel flow. Shape, vorticity and periodicity of coherent structures shed by the abutments are highlighted by means of Q-criterion and spectral analysis.
- Chapter 6: large eddy simulations of turbulent flow around bridge abutments in two different scour stages (i.e. pre-scour and equilibrium scour

1. INTRODUCTION

conditions) are carried out. The computational domain consists of an asymmetrical compound geometry with a parabolic main channel and abutments with sloped sidewalls and rounded corners. The only change between the two cases is the bed bathymetry, where a scour hole is present near the left abutment in the equilibrium scour case. The discussion of the changes in mean flow patterns before and after the scour formation is followed by the comparison of free surface undulation patterns between the cases. Near bed quantities including the bed shear stress and near-bed turbulent kinetic energy are presented to highlight the transformation between scour stages.

- Chapter 7: Conclusion of the thesis and outlook of this research are included in this chapter.

1. INTRODUCTION

Chapter 2

Literature Review

2.1 Bridge Abutment Hydraulics

Obstructing a stream with a hydraulic structure (e.g. spur dike, bridge abutment, and bridge pier) creates a very complex three-dimensional (3-D) highly turbulent flow field within the near proximity of the hydraulic structure as a result of the flow deceleration before the flow structure, the downflow at the upstream face of the structure, the separation of the incoming boundary layer, the formation of the separated shear layer (SSL) at the tip of the structure, and the wake flow past it. Figure 2.1 presents a sketch of the turbulent flow around a bridge abutment and embankment in a compound channel (Ettema et al. [2010]). As the flow approach the abutment, first flow separation occurs at the side wall as eddy is formed in the corner between the upstream face of the abutment and side wall, usually known as a corner vortex. The second separation occurs at the tip of the abutment as flow contracts and accelerates. Behind the abutment is the flow separation zone where large eddies exist. The fast flowing contracted flow and the slow rotating eddies behind the abutments induce the separated shear layer (SSL). Within the SSL, vigorous vortex formation happens which creates a region of high turbulence.

Understanding the flow physics around spur dikes, bridge piers, bridge abutments and embankments has been an important research topic in river engineering

2. LITERATURE REVIEW

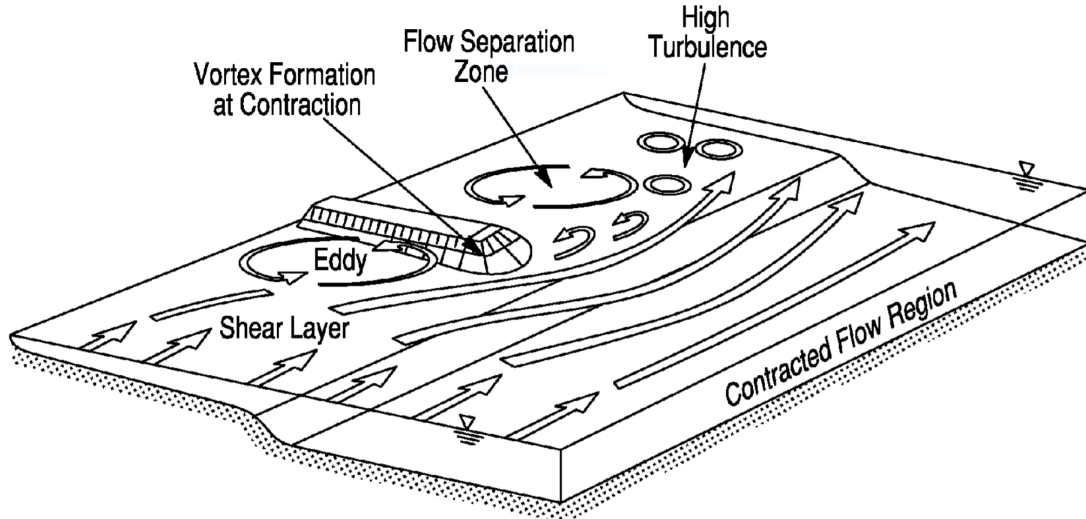


Figure 2.1: Flow around a bridge abutment and embankment in a compound channel. (Ettema et al. [2010])

as it directly links to the scouring process, thus contributing to the prediction of scour evolution and maximum scour depth (Kwan and Melville [1994]; Melville [1997]; Sumer and Fredsøe [2002]). Many studies attempted to predict the scouring pattern and maximum scour depth for different hydraulic conditions and shape of spur dikes/abutment structure (see Barbhuiya and Dey [2004]; Melville [1997] for review). However, these studies failed to explain the intricate flow physics behind the local scouring process, in particular, the roles played individually by the dominant coherent structures as well as their interactions with each other and with the hydraulic structure, at different stages of the scouring process (Koken and Constantinescu [2008a]). The difficulty that earlier experimentalists face is the limitations of experimental techniques (e.g. dye visualisations, free surface flow measurements) used in visualising the coherent structures. These techniques fail to give a clear analysis of the structure of the vortical eddies playing a role in the scouring process. More advanced visualisation method like the particle image velocimetry (PIV) appears to be a more popular method amongst the researchers for its better illustration of the dynamics of these coherent structures, despite its relatively higher costs.

2.1.1 Horseshoe vortex system

The flow and sediment dynamics around the close vicinity of a hydraulic structure is dominated by the coherent structures, also known as the macroturbulent structures. As the flow approaches the in-stream object, as a result of the adverse pressure gradients, the incoming boundary layer separates and necklace-like vortical structures form around the base of the obstacle. These vortices form what is known as the horseshoe vortex (HV) system. Baker [1979, 1980]; Dargahi [1989] were few of the earliest experimental studies which discovered the HV system by investigating the flow field around a vertical cylinder on a flat bed. Fig. 2.2 is the general pattern of the HV system proposed by Dargahi [1989]. The downward flow at the upstream face of the cylinder separates from the surface and a very small vortex in anti-clockwise direction is created, denoted as V1. The flow from the lower part of the boundary layer is turned into a clockwise vortex (V2). V3 is formed as a small triangular anti-clockwise vortex underneath the upstream part of the V2. Shortly after the formation of V2, an instability occurs at its upstream end which grows in size and finally develops into a fourth vortex (V4) rotating in clockwise direction. Subsequent to the formation of V4, V5 develops upstream and close to V4. The quasi-periodic sequence of the vortex formation starts with detachment of V2 and V2 is convected downstream, reducing its cross-sectional area as it is stretched. The HV system is applied not only to cylindrical structures but also wall mounted structures like spur dike and abutment. The difference is that the formation of the V2 follows the junction line between the bed and the upstream part of the structure, and then bends in the direction of the flow as it passes the obstacle.

In realistic cases of river engineering applications, the incoming flow is always fully turbulent, leading to a HV system that is unsteady and subject to large temporal variations in terms of location, size and intensity. Devenport and Simpson [1990] carried out experiments on a surface mounted wing-shaped body and observed significant amplification of the turbulent kinetic energy (*tke*), turbulence production and pressure root-mean-square (RMS) fluctuations within the HV system. Devenport and Simpson [1990] reported the amplifications are attributed to the presence of large-scale, relatively low frequency, aperiodic oscilla-

2. LITERATURE REVIEW

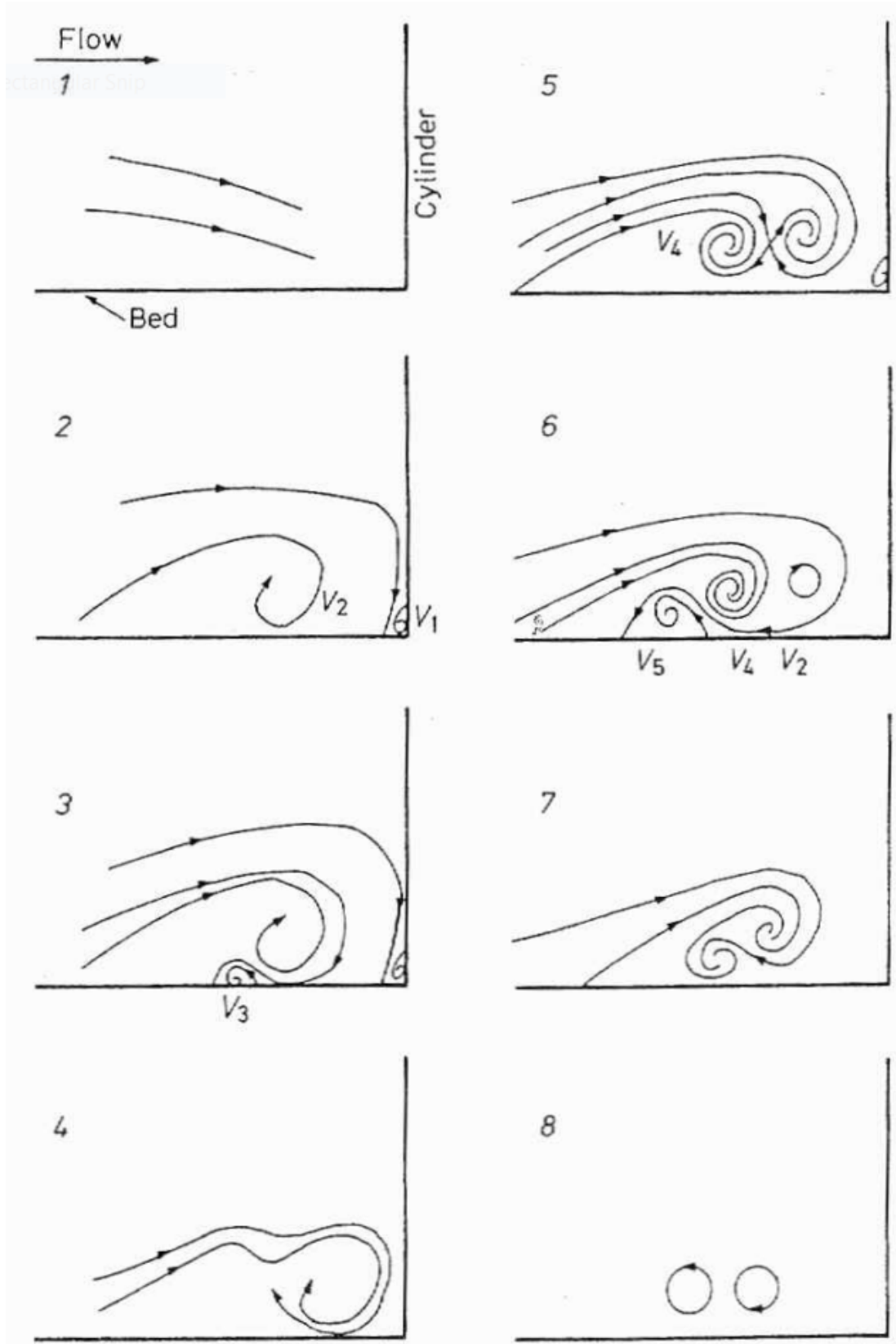


Figure 2.2: General pattern of the horseshoe vortex system. (Dargahi [1989])

2. LITERATURE REVIEW

tions of the main necklace vortex between two states, namely the back-flow mode and the zero-flow mode. Probability density functions of streamwise and spanwise velocities showed a double-peaked shape which confirmed the oscillations of the primary vortex between the two modes. They associated occurrence of high bed shear stress to the bimodal oscillations. Many more numerical studies later has confirmed the occurrence of bimodal oscillations of the HV system (Bressan et al. [2011]; Kirkil et al. [2008]; Koken [2011]; Koken and Constantinescu [2008a, 2009, 2011, 2014]; Koken and Gogus [2015]). Kwan and Melville [1994] carried out 3D experimental measurements on flow around wing-wall abutment using the hydrogen bubble technique and discovered the horseshoe vortex to be the primary vortex responsible for the scouring process. Chrisohoides and Sotiropoulos [2003] investigated the details of free surface flow past a vertical abutment at high Reynolds numbers using the Lagrangian Coherent Structure (LCS) where they introduced small tracer particles (paper pieces) to visualise the flow field. They found that the structure of the separated flow in the recirculation region upstream of the vertical abutment is very complex and quasiperiodic. Following Chrisohoides' experimental work is Paik and Sotiropoulos [2005], who carried out complementary DES and found that the corner vortex upstream of the abutment oscillates between a single and double eddy state in a random manner. Ultimately, these evidences provide insights to the important role played by the HV system in the development of the scour hole on the alluvial bed.

2.1.2 Flow contraction

However, the HV system is not the only factor responsible for scouring. The strongly accelerated flow at the tip of the abutment can induce high bed shear stress values and cause local scouring. The degree of flow acceleration is strongly linked to the flow contraction in the channel which directly affected by the length and the height of the hydraulic structure. For instance, Koken and Gogus [2015] used detached eddy simulation (DES) to investigate the effect of different length of vertical spur dikes on the flow dynamics and the bed shear stress. Results had shown that the length of the coherent structures observed downstream of the spur dikes increased dramatically with the increase of spur dike length. The total

2. LITERATURE REVIEW

area of large bed shear stress region in the longest spur dike is approximately 30 times larger than that in the shortest spur dike which translates to a much larger potential scour region in the long spur dike. [Koken \[2017\]](#) carried out DES on different flow contractions created by different lengths of spill-through abutment pairs connected at opposite sides of the channel. They found that the small contraction ratio coherent structures forming around the abutments are very similar to the ones observed for isolated abutments. On the other hand, in the large contraction ratio, the formation of two counter rotating contraction vortices at the centre of the channel close to the channel bed was found to have increased the bed shear stress beneath their mean path.

The flow contraction discussed in these previous papers are generally in the lateral direction which covers only non-extreme flooding scenarios. In the extreme cases, flood water overtops the abutments and essentially bridges and produces a more complex flow dynamics around the abutments which consists of lateral and vertical flow contraction. [Kara et al. \[2015a\]](#) performed a large eddy simulation (LES) to investigate the flow dynamics through a submerged bridge opening with overtopping. Due to the overtopping feature of the flow, a vortical structure along the spanwise axis forms after the bridge structure as seen in [Fig. 2.3a](#) while near the bed ([Fig. 2.3b](#)), the vortex remains at the vertical axis. The complex interactions between these vortices created high magnitudes of turbulent kinetic energy and bed shear stress which shown great implications relative to scour of a moveable sediment bed during extreme flood events.

2.1.3 Abutment form

The majority of the discussed literature above adopted a somewhat idealised in-stream hydraulic structure which consists of vertical walls and sharp corners (e.g. vertical spur dikes ([Fig.2.4a](#))). The sharp deceleration and downflow before the structure creates an adverse pressure gradient which in turn increasing the bed shear stress locally. In most practical applications, however, the abutment has sloped sidewalls to deflect more gradually the incoming flow while reducing the strength of the downflow and ultimately, the coherence of the HV system that drives the scour in front of and around the flank of the abutment ([Dey and](#)

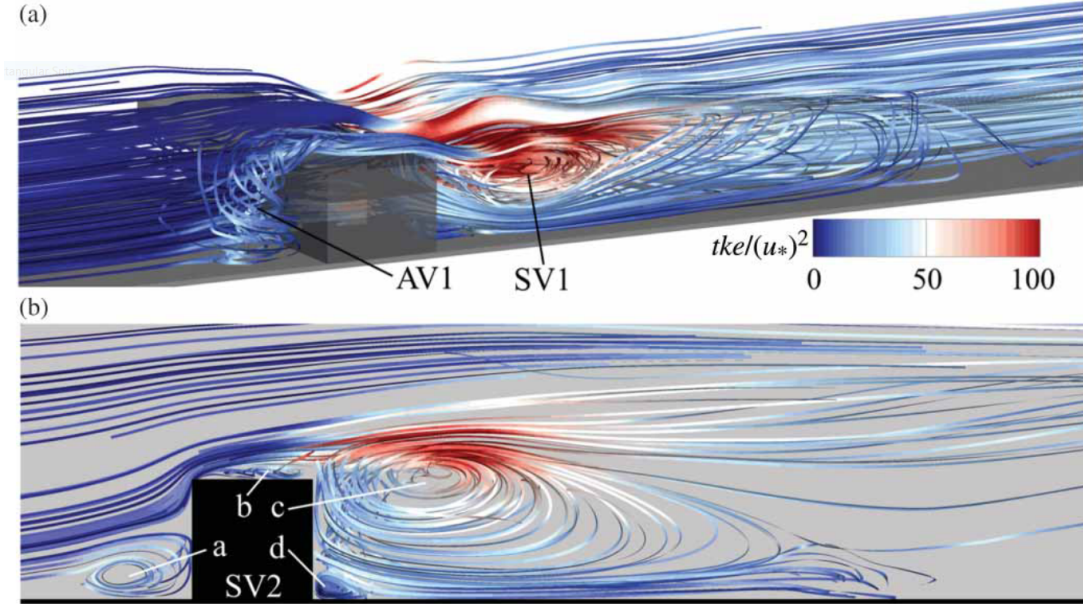


Figure 2.3: Streamlines of the time-averaged flow over a submerged bridge. (a) Oblique view from behind and (b) in a horizontal plane near the bed (Kara et al. [2015b])

Barbhuiya [2006]). This motivated several studies (Koken [2017]; Koken and Constantinescu [2014]; Morales and Ettema [2013]) to adopt abutments with sloped sidewalls (Fig. 2.4c) and they had found that the bimodal oscillations of HV system decay faster with the growth of scour hole when compared to vertical-wall abutments. With the flexibility of immersed boundary method in representing complex submerged structures, the present study conducts the simulations using spill-through abutments with rounded corners (Fig. 2.4d).

2.1.4 Compound channel

The common configuration of rivers consists of a main channel flanked by floodplains. This configuration is of great importance because in many cases the main channel of the rivers is not enough to discharge the total flow, mainly during flood events. There are numerous studies on compound open channel and most of their discussion focus on the interface between the main channel and floodplain. Cater and Williams [2008] and Kara et al. [2012] performed large eddy simulations in

2. LITERATURE REVIEW

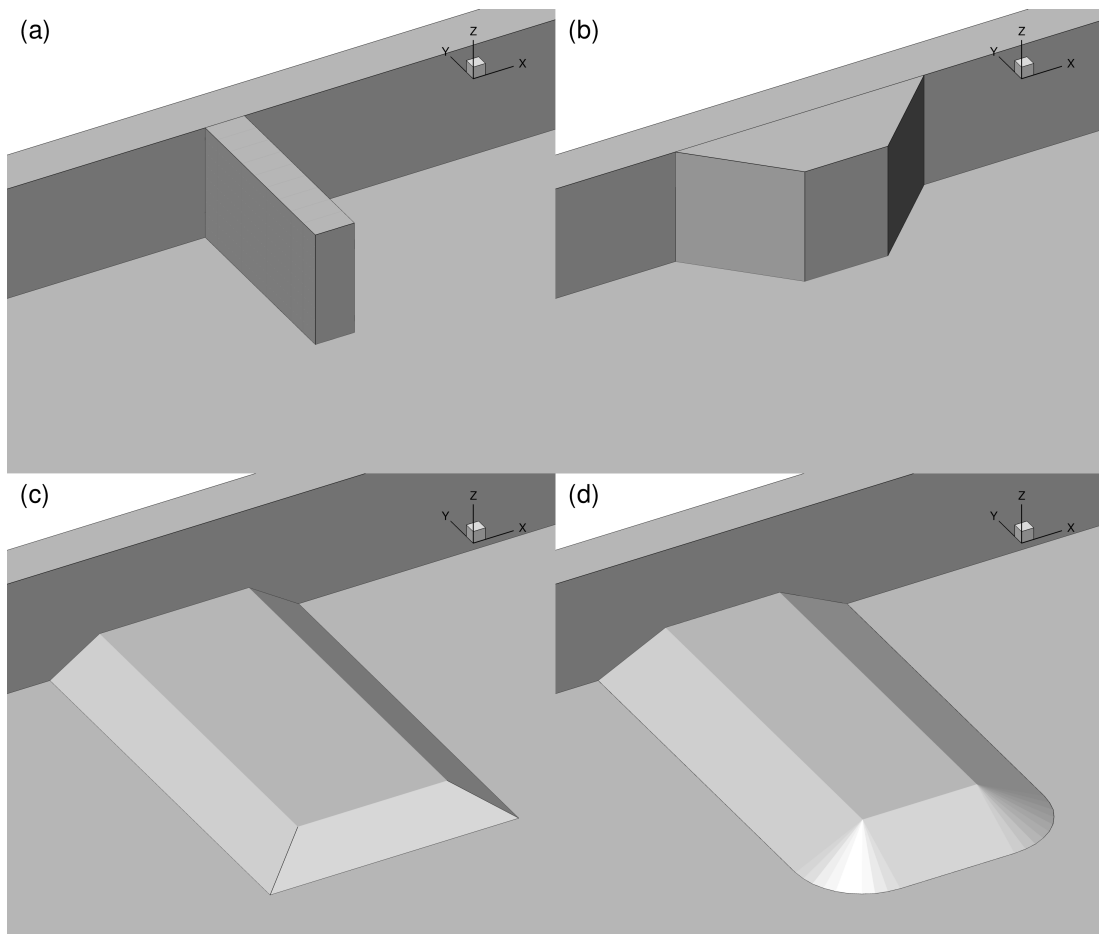


Figure 2.4: Types of side wall mounted hydraulic structures: (a) spur dike; (b) wing-wall abutment; (c) sloped side-wall abutment; and (d) spill-through abutment with rounded corners

a rectangular channel and a floodplain. Both studies reported that the strong lateral momentum transfer from the main channel to the floodplain is driven by the secondary current at the interface region. This resulted in the formation of a prominent bulge of velocity and bed shear stress at the main channel-floodplain interface. Biglari and Sturm [1998] attempted to predict the flow characteristics in a compound channel with and without bridge abutments on the floodplains by using a 2D depth-averaged $k - \epsilon$ turbulence model. The results showed promising prediction of the depth-averaged velocity and water surface elevation but little information on the flow interaction between the compound channel and abutments was reported. The present study tries to address this issue by simulating a 3D compound and asymmetric open channel with spill-through abutments on the floodplains.

2.2 Bridge Abutment Scour

2.2.1 Sediment transport theory

Scour is a process of sediment transport. When water flows over a sediment bed, a hydrodynamic force is exerted by the water on the individual sediment grains at the bed surface. For non-cohesive sediments such as sands and gravels, the weight forces of the particles themselves are the only forces that resist particle entrainment. The threshold of sediment movement occurs when applied forces due to fluid drag and lift exceed the stabilizing force due to gravity.

The Shields parameter is commonly used to identify the threshold of sediment movement based on mean flow properties and characteristics of the sediment. For flow below the threshold conditions, the riverbed is stable with no movement of sediment. For flows above the threshold conditions, the boundary sediment will be entrained in the flow with sediment movement taking place. Shields collected experimental data on initiation of motion and bedload transport of sediment and presented the Shields diagram using a dimensionless parameter τ_{*c} to express the initiation of sediment motion as a function of the boundary Reynolds number which is affected by viscosity and sediment size. Later, the Shields diagram

2. LITERATURE REVIEW

Table 2.1: Properties of sediment adopted in this study.

Sediment	d_{50}, mm	σ_g	d_*	τ_{*c}	$u_{*c}, m/s$
A	1.1	1.12	27.83	0.038	0.026

was modified by many other researchers, including [Yalin and Karahan \[1979\]](#), [Buffington \[1999\]](#) and [Sturm \[2001\]](#). The modified Shields diagram is shown in [Fig. 2.5](#) in terms of a dimensionless grain diameter, d_* which is defined by

$$d_* = \left(\frac{(SG - 1)gd_{50}^3}{\nu^2} \right)^{\frac{1}{3}} \quad (2.1)$$

in which SG = specific gravity of the sediment, g = gravitational acceleration, d_{50} = median sediment grain size, and ν = kinematic viscosity of the fluid.

The critical value of shear velocity for the initiation of motion of each sediment, u_{*c} , is given by

$$u_{*c} = \sqrt{\tau_{*c}(SG - 1)gd_{50}} \quad (2.2)$$

where u_{*c} is the critical value of shear velocity, τ_{*c} is the Shields parameter (determined directly from [Fig. 2.5](#)), which is equal to $\tau_c/[(\gamma_s - \gamma)d_{50}]$, τ_c is the critical shear stress for incipient sediment motion, γ_s is the specific weight of sediment, γ is the specific weight of fluid, d_{50} is median grain size, SG is the specific gravity, and g is gravitational acceleration.

In the present study, the properties of the sediment is adopted from the complementary experimental work from Georgia Institute of Technology, USA and are listed in [Table 2.1](#).

In a deformed bed after scour equilibrium is achieved, the critical shear stress for incipient motion, τ_c should be adjusted accordingly to take into account the gravitational bed slope effects at the scour region. [Jensen et al. \[2006\]](#) proposed

2. LITERATURE REVIEW

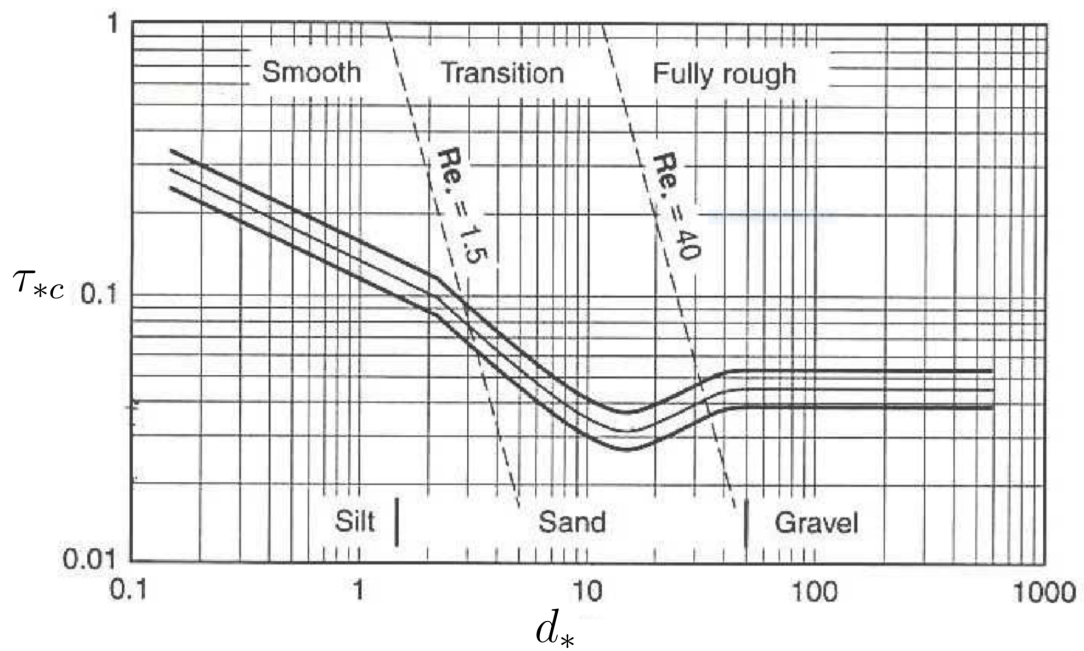


Figure 2.5: Shields diagram for direct determination of critical shear stress (Sturm [2001])

2. LITERATURE REVIEW

an adjustment formula which accounts for bed slope effects based on the angle of repose of sand (33° in present study) and the local maximum angle of the inclined surface with the horizontal. The adjustment formula is represented by

$$\tau_{*c} = \tau_{*c,0} \frac{\sin(\alpha + \theta)}{\sin(\theta)} \quad (2.3)$$

where $\tau_{*c,0}$ is the critical bed shear stress for incipient motion on a flat bed, θ is the angle of repose for the sediment, and α is the maximum angle of the inclined surface with the horizontal.

2.2.2 Types of scour at bridge abutment

Scour at bridge crossings can be generally divided into three different types; general scour, contraction scour, and local scour. Contraction scour and local scour are both induced by the existence of in-stream structure (bridge abutment, spur dike, or piers), and can occur either as clear-water scour or live-bed scour.

General scour: Fluvial, geomorphological and hydrometeorological processes in a river result in long-term variations in the flow conditions which cause changes in geomorphic form of the river including both downcutting and deposition. These river form adjustment processes are often referred to as long-term aggradation or degradation, but gradual translation of meanders and even changes between geomorphic river types such as meandering and braided can occur. General scour occurs irrespective of the presence of a bridge structure. Lateral shifting of the channel banks due to meandering can result in bridges being outflanked by the river.

Contraction scour: The flow at a bridge usually converges as it approaches the bridge. The encroachment from the abutments causes the flow to contract, separate from the abutments and accelerate through the bridge section. Downstream of the bridge the flow decelerates, gradually redistributing itself throughout the river channel. The accelerated flow in the bridge section exerts a greater shear stress on the bed sediment, which results in a contraction scour throughout the contracted area.

2. LITERATURE REVIEW

Local scour: Local scour is caused by the direct interference of the bridge abutment or pier with the flow, setting up three-dimensional flow structures and vortex systems responsible for inducing local scouring process. Local scour only occurs if the local flow field has enough energy to transport the bed sediment and it is characterized by the formation of scour holes adjacent to the abutment or pier. Interrelated local scour processes include separation of the approach flow from the bed, downflow in front of the obstruction, formation of a horseshoe vortex that wraps around the base of a pier or abutment, a separated shear layer adjacent to the pier or abutment, and a wake region immediately downstream of the obstruction. (Lee and Sturm [2009])

Contraction scour is generally limited to the length of the contraction and perhaps a short distance up and downstream, whereas general scour tends to occur over longer reaches (Fischenich and Landers [2000]). Melville and Coleman [2000] stated that depth of local scour are much larger than that by general scour, often by a factor ten.

The characteristics of local scour and contraction scour can vary depending on the condition of the approaching flow and they are classified by Chabert and Engeldinger [1956] into two categories, namely, clear-water scour and live-bed scour.

Clear-water scour: Clear-water scour occurs when the sediment in the approach flow just upstream of the scour area is at rest. This happens when the shear stress exerted on the sediment by the flow is less than the critical shear stress of the sediment. Under clear-water conditions, no sediment is transported into the scour hole from upstream, and the maximum scour depth occurs when the flow can no longer remove sediment from the scour hole; that is, when the shear stress falls below its critical value.

Live-bed scour: Live-bed scour occurs when the sediment upstream of the scour area is being transported, such that there is sediment transport by the river. This happens when the shear stress exerted on the sediment by the flow is greater than the critical shear stress of the sediment. Under live-bed conditions, the local scour hole develops rapidly and then oscillates about the equilibrium scour depth due to the propagating bed-forms (see Fig. 2.6). The magnitudes of the bed-forms influence the maximum scour because the troughs of the bed-

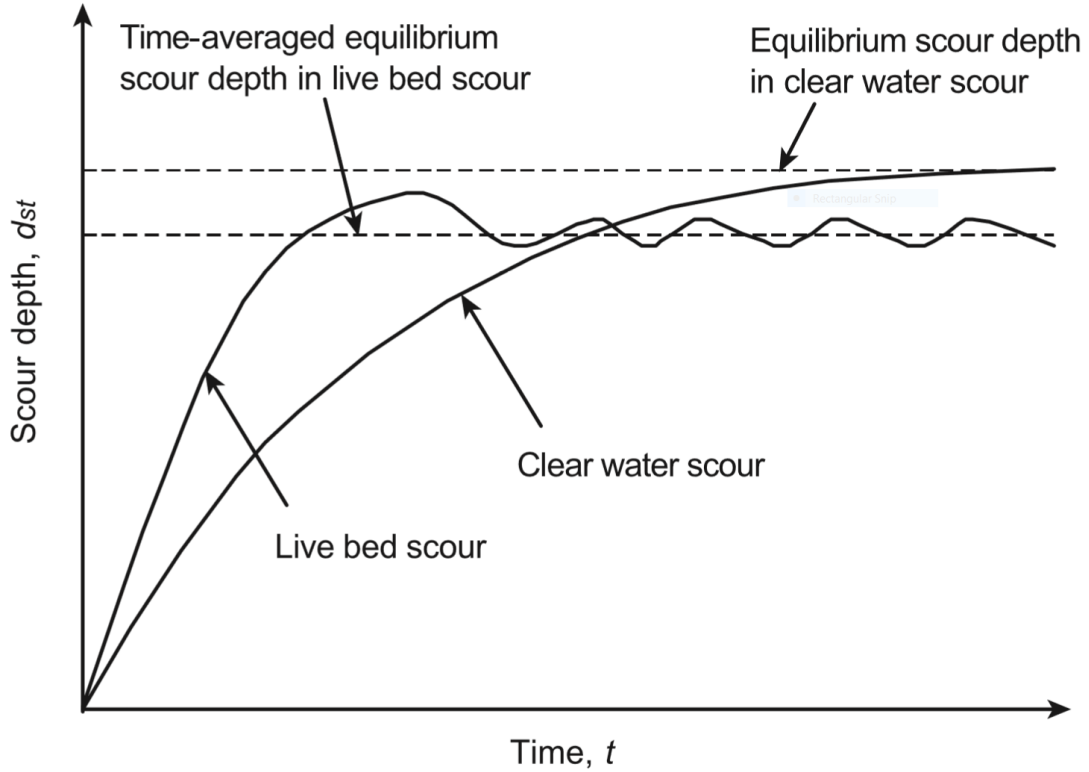


Figure 2.6: Time development of clear-water and live-bed scour (Chabert and Engeldinger [1956])

forms momentarily and locally lower the bed as they propagate through the bridge cross-section. The equilibrium scour depth is attained when the rate at which sediment is transported into the scour hole is equal to the rate at which it is removed from the scour hole.

The time-variation of clear-water and live-bed scours are shown schematically in Fig. 2.6 to compare the characteristics between them. It was observed that the clear-water scour condition takes much longer time to achieve the stable peak when compared to live-bed scour. Generally, the maximum clear-water scour depth is approximately 10% greater than the live-bed scour depth. In the present study, only the clear-water scour is considered in all simulations.

2.2.3 Experimental approach on scour prediction

For more than half a century, the experimental approach has been the most common and arguably the most effective method in predicting scour around an abutment. There are mainly two types of experimental studies; the first type focuses in explication of the three-dimensional flow field around a bridge abutment as mentioned in the previous section; and the second type, which is the more familiar approach, focuses in developing empirical correlations between number of identified parameters and essentially presenting them in the form of scour prediction formulas. The more common abutment scour depth equations can be found in the publications of Laursen [1963]; Melville and Coleman [2000]; Sturm [2001, 2006]; Sturm and Janjua [1994]; Sturm et al. [2011].

The major difficulty in obtaining an accurate scour prediction method is the large number of variables affecting the scour. The parameters involved in the scour phenomenon at abutments can be grouped as follows:

1. Parameters relating to the geometry of channel:
 - width
 - cross-sectional shape
 - slope.
2. Parameters relating to the abutment:
 - size
 - shape
 - orientation with respect to main flow and surface condition
3. Parameters relating to the bed sediment:
 - median size, d_{50}
 - grain size distribution, σ_g
 - mass density, ρ_s
 - angle of repose, θ

2. LITERATURE REVIEW

- cohesiveness
4. Parameters relating to the fluid:
 - density, ρ
 - viscosity, ν
 - gravitational acceleration, g
 - temperature
 5. Parameters relating to the approaching flow condition:
 - mean flow velocity, V_1
 - flow depth, y_1
 - shear velocity, $u_{*,0}$
 6. Parameters relating to time:
 - time, t

[Sturm et al. \[2011\]](#) carried out dimensional analysis to elucidate and identify the effect of each parameters on the problem of local scour around an abutment in a compound channel with reference to the definition sketch in Fig. 2.7 and the result is given as

$$\frac{y_{fmax}}{y_{f1}} = f\left(\frac{d_{50}}{y_{f1}} \text{ or } \frac{V_1}{V_{c1}}, \frac{\rho V_1 L_a}{\mu}, \frac{L_a}{d_{50}}, \frac{L_a}{y_f}, \frac{W_e}{y_f}, K_s, K_\theta, \frac{H_b}{y_{f1}}, \frac{y_{m1}}{y_{f1}}, \frac{L_a}{B_f}, \frac{B_m}{B_f}, \frac{V_1}{\sqrt{g y_1}}, \frac{k_f}{k_m}, \frac{\sigma}{\gamma_E H_E}, \frac{V_{f1} t}{y_{f1}}\right) \quad (2.4)$$

where y_{fmax} is the maximum depth of flow after scour, y_{f1} is the flow depth in the bridge approach section upstream of the abutment/embankment, V_1 is the approach flow velocity, V_{c1} is the critical approach velocity, ρ and μ are the density and viscosity of fluid, respectively, L_a is the abutment length, d_{50} is the median sediment grain size, y_{f1} and y_{m1} are the approach floodplain and main channel flow depth, respectively, W_e is the width of the embankment in

2. LITERATURE REVIEW

the flow direction, K_s is an abutment shape factor, K_θ is a factor accounting for the abutment alignment to the flow, y_{m1} is the main-channel flow depth in the bridge approach section, H_b is distance from initial bed to the bridge low chord in the floodplain, B_m is the main-channel width, B_f is the floodplain width, g is gravitational acceleration, k_f and k_m are roughness height of the floodplain and main channel beds, respectively, σ is bulk shear strength of the embankment fill, γ_E is the bulk density of the embankment material, H_E represents the height of the embankment and t is time.

Sturm et al. [2011] suggested that the Melville formula (Melville and Coleman [2000]) is the most applicable formula for short, solid-wall abutments (as presented in this study). From the extensive experimental work at the University of Auckland, Melville and Coleman [2000] proposed the formula for maximum abutment scour depth to be as follows:

$$d_s = K_{yL} K_I K_d K_s^* K_\theta^* K_G \quad (2.5)$$

in which d_s is the maximum scour depth, K_{yL} is the abutment length factor, K_I is the approach flow intensity factor, K_d is the sediment size factor, K_s^* is the abutment shape factor, K_θ^* is the abutment alignment factor and K_G is the channel geometry factor. All the K factors are empirical expressions as follows:

$$K_{yL} = \left\{ \begin{array}{ll} 2L; & \frac{L}{y} \leq 1 \quad (\text{Short abutment}) \\ 2(yL)^{0.5}; & 1 \leq \frac{L}{y} \leq 25 \quad (\text{Intermediate abutment}) \\ 10y; & \frac{L}{y} \geq 25 \quad (\text{Long abutment}) \end{array} \right\} \quad (2.6)$$

L is the length of abutment and y is the depth flow. These expressions indicate that scour depth is independent of depth of flow for short abutments and independent of abutment length for long abutments.

2. LITERATURE REVIEW

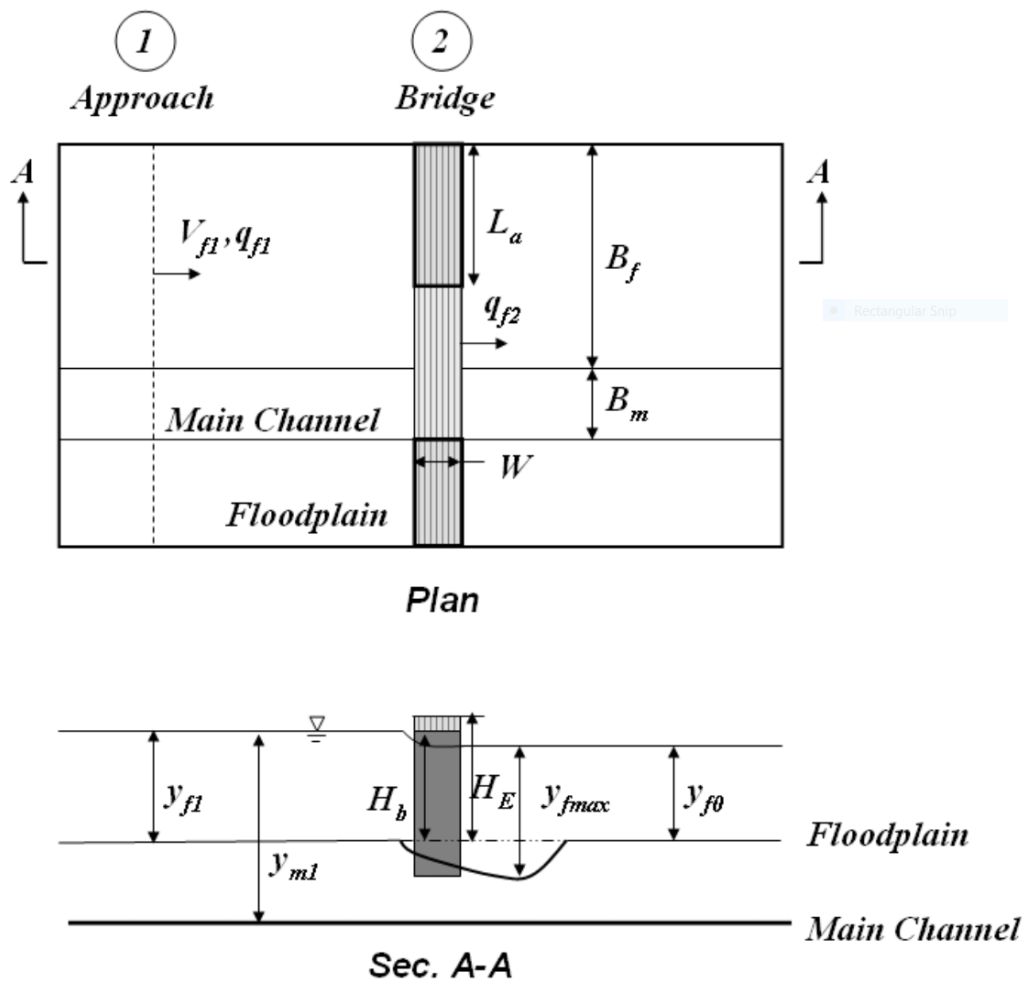


Figure 2.7: Definition sketch for abutment scour in a compound channel. (Sturm et al. [2011])

2. LITERATURE REVIEW

Table 2.2: Abutment shape factors, K_s for Melville scour formula.

Abutment shape	K_s
Vertical-wall	Square End
	0.75
	Semi-circular End
	0.75
45° Wing-wall	0.75
Spill-through	0.5:1.0 (H:V)
	0.60
	1.0:1.0 (H:V)
	0.50
	1.5:1.0 (H:V)
	0.45

$$K_I = \begin{cases} \frac{V - (V_a - V_c)}{V_c}; & \frac{V}{V_c} < 1 \\ 1.0; & \frac{V}{V_c} \geq 1 \end{cases} \quad (2.7)$$

where V_a is the mean flow velocity at the "armour peak" ($V_a = V_c$ for uniform sediments, V_c is the critical shear velocity). The sediment size effect, K_d , appears only in relatively coarse size sediment ($L/d_{50} \leq 25$).

$$K_s^* = \begin{cases} K_s; & \frac{L_a}{Y} < 10 \\ K_s + 0.67(1 - K_s)(0.1 \frac{L_a}{Y} - 1); & 10 \leq \frac{L_a}{Y} \leq 25 \\ 1.0; & \frac{L_a}{Y} \geq 25 \end{cases} \quad (2.8)$$

in which K_s is given in the Table 2.2. The abutment alignment factor, K_θ is varied from 0.9 to 1.1 depending on the angle between the abutment and flow direction.

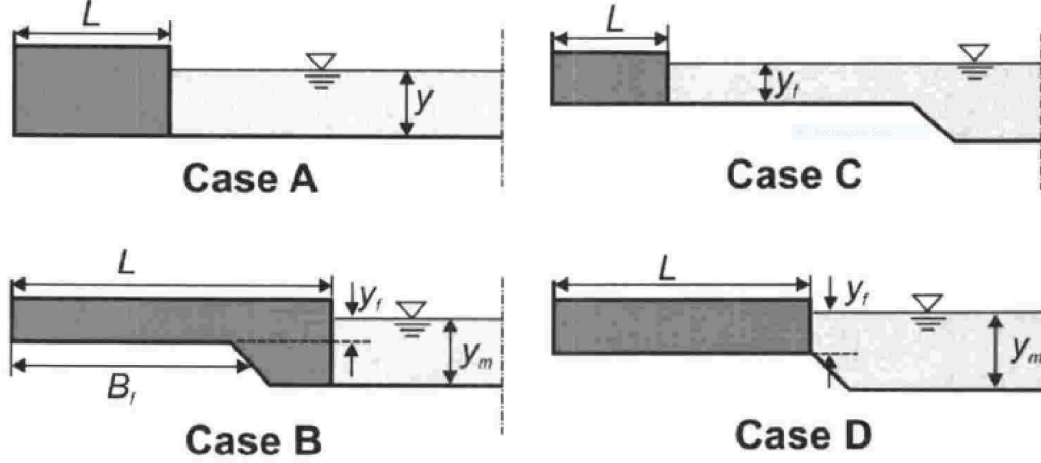


Figure 2.8: Typical cases of abutment positions in compound channels. (Melville and Coleman [2000])

$$K_G = \left. \begin{array}{l} 1.0; \quad \text{Case A} \\ \sqrt{1 - \frac{B_f}{L} \left[1 - \left(\frac{y_f}{y_m} \right)^{\frac{5}{3}} \frac{n_m}{n_f} \right]}; \quad \text{Case B} \\ 1.0; \quad \text{Case C} \\ \left(\frac{y_f}{y_m} \right)^{\frac{5}{6}} \left(\frac{n_m}{n_f} \right)^{\frac{1}{2}}; \quad \text{Case D} \end{array} \right\} \quad (2.9)$$

where y_m and y_f are the flow depths in the main channel and on the floodplain, respectively and n_m and n_f are the Manning's roughness values in the main channel and on the floodplain, respectively. Case A to D are shown in Fig. 2.8 and they represent different abutment positions in compound channels.

2.2.4 Numerical approach on scour prediction

With the advancement of super-computing power, the numerical approach in the scour related field has gained its popularity. The numerical studies are mainly divided into two categories: (1) to study the complex three-dimensional flow field around an abutment with deformed bed (usually at equilibrium scour condition);

2. LITERATURE REVIEW

and (2) to predict the scour pattern and maximum depth around an in-stream structure.

The flow field around an abutment in a scour hole is closely related to those numerical studies discussed in Sec. 2.1. Researchers focus on the flow features found in scour holes by identifying the coherent structures in the form of vortices and near bed quantities like bed shear stress and turbulent kinetic energy. [Koken and Constantinescu \[2008b\]](#) performed LES on a deformed bed around a spur dike ($Re = 1.8 * 10^4$) and reported that the aperiodic oscillations of the HV system, which dominates the flow field on a flat bed, are still present even after the scour equilibrium state is achieved. The intensity of the HV system, however, had substantially decayed when compared with that in the pre-scour state reported in part 1 of the study ([Koken and Constantinescu \[2008a\]](#)). A similar finding is reported in [Koken and Constantinescu \[2011\]](#) where they carried out DES on a low Reynolds number flow ($1.8 * 10^4$) and a much higher Reynolds number flow ($2.4 * 10^5$). Interestingly, they found that the presence of a second main necklace vortex inside the scour hole is a unique feature for the high Re case that was not observed in the low Re case. As for the near bed quantities in a deformed bed, both studies showed that the $> 97\%$ of the scour hole region has lower bed shear stress than the critical value. In the remaining region where bed shear stress is over the critical value, analysis of mean flow fields suggested that a sort of equilibrium is reached between the sediment entrained from these regions and the sediment deposited back into these regions, such that in average the bathymetry does not change.

To simulate the process of sediment transport, there are mainly two types of approaches; the first type is the coupling of a morphological model, which includes a sediment transport formulation, with a hydrodynamic model, which is responsible for the flow solution; and the second type is called the Euler-lagrange coupling method where individual sediment motion in the fluid is being simulated taking into consideration the effects of drag, lift, and added mass of sediment.

Most existing morphological modeling is based on the classic sediment transport formula proposed by [Meyer-Peter and Müller \[1948\]](#). [Khosronejad et al. \[2012\]](#) carried out URANS with a bed morphological model on bridge piers with different shapes (round, square and diamond) and orientations. The results of the

2. LITERATURE REVIEW

topography and temporal evolution of the scour did not look promising especially for the round and square piers. They highlighted the importance of correctly resolving the HV system around the piers and concluded that URANS model are not adequate. [Dixen et al. \[2013\]](#) performed simulations on a half-buried sphere with a $k - \omega$ SST turbulence model. The novelty of the study was to include the effect of externally-generated turbulence (induced by the HV system and lee-wake flow) in the sediment transport description. The result of temporal scour evolution showed very good agreement with the experimental results when the effect of the externally-generated turbulence was turned on as opposed to a discrepancy of 35% when it was off. However, the improvement was found to work only in live-bed cases and have practically no effect on clear-scour condition. Ultimately, the overall accuracy of the morphological model is insufficient as the sediment transport formulas were obtained based on steady unidirectional flows and equilibrium sediment transport conditions, their applicability to sediment transport around local hydraulic structures is questionable.

Euler-lagrange coupling approach is emerging as a promising method to simulate the grain motion in fluids. With this method, the sediment particles are treated as an independent phase in a Lagrangian frame and are simultaneously coupled with the fluid phase in an Eulerian frame. As the detailed movement of individual particles are exactly tracked, this kind of two-phase flow models are capable of resolving more physics and are expected to be more general and accurate ([Fukuoka \[2013\]](#)). [Escauriaza and Sotiropoulos \[2011\]](#) proposed an Euler-Lagrange model to investigate the mechanisms of bedload transport in turbulent junction flows. They coupled a 3D DES model for the fluid and a Lagrangian particle model based on the particle momentum equations. The model was able to reproduce reasonably the sediment dynamics observed in multiple experiments performed under similar conditions. Their findings provided fundamental information on the initiation of motion and the multifractal nature of bed-load transport processes. [Zhang et al. \[2015\]](#) presented a 3D EulerLagrange two-phase flow model for local scour around a spur dike, coupling the $k - \epsilon$ URANS turbulence model with a lagrangian model. The cost-effectiveness nature of URANS enabled them to simulate the whole scouring process until the equilibrium state. The agreements between the model and experimental results were reasonable. The

euler-lagrange method sheds a light on the formulation of more universal models for sediment transport. However, the approach still needs refinement to account for inter-particle collisions and extension to more densely sediment-laden flows.

2.3 Free Surface Flow

The water surface is present in a wide range of flows that are of interest within engineering hydrodynamics, from the ubiquitous open channel flow to low submergence coastal flows past marine structures such as tidal stream turbines. Such surfaces, often termed free-surfaces, represent the boundary between the water body and the air above it, and may deform in response to the local flow physics including turbulence and bathymetric features. Deformation due to turbulence is generally small when compared to spatial and temporal variations of the mean surface position due to bed non-uniformity, ocean waves and the presence of hydraulic structures.

The equations governing free-surface flow are significantly more complex than those governing internal flow as they are subject to additional kinematic and dynamic boundary conditions at the (free) surface (Ferziger and Peric [2002]; Hodges and Street [1999]). The kinematic condition is hyperbolic in nature and states that, since there can be no convective mass transfer across the air-water interface, the component of fluid velocity in the direction normal to the surface must be equal to the velocity of the surface itself. The dynamic boundary condition stipulates a force equilibrium at the interface, implying that the pressure and viscous forces exerted by the air and water respectively must be balanced. The boundary conditions introduce new nonlinear terms into the Navier Stokes equations, complicating their numerical solution significantly, although in hydraulics the dynamic condition is generally ignored since it is assumed that the surface tension can be neglected and the pressure on the air side can be assumed to be constant.

There are various ways to handle the free-surface boundary in CFD. The easiest approach is to ignore the free surface deformations and do the rigid lid approximation as will be described in Section 2.3.1. The more complicated matters

2. LITERATURE REVIEW

are the numerical approaches that compute free-surface deformations as the numerical solution progresses (for instance at every time step) and these are largely grouped into two distinct categories: interface tracking methods and interface capturing methods (described in Sections 2.3.2 and 2.3.3, respectively).

2.3.1 Rigid lid approximation

Within the field of hydraulics, the vast majority of simulations of flows involving water surfaces to date have employed the so-called rigid lid approximation, in which a fixed (generally flat) surface or lid is used to represent the water surface. A free-slip boundary condition is stipulated at the lid, and the simulation is in fact that of a closed conduit with an artificial, frictionless condition at the lid. By definition the shear stress at the lid is zero, as is the component of the fluid velocity in the direction normal to it, but the pressure is free to vary as it would along a wall, which in turn produces zero shear stress there. This in effect constitutes a symmetry boundary condition. Rather than calculating the surface height with knowledge of the local fluid pressure, the problem is now reformulated and it is necessary to calculate the pressure based on the known height of the surface. The surface-elevation-gradient terms in the momentum equations for free-surface flows are thereby replaced by pressure gradients so that the dynamic effects of surface-elevation variations are properly accounted for by the rigid lid approximation method. The suppression of the actual surface deformation introduces an error in the continuity equation, but this is small when the surface deviation is small compared with the local water depth, say below 10% of the depth. Since local surface perturbations due to turbulence satisfy this condition in a large range of engineering flows the rigid lid approach has been applied with considerable success in a number of studies. This is particularly true of open-channel flows, where rigid lid LES and direct numerical simulations (DNS) have led to important insights on the structure of bed-generated turbulence (Bomminayuni and Stoesser [2011]; Lam and Banerjee [1992]; Pan and Banerjee [1995]; Singh et al. [2007]; Stoesser and Nikora [2008]).

To assess the validity of the rigid lid assumption Komori et al. [1993] included the surface variations in their computation by including the kinematic boundary

2. LITERATURE REVIEW

condition and compared the results with those from the rigid lid simulations of [Lam and Banerjee \[1992\]](#). They found that the free-surface deformations and near-surface normal velocities remained extremely small, leading them to conclude that the calculated flow behaviour near the free-surface did not differ from the rigid lid simulations. However, it is expected that the errors will be more significant when the surface fluctuations are not small compared with the local water depth. In fact, it is generally accepted that the rigid lid approximation is only strictly applicable to low Froude number (i.e. $Fr \leq 0.5$) flows ([Koken and Constantinescu \[2009\]](#); [Paik and Sotiropoulos \[2005\]](#)). [Kara et al. \[2015a\]](#) performed two LES for flow through the same bridge contraction geometry, one with a rigid lid boundary and one with a free-surface capturing algorithm. The bulk Reynolds number was 27 200 and although the bulk Froude number was relatively low at $Fr = 0.37$, locally values of $Fr = 0.78$ were reached as a result of the significant constriction imposed on the flow by the abutment (the ratio of channel width to abutment width was 3). [Kara et al.](#)'s results showed that although the first order statistics and bed shear stresses were very similar for the two simulations, the instantaneous turbulence structure and second order statistics showed significant disparity. [Fig. 2.9](#) shows the distribution of normalised turbulent kinetic energy (tke) in a horizontal plane near the bed at $z/H = 0.1$ as computed in both simulations by [Kara et al. \[2015a\]](#). The peak of the high tke occur closer to the tip of the abutment for the free-surface simulation; in contrast to the rigid lid simulation where the peak is observed further downstream. This difference is quite significant with regards to local scour because near-bed tke is an important ingredient of the erosion mechanism. Their study highlighted the limitation of the rigid lid approximation and the requirement for more sophisticated approaches for the simulation of turbulent flows with complex water-surface deformations.

2.3.2 Interface tracking methods

In interface tracking methods, also known as moving mesh methods, the mesh deforms after every time step to ensure that the boundary of the computational domain matches the free-surface position, thereby ensuring that the surface is

2. LITERATURE REVIEW

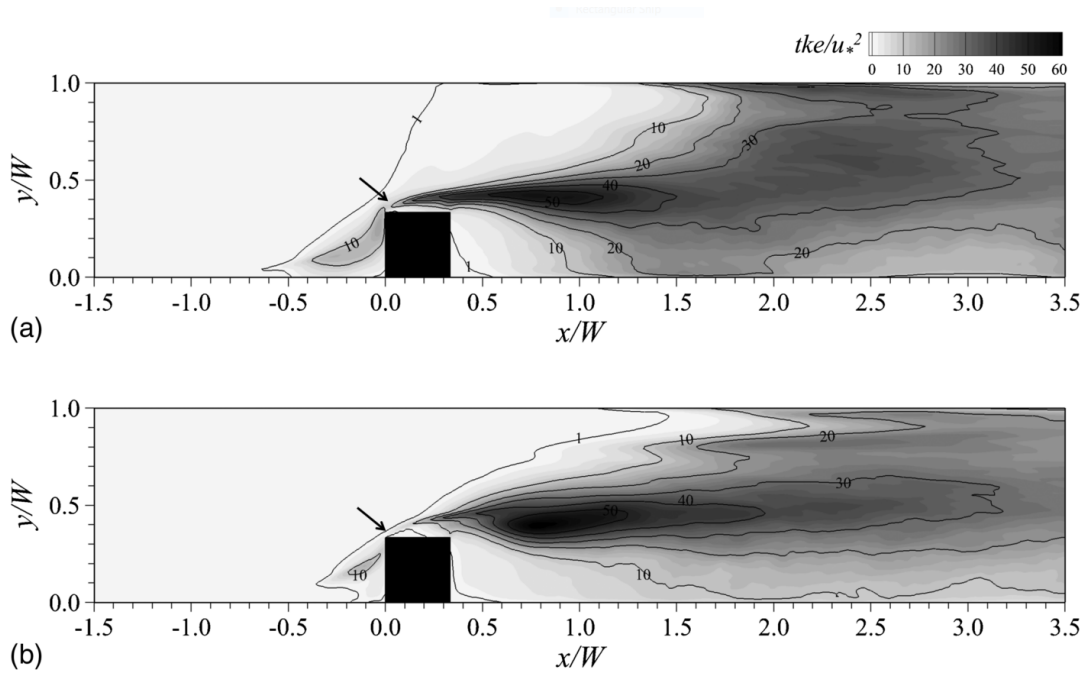


Figure 2.9: Distribution of normalised turbulent kinetic energy in a horizontal plane near the bed at $z/H = 0.1$ as computed by (a) free-surface-resolved simulation; (b) rigid-lid simulation (Kara et al. [2015a])

2. LITERATURE REVIEW

explicitly tracked.

The principal advantages of interface tracking methods arise from the inherent reduction in the number of grid nodes since no nodes are required in the air phase, and the lack of numerical diffusion which tends to smooth out the interface in other methods (Chang et al. [1996]). Although the boundary integral technique is perhaps the interface tracking method that has attracted the most attention (Hou et al. [1994]), due to its unsuitability to flows that are governed by the viscous Navier Stokes equations it is largely inapplicable to the field of hydraulics (Hou et al. [2001]). Much of the progress in interface tracking methods has been made in the field of ship hull hydrodynamics, where the key problem of interest is the interaction between the viscous boundary layer at the surface-piercing hull and the resulting surface wave (Longo et al. [1993]; Toda et al. [1992]). Most studies have focused on achieving accurate predictions of this interaction using RANS approaches: in this context Nichols and Hirt [1973], Farmer et al. [1993] and Raven [1996] employed free-surface height methods in which the free-surface was described as a height function, the solution of which was only loosely coupled temporally to the solution of the bulk pressure and velocities. Alessandrini and Delhommeau [1997] on the other hand employed a similar method but solved the height function and bulk flow simultaneously. Van Brummelen et al. [2001] and Raven and van Brummelen [1999] successfully applied an efficient iterative approach for steady and smooth surface waves, but noted that the performance of the method deteriorates and finally breaks down when steeper waves are simulated.

Miyata et al. [1987] employed an interface tracking method using finite differences, with a sub-grid scale model for turbulent stresses, in simulations of flow past a ship hull in which the surface wave profile had reached a steady state, with Reynolds numbers ranging up to 10^5 . Miyata et al. [1992] improved the accuracy of the method by employing a similar approach with finite volumes, successfully simulating Reynolds numbers up to 10^6 . In hydraulics, an interface tracking method in the context of LES has been presented by Hodges and Street [1999] who simulated the interaction of waves with a turbulent channel flow. These authors used an explicit time-discretization scheme to advance the free-surface by solving the kinematic boundary condition and solved a Poisson-type equation

2. LITERATURE REVIEW

after every time step to compute a new boundary-orthogonal grid. The Reynolds number in this case was relatively low $Re_\tau = 171$ so that the turbulent eddies and the surface deformations caused by them have rather large length and time scales. At Reynolds numbers of practical interest with much smaller turbulent length and time scales, the recalculation of a new mesh would be extremely expensive. In fact, Hodges and Street state that in such cases their method is not suitable. In an attempt to avoid the creation of a new mesh after every time step, Fulgosi et al. [2003] used a mapping scheme that transfers the curvilinear physical space into an orthogonal coordinate system, employing the technique in a DNS of wind-sheared free-surface deformations.

A significant drawback of interface tracking methods concerns their ability to deal with complex surface topologies, especially in three dimensions and when singularities are observed. In general the methods fail beyond the time of the singularity and additional operations are required to remove individual nodes close to such features, thereby adding to the overall computational cost (Chang et al. [1996]).

2.3.3 Interface capturing methods

In interface capturing methods, the water surface is not defined explicitly by the boundary of the numerical mesh as it is in interface tracking methods. Both fluid phases (i.e., water and air) are included on an Eulerian mesh, and an algorithm is therefore required to compute the evolution of the interface between them. In general, interface capturing methods have the advantage of avoiding the grid surgery problem that is encountered in interface tracking methods, but common difficulties are how to maintain the thickness of the interface and conserve mass across it.

Harlow and Welch [1965] first proposed the marker-and-cell (MAC) method, in which massless particles are seeded in the water phase and are passively advected with the flow. An important advantage of the approach compared to most interface tracking methods arises from its ability to handle complex surface topologies such as breaking waves. The MAC method does however require a large number of seeded particles, making it relatively computationally expensive.

2. LITERATURE REVIEW

As a result it has primarily been employed for 2-D or axis-symmetric flows [Armenio \[1997\]](#); [Veldman and Vogels \[1984\]](#); [Viecelli \[1971\]](#), although more recently [Tomé et al. \[2001\]](#) and [Sousa et al. \[2004\]](#) have extended it to three-dimensional tank filling and droplet splashing test cases. A comprehensive review of progress in MAC techniques can be found in [McKee et al. \[2008\]](#).

Rather than representing the free-surface using markers or particles, another class of interface capturing methods use scalar functions that do not need to coincide with grid lines and do not incur the vast computational expense of marker methods. The volume of fluid (VOF) method introduced by [Hirt and Nichols \[1981\]](#) is one such approach. In this method, the fraction of the liquid phase is determined by the solution of a transport equation for the void fraction F . By definition, F is the unity in any cell that is fully submerged in the liquid, zero in any cell fully exposed in the gas, and some fraction in the range $0 < F < 1$ in cells that contain the surface.

A number of research groups have proposed variants on Hirt and Nichols original method, generally with the intention of improving the robustness of the advection of the volume fraction and/or the accuracy of the geometrical representation of the surface; lower order schemes like first order upwinding tend to smear the interface due to numerical diffusion while high order methods suffer from stability issues and may result in numerical oscillations ([Gopala and van Wachem \[2008\]](#)). Existing variants include Hirt and Nichols original donor-acceptor scheme ([Hirt and Nichols \[1981\]](#)), the piecewise linear interface calculation method (PLIC) ([Youngs \[1982\]](#)), the simple line interface calculation method (SLIC) ([Noh and Woodward \[1976\]](#)), the flux-corrected transport method (FCT) ([Boris and Book \[1973\]](#)), the compressive interface capturing scheme for arbitrary meshes (CICSAM) ([Ubbink \[1997\]](#)), and the inter-gamma compressive scheme ([Jasak and Weller \[1995\]](#)). The SLIC and PLIC methods, which both use geometric as opposed to algebraic interface reconstruction, have proved relatively popular since their introduction, in large part due to their relative simplicity and ability to deal with breaking and merging interfaces. [Gopala and van Wachem \[2008\]](#), however, state that SLIC suffers from high levels of numerical diffusion and limited accuracy, while PLIC is difficult to implement in three dimensions and to boundary-fitted grids. CICSAM and the inter-gamma method, on the other hand, are

2. LITERATURE REVIEW

observed to conserve mass very well while also keeping the interface sharp, but they suffer from a high degree of sensitivity to the local Courant-Friedrichs-Lewy (CFL) number.

Despite the drawbacks of the VOF method, it has nonetheless grown in popularity since its introduction. [Thomas et al. \[1995\]](#) proposed a novel method that combined the height function approach (Section 2.3.2) with VOF, achieving mass and momentum conservation with very little numerical dissipation. Although the method was capable of simulating arbitrarily large surface deformations the slope of the surface was subject to a limit related to the cell aspect ratio, and breaking wave simulations were therefore not permitted. The method was applied to turbulent flow in a straight open channel by [Shi et al. \[2000\]](#) in a relatively poorly resolved LES that was designed to be run on a desktop workstation to demonstrate the applicability of the method within an engineering context. The turbulence metrics were found to be in agreement with experimental and DNS data.

[Sanjou and Nezu \[2010\]](#) reported LES of turbulent free-surface flows past emergent vegetation in compound open channels. Although no details of the VOF scheme were given, the results demonstrated the applicability of surface capturing approaches to LES of complex flows in hydraulics.

[Xie et al. \[2014\]](#) performed LES of turbulent open-channel flow over two-dimensional dunes. The simulations were designed to replicate the experiments of [Polatel \[2006\]](#), and two LES were carried out, one with the rigid lid approximation and one in which the free-surface was modelled using CICSAM VOF. The bulk Reynolds number, based on mean depth and bulk flow velocity, was 28,000. The relative submergence, that is to say the ratio of flow depth to dune height, was 4 and the Froude number was relatively low at 0.32. The mean velocity profiles from both LES agreed well with the experimental data, but some discrepancies were observed in the turbulence statistics. Furthermore, the VOF simulation revealed the presence of some degree of surface renewal in the form of upwelling and drafts.

The ability of the VOF method to cope with complex surface topologies that involve breaking up and merging has naturally led to its application to the study of breaking waves. While a number of early studies addressed this problem us-

2. LITERATURE REVIEW

ing RANS approaches (Bakhtyar et al. [2009]; Bradford [2000]), relatively few LES have been performed, and most of those are restricted to two dimensions (Lubin et al. [2011]; Watanabe and Saeki [1999, 2002]). Christensen [2006], however, extended into three dimensions but the simulations suffered from poor grid resolution.

The level-set method (LSM), which originated in computer graphics, has recently become a popular interface-capturing method for multi-phase flows. Like VOF, LSM employs a scalar function rather than Lagrangian particles, thereby circumventing the computational expense that hinders methods such as MAC. It was originally proposed by Osher and Sethian [1988] and was developed for the computation and analysis of the motion of an interface between two fluid phases in two or three dimensions. In the LSM the interface is represented by the zero set of a smooth distance function, ϕ , that is defined for the entire physical domain. The conservation equations are solved for both liquid and gas phase and the interface is advected according to the local velocity vector.

The LSM method has proven a very versatile approach, capable of computing geometrically complex surfaces involving corners and cusps, and can deal with rapidly changing topologies robustly. Furthermore it can be generalised to three-dimensional problems relatively easily (Chang et al. [1996]).

Within the field of hydraulics, Yue et al. [2005] employed the LSM in LES of turbulent open channel flow over fixed dunes. The relative submergence was 6.6 and therefore significantly higher than in the VOF study of Xie et al. [2014]. It was observed that the method was able to accurately and realistically calculate the unsteady free-surface motion and also provided evidence of boils, upwelling and downdraft at the water surface. Suh et al. [2011] report results from LES of flow past a vertical circular cylinder that protruded from the water surface. The LSM was used to capture the water surface dynamics and it was observed that the classic Karman-type vortex shedding is attenuated in the near-surface region, to be replaced by much smaller vortices. Kara et al. [2015b] performed LES of flow through a submerged bridge with overtopping, using LSM to capture the free-surface dynamics. The simulation revealed very complex flow phenomena, including a plunging nappe and standing wave at the surface downstream of the bridge, a horizontal recirculation in the wake of the lateral abutment and

2. LITERATURE REVIEW

vertical recirculation created by the plunging flow. The simulation results agreed very well with complementary experimental measurements in terms of the water surface deformation. [Kang and Sotiropoulos \[2015\]](#) performed a LES of open channel turbulent flow over a river restoration scheme, also using the LSM for the free-surface capture, on a curvilinear grid. Good agreement with experimental data was observed in terms of mean velocities and turbulence statistics, and the method was shown to be capable of capturing very complex flow dynamics downstream of the structure, including a standing wave that was characterised by very high levels of near-surface turbulence.

As mentioned earlier, a difficulty commonly associated with front capturing techniques is how to maintain the interface thickness while satisfying mass conservation. For the LSM, the specific problem is that, although ϕ should remain a signed distance function at all times, advection due to the local velocity vector naturally acts to distort the function. The LSM overcomes this difficulty by using re-initialisation techniques, which involve resetting the ϕ field at regular intervals, thereby ensuring that it remains a signed distance function with the same zero level set. The first of these re-initialisation techniques was proposed by [Sussman et al. \[1994\]](#), with subsequent modifications developed by [Peng et al. \[1999\]](#), [Russo and Smereka \[2000\]](#) and [Sussman and Puckett \[2000\]](#), among others. The re-initialisation can, however, result in numerical errors and the introduction of numerical oscillations in the free-surface ([Griebel and Klitz \[2017\]](#)).

In recent years a number of efforts have been made to improve the mass conservation properties of the LSM by coupling it with other techniques to form so-called hybrid methods. [Enright et al. \[2002\]](#), for example, derived a particle level set method (PLSM) that used Lagrangian marker particles to reconstruct the interface in regions of poor resolution, finding that its mass conservation and interface resolution quantities were comparable to those of VOF and pure Lagrangian methods respectively. A hybrid method that has shown promise in recent years is the coupled level set volume of fluid (CLSVOF) method ([Wang et al. \[2008\]](#)), which has been shown to perform better than the PLSM for simulations of practical engineering flows ([Ménard et al. \[2007\]](#); [Wang et al. \[2012\]](#)).

2. LITERATURE REVIEW

Chapter 3

Numerical Framework

3.1 Large Eddy Simulation

Turbulence is a multiscale phenomenon with a wide spectrum of scales of the fluid motion. The idea of LES is to calculate explicitly the motion of large scale eddies by solving the governing 3D Navier-Stokes equations and to model the motions of the small scales. Fig. 3.1 illustrates the concept of LES in relation to energy flux and energy spectrum. The large scales extract energy from the mean flow (production zone) and transfer it to smaller scales in the energy cascade, and at the smaller scales, the kinetic energy is withdrawn by the mechanism of dissipation (Rodi et al. [2013]). The $k_{cut-off}$ vertical dashed line (Fig. 3.1 bottom) which defines the separation between large eddies and small scale turbulence is achieved via spatial filtering introduced by Leonard [1975]. This filtering is based on the assumption that the small scales are isotropic and thus easier to model than the large scales which are more energetic and anisotropic. In LES, the general rule of spatial filtering is that the filter width is equal to the grid size, and those turbulent scales smaller than the grid size are modelled, using a subgrid-scale (SGS) model. Considering medium-to-high Reynolds number flows, the resolution of the spatial and temporal flow scales requires extremely fine grids and small time steps. This approach is well-known as Direct Numerical Simulation (DNS) which computes the full spectrum of turbulent scales without introducing

any model. However, such high demand of computational power is deemed to be impractical in the current state of supercomputing technology. On the other end of the spectrum, the Reynolds-averaged Navier-Stokes (RANS) method, all fluctuations are (time-)filtered/averaged out and only mean-flow quantities are solved; and when the mean flow is unsteady, the method is called URANS and the time-filtering/averaging removes only the turbulent fluctuations, but not the lower-frequency unsteadiness of the mean flow (Rodi et al. [2013]). LES being in the middle ground in terms of accuracy and computational demand has gained its popularity in this research field.

3.2 Governing Equations

The in-house code HYDRO3D is the numerical model used in this study which has been validated thoroughly for many internal and external flows (Bomminayuni and Stoesser [2011]; Cevheri et al. [2016]; Fraga and Stoesser [2016]; Fraga et al. [2016]; Liu et al. [2016]; McSherry et al. [2018]; Ouro et al. [2017]; Stoesser [2010]; Stoesser and Nikora [2008]; Stoesser et al. [2015]). Hydro3D solves the incompressible, filtered Navier-stokes equations which read

$$\frac{\partial u_i}{\partial x_i} = 0 \tag{3.1}$$

$$\frac{\partial u_i}{\partial t} + \frac{\partial u_i u_j}{\partial x_j} = -\frac{\partial p}{\partial x_i} + \frac{1}{Re} \frac{\partial^2 u_i}{\partial x_i \partial x_j} - \frac{\partial \tau_{ij}}{\partial x_j} \tag{3.2}$$

where x_i and x_j are the spatial location vectors (i.e. x_i and $x_j = x, y$ for i and $j = 1, 2, 3$), u_i, u_j ($i, j = 1, 2, 3$) are the resolved velocity components in x - and y -directions, normalised on the reference velocity U and p is the resolved pressure divided by density. $Re = UL/\nu$ is Reynolds number, where ν is the kinematic viscosity and L is the reference length scale.

The SGS stress, τ_{ij} , arises from unresolved small scale fluctuations and is approximated using the wall-adapting local eddy (WALE) viscosity model introduced by Nicoud and Ducros [1999]. The WALE SGS model has several advantages over

3. NUMERICAL FRAMEWORK

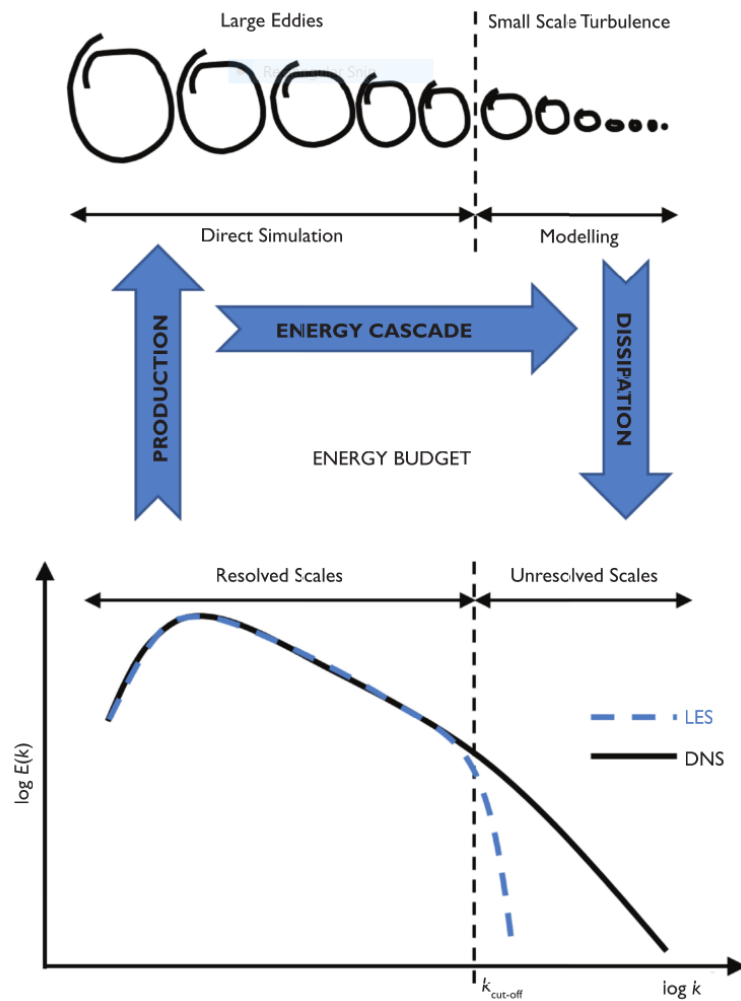


Figure 3.1: Concept of Large Eddy Simulation in relation to energy flux and energy spectrum (adapted from Breuer [2002])

3. NUMERICAL FRAMEWORK

the classic Smagorinsky model and are listed as follow:

- the model consists of a mixing of both the local strain and rotation rates. Thus, all the turbulence structures relevant for the kinetic energy dissipation are detected by the model,
- the eddy-viscosity goes naturally to zero in the vicinity of a wall so that neither (dynamic) constant adjustment nor damping function are needed to compute wall bounded flow,
- the model produces zero eddy viscosity in case of a pure shear. Thus, it is possible to reproduce the laminar to turbulent transition process through the growth of linear unstable modes,
- the model is invariant to any coordinate translation or rotation and only local information (no test-filtering operation, no knowledge of the closest points in the grid) are needed. Thus, it is suitable for LES in complex geometries.

The final point is particularly important as the WALE model is well-suited to simulations in which solid boundaries are not sharply defined, such as those performed using the Immersed Boundary Method (IBM) as is the case in the present study.

The eddy viscosity, ν_T , is calculated as follows:

$$\nu_T = (C_w \Delta)^2 \frac{(s_{ij}^d s_{ij}^d)^{\frac{3}{2}}}{(\overline{S_{ij} S_{ij}})^{\frac{5}{2}} + (s_{ij}^d s_{ij}^d)^{\frac{5}{4}}} \quad (3.3)$$

where C_w is a constant with a value 0.46 and Δ is the subgrid characteristic length scale. The traceless symmetric part of the square of the velocity gradient tensor, s_{ij}^d is computed in the following form:

$$s_{ij}^d = \frac{1}{2}(\overline{g_{ik} g_{kj}} + \overline{g_{jk} g_{ki}}) - \frac{1}{3}(\delta_{ij} \overline{g_{kk}})^2 \quad (3.4)$$

3. NUMERICAL FRAMEWORK

where $\overline{g_{ij}} = \frac{\partial \overline{u_i}}{\partial x_j}$ and δ_{ij} is the Kronecker symbol. $\overline{S_{ij}}$ is the rate-of-strain tensor for the resolved scale defined by:

$$\overline{S_{ij}} = \frac{1}{2} \left(\frac{\partial \overline{u_i}}{\partial x_j} + \frac{\partial \overline{u_j}}{\partial x_i} \right) \quad (3.5)$$

The diffusive terms in the Navier-stokes equations are approximated by fourth-order central differences while convective fluxes in the momentum and level-set equations (will be introduced in the level set method section) are approximated using a fifth-order weighted, essentially non-oscillatory (WENO) scheme introduced by [Jiang and Shu \[1996\]](#). The main advantage of the WENO scheme is its capability to achieve arbitrarily high order formal accuracy in smooth regions while maintaining stable, non-oscillatory and sharp discontinuity transitions. The schemes are thus especially suitable for problems containing both strong discontinuities and complex smooth solution features. [Rodi et al. \[2013\]](#) state that the accuracy and credibility of a code can be justified by the use of high-order spatial discretization schemes together with sufficiently fine grids.

3.3 Fractional-step method

The spatially filtered Navier-Stokes equations in the LES framework presented in the Eq. 3.1 and Eq. 3.2, normalised by Reynolds number, Re , are advanced in time using the so-called fractional-step method based on the projection method developed by [Chorin \[1968\]](#). The main advantage of this method is that the velocity and pressure computations are decoupled. This numerical code solves the fluid in a staggered Cartesian rectangular grid in which velocity vectors are stored at the middle of the cell faces while the pressure is stored in the cell centre. The fractional-step method comprises of two steps [Kim and Moin \[1985\]](#). In the first step, the intermediate velocities, u_i^* , are initially predicted without enforcing the incompressibility constraint using a two-stage explicit Runge-Kutta method as follows:

3. NUMERICAL FRAMEWORK

$$u_i^{*,n+\frac{1}{2}} = u_i^n + \frac{\Delta t}{2} \left[R^n - \frac{\partial}{\partial x_i} p^{n-\frac{1}{2}} \right] \quad (3.6)$$

$$u_i^{*,n+1} = u_i^n + \Delta t \left[R^{*,n+\frac{1}{2}} - \frac{\partial}{\partial x_i} p^{n-\frac{1}{2}} \right] \quad (3.7)$$

where

$$R = \left[-\frac{\partial(u_i u_j)}{\partial x_j} + \left(\frac{1}{Re} + \nu_T \right) \frac{\partial^2 u_i}{\partial x_i \partial x_j} \right]. \quad (3.8)$$

In the second step, the intermediate velocities are projected onto the divergence-free vector fields through a Poisson equation, which calculates a projection scalar function, δp :

$$\nabla^2(\delta p) = \frac{1}{\Delta t} \frac{\partial}{\partial x_i} u_i^{*,n+1} \quad (3.9)$$

where ∇^2 is the Laplacian operator. Eq. 3.9 is solved iteratively using the multigrid method [Ferziger and Peric \[2002\]](#), and the velocity field is updated as follows:

$$u_i^{n+1} = u_i^{*,n+1} - \Delta t \frac{\partial(\delta p)}{\partial x_i} \quad (3.10)$$

$$p^{n+\frac{1}{2}} = p^{n-\frac{1}{2}} + \delta p \quad (3.11)$$

The Poisson equation is then solved with this new pressure, and an iterative process is established. The iteration continues until the divergence-free condition of the computed velocity field within some tolerance is satisfied. This stability of the model is ensured by enforcing the Courant-Friedrichs-Lewy condition (CFL

3. NUMERICAL FRAMEWORK

condition) in which it asserts that the numerical flow speed of $\Delta x/\Delta t$ must be at least as fast as the physical flow speed $|u|$, i.e., $\Delta x/\Delta t > |u|$. As a common conservative practice, the CFL number, α ($0 < \alpha < 1$) is used to enforce the safety condition and the three-dimensional CFL number, α can be written as

$$\Delta t \max \left[\frac{|u|}{\Delta x} + \frac{|v|}{\Delta y} + \frac{|w|}{\Delta z} \right] < \alpha = 1 \quad (3.12)$$

3.4 Level set method

The level set method introduced by [Osher and Sethian \[1988\]](#) is used to capture the free-surface. The LSM employs a level set signed distance function, ϕ , which has zero value at the phase interface and is negative in air and positive in water. The method is formulated as:

$$\phi(x, t) < 0 \quad \text{if} \quad x \in \Omega_{gas} \quad (3.13)$$

$$\phi(x, t) = 0 \quad \text{if} \quad x \in \Gamma \quad (3.14)$$

$$\phi(x, t) > 0 \quad \text{if} \quad x \in \Omega_{liquid} \quad (3.15)$$

where Ω_{gas} and Ω_{liquid} represent the fluid domains for gas and liquid, respectively, and Γ is the interface. The interface moves with the fluid particles, expressed through a pure advection equation of the form

$$\frac{\partial \phi}{\partial t} + u_i \frac{\partial \phi}{\partial x_i} = 0 \quad (3.16)$$

Since density and viscosity are constant along the particle paths for immiscible fluids, discontinuities in these properties at the interface will cause numerical instabilities. This is avoided by the introduction of a transition zone in which density and viscosity switch smoothly between water and air. The transition zone is defined as $|\phi| \leq \epsilon$ where ϵ is half the thickness of the interface, which in

3. NUMERICAL FRAMEWORK

this study is two grid spacings. A Heaviside function, $H(\phi)$, accomplishes the transition as follows [Osher and Fedkiw \[2003\]](#)

$$\rho(\phi) = \rho_g + (\rho_l - \rho_g)H(\phi), \quad (3.17)$$

$$\mu(\phi) = \mu_g + (\mu_l - \mu_g)H(\phi) \quad (3.18)$$

where ρ_l and ρ_g are the density of liquid and gas, respectively; μ_l and μ_g are the dynamic viscosity of liquid and gas, respectively.

$$H(\phi) = 0 \quad \text{if } \phi < -\epsilon \quad (3.19)$$

$$H(\phi) = \frac{1}{2} \left[1 + \frac{\phi}{\epsilon} + \frac{1}{\pi} \sin\left(\frac{\pi\phi}{\epsilon}\right) \right] \quad \text{if } \phi \leq \epsilon \quad (3.20)$$

$$H(\phi) = 1 \quad \text{if } \phi > \epsilon \quad (3.21)$$

LSM is known to have difficulties in conserving mass for strongly distorted interfaces due to numerical dissipation introduced in the discretisation of Eq. [3.16](#) when using upwind biased schemes. Because this is a pure advection problem, central differencing schemes are unstable. Therefore, as mentioned in the previous section, a fifth-order WENO scheme is used to minimise the numerical dissipation. Another difficulty with LSM is that ϕ does not maintain its property of $|\nabla\phi| = 1$ as time proceeds. To overcome this problem, a re-initialisation technique introduced by [Sussman et al. \[1994\]](#) is employed, which also helps in improving mass conservation issues. The re-initialised signed distance function d is obtained by solving the partial differential equation given by

$$\frac{\partial d}{\partial t_a} + s(d_0)(|\nabla d| - 1) = 0 \quad (3.22)$$

where $d_0(x, 0) = \phi(x, t)$, t_a is a dummy parameter and $s(d_0)$ is the smoothed signed function given as

$$s(d_0) = \frac{d_0}{\sqrt{d_0^2 + (|\nabla d_0| \epsilon_r)^2}} \quad (3.23)$$

This re-initialisation is applied throughout the transition zone within several iteration steps, $\epsilon_r/\Delta t_a$ where ϵ_r represents one grid space. Those adjustments to level set function are employed only for computational cells lying on the interface, so that there is no need to solve the partial differential equation for the whole domain.

3.5 Immersed boundary method

The immersed boundary (IB) method was originally developed by [Peskin \[1972\]](#) with the aim at developing a methodology for the simulation of heart valves. Peskin developed a non-body conformal methodology that constituted a computationally cheap while accurate approach to biomechanical flows. In the 1990s, the popularity of IB method increased notably as the research community explored new improvements onto the method so as to enlarge its range of applications and accuracy. The main advantages of using IB method are: a) the capability to combine with structured meshes (usually rectangular Cartesian mesh) which allows the use of efficient flow solvers, such as fast Poisson equations ([Sotiropoulos and Yang \[2014\]](#)); and b) the relatively low computational cost compared to body-fitted models as highlighted by [Fadlun et al. \[2000\]](#).

There are mainly two IB method varieties: the continuum and discrete approaches. The continuum models use the geometrical description of a continuous surface to project the velocities over the normal vector to the body surface. It usually involved the categorisation of the Eulerian cells into solid, fluid or intermediate ([Kang et al. \[2012\]](#)). In the present study, the discrete approach is adopted. The discrete models are those where the body is built as a set of individual Lagrangian points that conform its shape. [Fig. 3.2](#) exhibits a two-dimensional representation of a staggered grid with uniform grid spacings (Δx & Δy) and Lagrangian markers (red circles). [Uhlmann \[2005\]](#) developed the direct forcing (DF)

3. NUMERICAL FRAMEWORK

method using delta functions to essentially form a two-way interpolation procedure between the Eulerian cells and Lagrangian cells where information between the fluid and solid frameworks are exchanged.

The direct forcing method follows a multi-step predictor-corrector procedure, which is adapted as follows: first, the predicted Eulerian velocities (u^*) are calculated from Eq. 3.7. A delta function (δ) is used as an interpolation function to transfer u^* onto the Lagrangian grid from its closest number of Eulerian neighbours, n_e (filled black symbols in Fig. 3.2) and the interpolated Lagrangian velocity, U_L is obtained:

$$U_L = \sum_{ijk=1}^{n_e} u_{ijk}^* \cdot \delta(x_{ijk} - X_L) \cdot \Delta x_{ijk} \quad (3.24)$$

where x_{ijk} is the vector of coordinates of the Eulerian mesh cells ijk . $X_L = (X_L, Y_L, Z_L)^T$ is the location of the Lagrangian marker, L and $\Delta x_{ijk} = \Delta x \cdot \Delta y \cdot \Delta z$ is the Eulerian cell volume.

The interpolating delta function is calculated from the multiplication of three one-dimensional kernel, ϕ as shown:

$$\delta(x_{ijk} - X_L) = \frac{1}{\Delta x_{ijk}} \phi\left(\frac{x_{ijk} - X_L}{\Delta x}\right) \phi\left(\frac{y_{ijk} - Y_L}{\Delta y}\right) \phi\left(\frac{z_{ijk} - Z_L}{\Delta z}\right) \quad (3.25)$$

The one-dimensional kernel, ϕ are chosen carefully to avoid large oscillations on the force outputs. In the present publication, a kernel which uses 64 neighbouring cells are chosen.

The second step of the DF method is to compute the force F_L that each Lagrangian markers needs to exert on the fluid to satisfy the no-slip condition at the marker's position. The force term is calculated as the difference between the desired velocity at the marker, U_L^* , and the velocity previously interpolated from the fluid mesh, U_L . In the case of a static body, the desired velocity at the marker, U_L^* is zero.

3. NUMERICAL FRAMEWORK

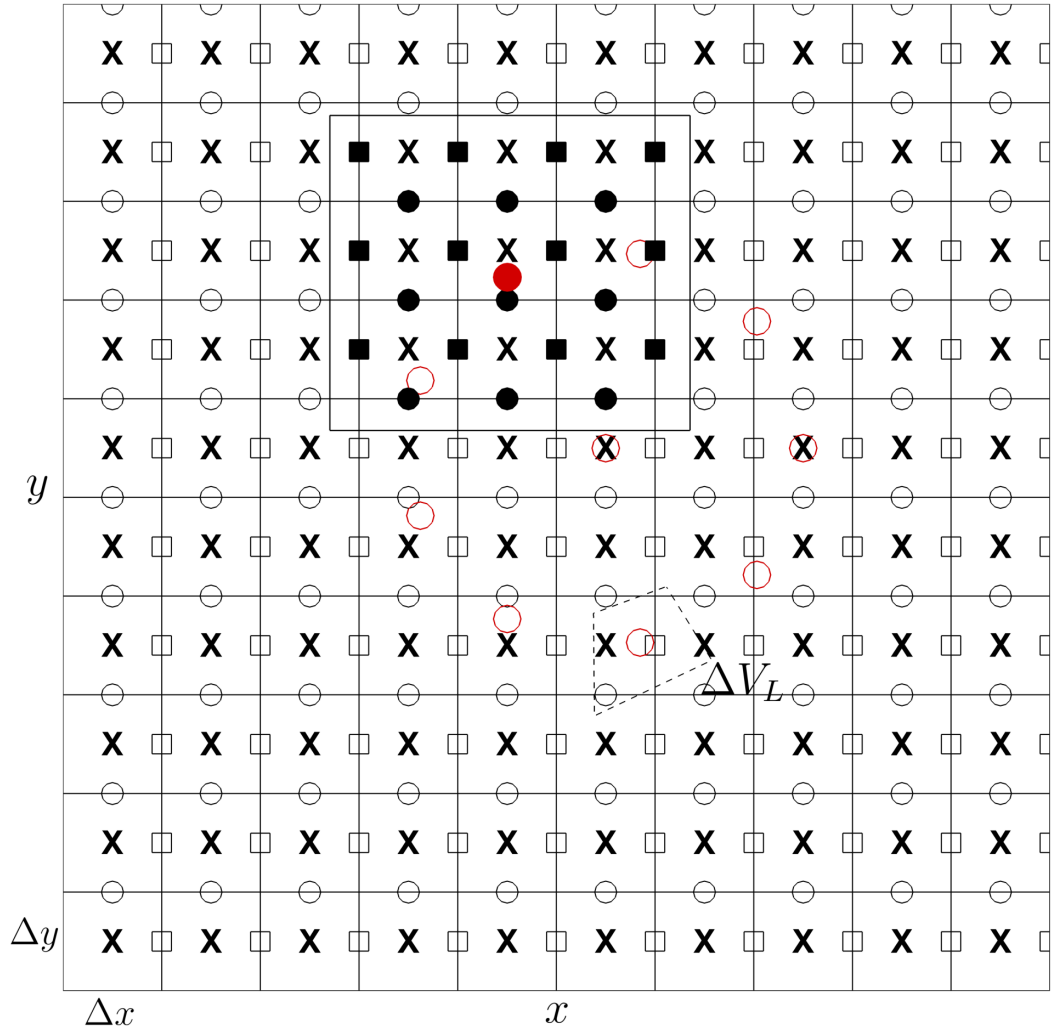


Figure 3.2: Two-dimensional representation of the Cartesian staggered grid. The neighbours used in the interpolation for a Lagrangian marker (filled red circle) are the black-filled symbols within the square boundary. x represents pressure nodes, \square are x-velocity nodes, \circ are y-velocity nodes, and red circles are the Lagrangian markers. ΔV_L denotes the Lagrangian marker volume.

3. NUMERICAL FRAMEWORK

$$F_L = \frac{U_L^* - U_L}{\Delta t} \quad (3.26)$$

The third step constitutes the backwards procedure where the Lagrangian force is transferred back to the Eulerian mesh cells in order to obtain the Eulerian force, f . The same delta function as Eq. 3.25 is used to reverse interpolate F_L from the closest Lagrangian markers, n_L to each Eulerian cell and is performed as:

$$f(x_{ijk}) = \sum_{L=1}^{n_L} F_L \cdot \delta(X_L - x_{ijk}) \cdot \Delta V_L \quad (3.27)$$

where ΔV_L is the Lagrangian volume, which should be approximately equal to Δx_{ijk} .

In the final corrector step, the predicted Eulerian velocity, u^* is updated with the Eulerian force from the IB method correction as follows:

$$\tilde{u}^* = u^* + f\Delta t \quad (3.28)$$

3. NUMERICAL FRAMEWORK

Chapter 4

Level Set Method Validation

Case¹

4.1 Objectives

The aim of the present chapter is to investigate the validity of the use of level set method (LSM) as an interface capturing tool for the water surface. Large eddy simulations (LES) and complementary experiments were carried out on six flow cases, with varying relative submergence and k-type and transitional (between d-type and k-type) roughness types. The bed roughness is introduced by submerged spanwise square bars mounted on the bed. d-type roughness is characterized by stable separated vortices occupying the entire cavity between roughness elements while k-type roughness entails a mean recirculation bubble in the wake of the roughness elements, with reattachment to the bed occurring between successive elements (Stoesser and Rodi [2004]). LES-computed results are compared to complementary experimental results by means of temporal and spanwise mean free surface elevation and temporal and spanwise mean streamwise velocity. Contours of the temporal and spanwise mean streamwise velocity and streamfunction of the six flow cases are presented.

¹Results from this chapter are directly adopted from the 2nd journal paper listed in the section of related publications.

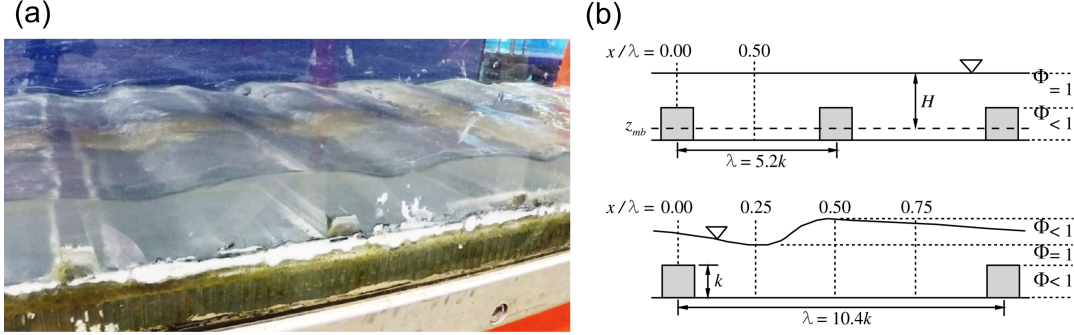


Figure 4.1: Experimental set-up. (a) the flume equipped with square bars, (b) the two geometries, with velocity measurement locations denoted by dashed lines.

4.2 Experimental set-up

Experiments were carried out in a 10m long, 30cm wide glass-walled recirculating flume in the Hyder Hydraulics Laboratory at Cardiff University. A series of plastic square bars 30 cm wide with cross-section 12 mm \times 12 mm were installed along the length of the flume, perpendicular to the direction of mean flow (Fig. 4.1). The roughness height, k , was therefore 12 mm. Two different bar spacings were investigated, $\lambda = 62.5$ mm and $\lambda = 125$ mm, corresponding to the normalised spacings $\lambda/k = 5.2$ and $\lambda/k = 10.4$ respectively. According to Coleman et al. [2007], the $\lambda/k = 5.2$ case should be classified as transitional roughness as it is very close to the boundary between d - and k -type roughnesses, while the $\lambda/k = 10.4$ case constitutes k -type roughness. Bed slope was fixed at 1:50 for all experiments and three flow rates, Q , were tested for each bar spacing (1.7, 2.5, 4.0 l/s), giving a total of six experimental cases. Each case had a different relative submergence, H/k , where H is the double-averaged depth, defined as the distance between the spatial and temporal mean water surface position and the spatial mean bed elevation, z_{mb} . The double-averaged bulk velocity, $U_b (= Q/H)$, ranged from 0.20 m/s to 0.36 m/s. Note that the angular brackets and overbar have not been used for H and U_b in the interest of simplicity. Table 4.1 provides a summary of the flow conditions. In all cases the aspect ratio, B/H , was sufficiently large to ensure either that the flow was two-dimensional or that any secondary flows were weak and that their influence on the mean flow could be neglected.

4. LEVEL SET METHOD VALIDATION CASE

Case	λ/k	H/k	B/H	λ/H	$U_b(m/s)$	Re	Re_τ	Fr	L_x/H	L_y/H	Δx^+	Δy^+	Δz^+
C1	5.2	2.2	11.6	2.4	0.22	5.7×10^3	1.8×10^3	0.43	4.8	2.3	69.9	66.8	35.6
C2	5.2	2.5	10.0	2.1	0.28	8.3×10^3	2.3×10^3	0.51	4.2	2.0	75.1	71.8	38.8
C3	5.2	3.1	8.0	1.7	0.36	13.3×10^3	3.2×10^3	0.59	3.4	1.6	83.8	80.2	42.8
C4	10.4	2.4	10.5	4.4	0.20	5.7×10^3	2.1×10^3	0.38	4.4	2.1	73.2	70.0	37.4
C5	10.4	2.9	8.8	3.6	0.24	8.3×10^3	2.8×10^3	0.42	3.7	1.8	80.3	76.9	41.0
C6	10.4	3.4	7.3	3.0	0.32	13.3×10^3	3.7×10^3	0.51	3.0	1.5	88.2	84.3	45.0
F1	5.2	2.5	10.0	2.1	0.28	8.3×10^3	2.3×10^3	0.51	4.2	2.0	37.5	35.9	19.1
F2	10.4	2.4	10.5	4.4	0.20	5.7×10^3	2.1×10^3	0.38	3.7	1.8	36.6	35.0	18.7
F3	10.4	2.9	8.8	3.6	0.24	8.3×10^3	2.8×10^3	0.42	3.7	1.8	40.2	38.4	20.5
D1	10.4	2.9	8.8	3.6	0.24	8.3×10^3	2.8×10^3	0.42	7.4	3.6	80.3	76.9	41.0

Table 4.1: Hydraulic conditions and computational details.

Measurements of instantaneous velocity and free surface position were taken in a section of the flume where the flow was considered to be uniform and fully-developed. The flow was also considered to be spatially periodic with wavelength λ in the streamwise direction, that is to say the temporal mean values of all flow variables in successive cavities between bars were considered to be the same. The bulk Reynolds number ($= U_b H / \nu$) was in the range $5700 \leq \text{Re} \leq 13000$ and the friction Reynolds number $\text{Re}_\tau (= u_* H / \nu)$ where u_* is the global friction velocity based on the bed shear stress, was in the range $1.8 \times 10^3 \leq \text{Re}_\tau \leq 3.7 \times 10^3$. The global Froude number of the flows, $\text{Fr} = (U_b / \sqrt{gH})$, was in the range $0.38 \leq \text{Fr} \leq 0.59$; local values based on local depths and velocities can be much higher.

A Nixon Flowmeters propeller meter (accuracy of $\pm 1.5\%$) was used to measure streamwise velocities along the channel centreline, at two streamwise positions for the $\lambda/k = 5.2$ case and four streamwise positions for the $\lambda/k = 10.4$ case. At each streamwise location the velocity was measured at between four and eleven discrete depths, to reveal vertical velocity profiles. At each depth, measurements were taken during 120 seconds at a sampling frequency of 1 Hz; 120 samples of instantaneous velocity were therefore available, from which the temporal mean was calculated.

Water surface position was measured using high speed photography with illuminated seeded particles. A Baumer TXG14F CCD camera was used in conjunction with a Polytec BUS-11 Wotan Flash stroboscope and a halogen lamp to capture the dynamic free surface. Seeding particles that had the same approxi-

4. LEVEL SET METHOD VALIDATION CASE

mate density of water, making them neutrally buoyant, were used. The camera was positioned at one side of the flume, level with the mean water surface position, and recorded images during 50 seconds for each flow case, at a rate of 30 frames per second. Figure 4.2a presents an example of one such image that was taken for the $\lambda/k = 10.4$, $H/k = 2.9$ flow case. Each recording therefore comprised 1500 individual frames, which were then digitally processed using pixel recognition software to reveal the x - z coordinates of the free surface at the channel sidewall at each time instant. These data were then averaged to give a temporal mean of the water surface position. Figure 4.2a presents an individual frame from one of the cases, showing the instantaneous water surface deformation. It should be noted that the free surface elevation recorded by this technique was somewhat different from the elevation observed in the centre of the channel due to Meniscus effects that were observed at the sidewalls. This has the effect of thickening the appearance of the free surface and “smearing” the profiles of the standing waves that occurred in the $\lambda/k = 10.4$ cases.

In addition to the data that was derived from the photographs, a point gauge was used to measure water surface elevations at several locations along the channel centreline. The point gauge has an accuracy of $\pm 0.1\text{mm}$. Measurements were taken over a length spanning two or more cavities, at streamwise intervals of between 2.5 mm and 10 mm. Point gauge measurements were taken for all flow cases except C6, which was characterised by an extremely dynamic free surface with significant spanwise wandering of the hydraulic jump, and it was therefore impossible to measure water surface with a point gauge.

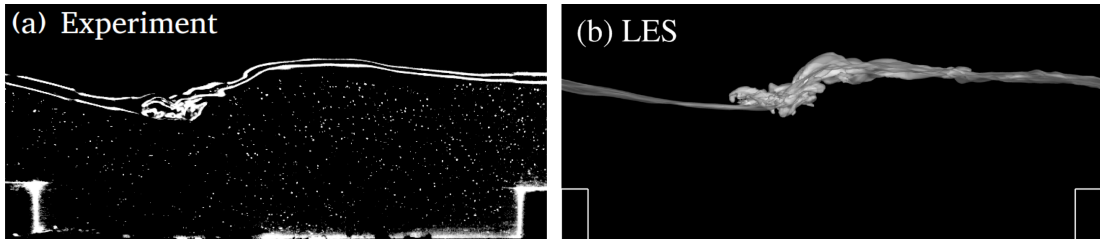


Figure 4.2: (a) Post-processed camera image from side view and (b) visualisation of 3D instantaneous free surface profiles from side view for LES results, $\lambda/k = 10.4$, $H/k = 2.4$.

4.3 Numerical setup

In total ten LES of flows over transverse square bars have been performed. Computational details are provided in Table 4.1. Cases C1 to C6 correspond to the six experimental flow cases that were described in the previous section and were performed on a reasonably coarse grid. Cases F1 to F3 correspond to three selected flow cases and were performed on a fine grid to investigate the sensitivity of the results to grid resolution. Figure 4.3 presents the computational domains that were used for these first nine simulations; for the $\lambda/k = 5.2$ cases the domain spanned two cavities while in the $\lambda/k = 10.4$ cases it spanned only one cavity. For both λ/k values the length of the domain, L_x , was $10.4k$ while the width, L_y , and height, L_z , were both $5k$. In the coarse grid the number of uniformly-spaced computational points in the streamwise direction, N_x , was 128; in the spanwise direction the number of points, N_y , was 64, and the number of points in the vertical direction, N_z , was 120. The total number of computational points was therefore approximately 9.8×10^5 . The fine grid was discretised with $256 \times 128 \times 240$ ($= 7.8 \times 10^6$) computational points.

Figure 4.3 includes isosurfaces showing the instantaneous free surface positions at two arbitrary moments in time, for two example simulations (C2 and C5). The figure shows that the domain extended higher than the free surface: the volume above the surface was occupied by the air phase, and the volume below was occupied by the water phase. A free-slip boundary condition was applied to the top of the domain while a no-slip condition was stipulated on the channel bed. The bars were represented by immersed boundaries, which also achieve an effective no-slip boundary condition on their surfaces (refer to [Cevheri et al. \[2016\]](#) for a rigorous validation). Periodic boundary conditions were applied in the streamwise direction, and the flow was driven by the component of gravitational acceleration parallel to the channel bed, based on the bed slope that was applied in the flume experiments (1:50). The global shear velocity, $u_* (= \sqrt{gSH})$, was therefore exactly the same as in the experiments. As discussed in Section 4.2, the aspect ratio of the experimental cases was large enough to ensure that the influence of the vertical side walls on the mean flow would be negligible, and that secondary currents would be negligibly weak. Periodic boundary conditions were

4. LEVEL SET METHOD VALIDATION CASE

therefore applied on the lateral faces of the computational domain to produce a two-dimensional mean flow with no secondary currents, applying the wide channel assumption.

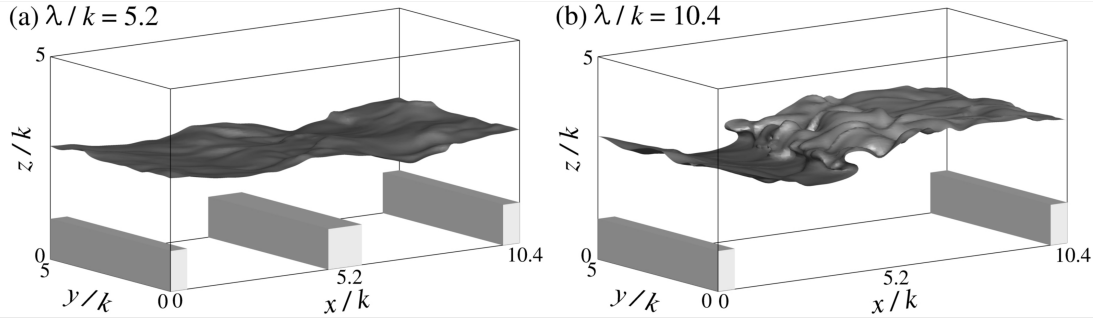


Figure 4.3: Computational domain with instantaneous free surface response. (a) $\lambda/k = 5.2$; (b) $\lambda/k = 10.4$

The domain dimensions, in terms of the mean height of the water surface, H , for each of the cases, are provided in Table 4.1. A tenth simulation, D1, was performed using a coarse grid in a domain that was twice as long and twice as wide as the original domain, so that the effect of domain size on the computation of turbulent structures could be assessed.

In all cases the simulations were started with a planar rigid lid applied at the mean free surface position that was recorded in the experiments. A free-slip boundary condition was stipulated at the rigid lid and the simulation was run for 100,000 time steps, which corresponded to between 10 and 15 flow through periods, $T_f (= L_x/U_b)$, to allow the flow to develop fully. The simulation was then restarted without the rigid lid but with the level set algorithm now activated to track the free surface. Averaging of the flow quantities was begun after 4 to 6 more flow through periods, and continued for between 40 and 60 further flow throughs to ensure that the turbulence statistics were well converged. Further averaging was performed in the homogeneous spanwise direction to obtain a smooth distribution of turbulence statistics. The variables averaged in this way are denoted with an overbar above the corresponding symbols.

In the present study the *volume fraction*, (ϕ) , is defined as the temporal mean of the fraction of the volume in a plane parallel to the mean flow direction that is

occupied by water, i.e. $\phi = V_w/V_o$, where V_w is the temporal mean of the volume of water in the plane and V_o is the overall volume of the plane. In the roughness layer the volume fraction is identical to the *roughness geometry function* defined by Nikora et al. [2001], and takes a value in the range $0.0 < \phi < 1.0$ ($V_w < V_o$), depending on the roughness distribution. In the region immediately above the roughness tops the water occupies the entire volume of the plane ($V_w = V_o$) and therefore $\phi = 1.0$. Due to the spatial heterogeneity of the mean water surface in some of the flow cases (refer to Figs 4.2 and 4.3b), a portion of the volume of a plane parallel to the flow direction may be occupied by the air and the volume of water in the plane may therefore be less than the volume of the plane. In this region the plane volume may be expressed as $V_o = V_w + V_a$, where V_a is the temporal mean of the volume of air in the plane. It follows that $\phi < 1.0$ when $V_a \neq 0.0$.

Figure 4.4 presents vertical distributions of the volume fraction for LES cases C1 to C6. The plots show that, since the roughness elements have a square cross-section, ϕ is constant in the interfacial sub-layer and undergoes a step change as z increases beyond the roughness tops at $z/k = 1$. As z increases towards the water surface, two of the cases (Fig. 4.4b and Fig. 4.4c) display another abrupt step change as ϕ drops from 1.0 to 0.0. This is because the mean water surface in these two cases was flat, so the volume of a plane parallel to the mean flow direction is occupied entirely by water on one side of the surface and entirely by air on the other side. In contrast, in the other four cases ϕ transitions gradually from 1.0 to 0.0 due to the spatial heterogeneity of the mean water surface: the fraction of air in the plane increases with increasing z , until finally no water volume is present.

4.4 Results and Validation

Eq. 4.1 is the formulation to calculate the well-known Darcy-Weisbach friction factor, f for flow in an open channel.

$$\left(\frac{8}{f}\right)^{\frac{1}{2}} = \frac{U_b}{(gHS)^{\frac{1}{2}}} \quad (4.1)$$

4. LEVEL SET METHOD VALIDATION CASE

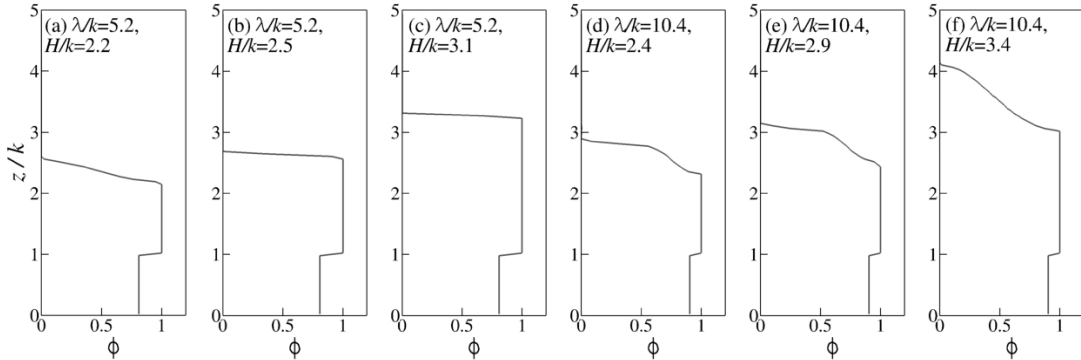


Figure 4.4: Volume fraction vs height above bed for the six LES cases.

where U_b is the bulk flow velocity, g is acceleration due to gravity and S is the bed slope.

Figure 4.5 presents the variation of the friction factor, presented as $(8/f)^{1/2}$ and calculated from Eq. 4.1, with relative submergence for the six cases that have been studied. Flume data from Bathurst [1985] are included for comparison. Note that the Bathurst data correspond to gravel bed roughness and were originally presented in terms of H/d_{84} , where d_{84} corresponds to the 84th percentile used to represent the coarse gravel fraction (i.e., 84% of the gravel elements are smaller than d_{84}). The data has been re-plotted in terms of the equivalent grain roughness, k_s , and the relationship $k_s = 3.5d_{84}$ Dietrich and Whiting [1989] has been used to equate the two measures of roughness height. With regards to the data from the present simulations, the equivalent grain roughness is assumed to be equal to the bar height ($k_s = k$); this relationship is likely to be subject to some error but has been used to permit a crude comparison with the Bathurst flume data. The data lie within the spread of Bathurst's data and agree very well with the general trend of decreasing resistance with increasing relative submergence. Similar to flow over square bars in ducts, for a given submergence, the small bar spacing produces less resistance than the large bar spacing [Leonardi et al., 2003].

Figure 4.2 presents a qualitative comparison of an instantaneous free surface profile recorded by the high speed photography with one computed in the corresponding LES. Although an exact match cannot be expected due to the Meniscus effect that affected the experiments (refer to Section 4.2), the agree-

4. LEVEL SET METHOD VALIDATION CASE

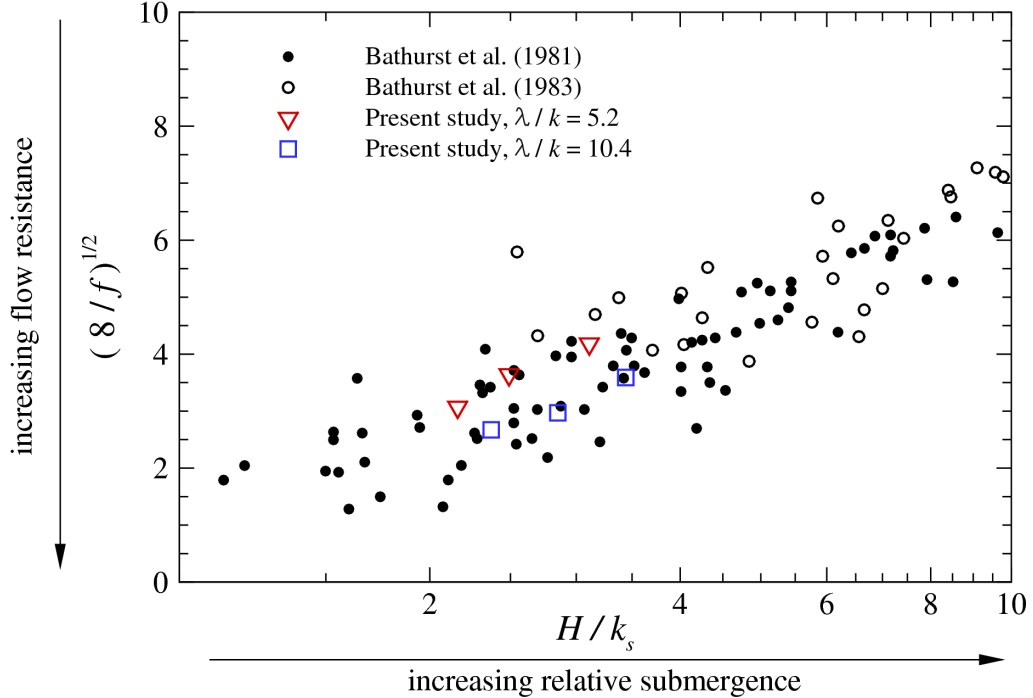


Figure 4.5: Variation of friction factor with relative submergence for the flume experiments.

ment is nonetheless very encouraging. The figure shows that the standing wave is very clear, both in the experiment and in the simulation, and that its height and streamwise position are fairly accurately predicted by the LES.

A more quantitative evaluation of the match between LES and experiment can be achieved with the help of Fig. 4.6, which presents water surface profiles for the six flow cases. Plotted are the spanwise mean of the temporal mean water surface predicted by the LES and the temporal means that were measured using the digitally-processed photographs and the point gauge. Coarse and fine grid LES results are plotted, where available. The agreement between experiments and LES is particularly good for the small spacing ($\lambda/k = 5.2$) cases, and the accuracy of the free surface computation seems not to be affected by grid resolution (Fig. 4.6b). The mean free surface in all three small spacing cases is relatively flat, although some undulation is noticeable in the lowest submergence case (Fig.

4. LEVEL SET METHOD VALIDATION CASE

4.6a). In fact two unsteady undular jumps are present in this flow case, slightly upstream of the bars. These jumps establish and disappear (quasi-) periodically. In the large spacing cases well-defined weak hydraulic jumps are visible between the bars, where the local Froude number approaches unity and the flow becomes critical.

For the low submergence, large spacing case (Fig. 4.6d) the elevation predicted by the coarse grid simulation, C4, is noticeably higher than the measured elevations. This is the result of numerical diffusion and the imperfect approximation of density and viscosity gradients across the boundary that can occur when the Level Set Method is used to simulate complex free surface topologies on coarse grids. Indeed the fine grid simulation, in which the numerical diffusion is lower and the computation of gradients is more precise, produces a very good agreement with the experimental data. The agreement in the medium submergence, large spacing case (Fig. 4.6e) appears to be very convincing for both coarse and fine grids. It is noteworthy that the coarse grid simulation, C5, appears not to suffer from the same problem as C4, even though the complexity of the free surface profiles is similar for both cases.

As stated in Section 4.2, point gauge measurements were not possible in the high submergence, large spacing case (Fig. 4.6f) due to the extremely dynamic nature of the surface and very significant three-dimensionality of the water surface. This dynamic, three-dimensional behaviour is also thought to be the reason for the relatively poor agreement between the LES and the photography data in this case. The periodic boundary conditions that have been applied to the lateral faces of the domain ensure that the mean flow is, by definition, two-dimensional. The spanwise effects that were observed in the experiments due to the presence of the side walls cannot therefore be simulated using this approach. It must therefore be stated that, although the wide channel assumption appears to be valid for the other five flow cases, it may not be valid for C6. Nevertheless some general observations and comparisons can be made from examination of the results. It should also be noted that the spanwise behaviour at the water surface was very dynamic in nature, and may have been the result of an onset of three-dimensional instability at the jump. As no measurements of spanwise and vertical velocity components were possible it is impossible to state with any certainty if significant

4. LEVEL SET METHOD VALIDATION CASE

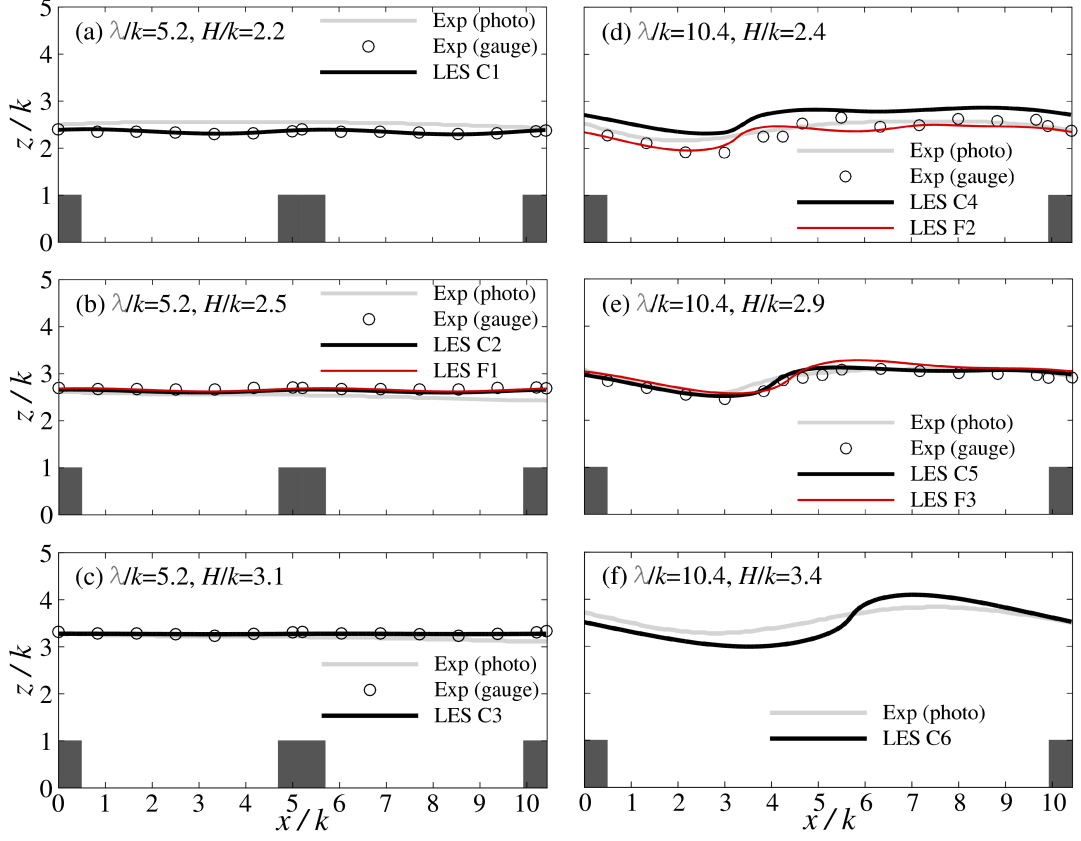


Figure 4.6: Measured and computed longitudinal profiles of temporal and spanwise mean free surface elevation of the six flow cases

secondary currents were present, nor indeed whether or not they were related to the three-dimensionality of the water surface.

Further validation of the LES is provided by vertical profiles of the spanwise and temporal mean of the streamwise velocity from the LES in Figs 4.7 and 4.8, alongside the experimental data, which were recorded at the channel centreline using the Nixon propeller meter. The measurement locations are illustrated in Fig. 4.1: two profiles were measured in the $\lambda/k = 5.2$ cases and four were measured in the $\lambda/k = 10.4$ cases. In general, the LES data from all six cases show good agreement with the experiments. It should be noted that the experimental data points at $z/k = 1$ have been given a filled symbol to highlight the fact that they are possibly less reliable than the others: these points are located in the

4. LEVEL SET METHOD VALIDATION CASE

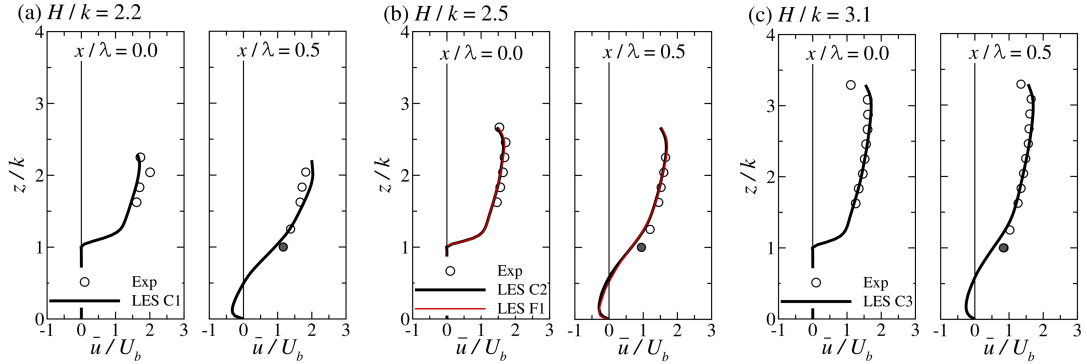


Figure 4.7: Vertical profiles of temporal and spanwise mean streamwise velocity, \bar{u} : $\lambda/k = 5.2$.

shear layer at the top of the roughness elements, and it is known that the Nixon probe is not well suited to regions of high shear and rotation. In addition some of the discrepancy between experimental and numerical results is likely to be due to spatial resolution: in the experiments this is defined by the propeller diameter (comparable to the bar height) while in the LES the spatial resolution is defined by the grid and is therefore much finer than the resolution in the experiments. In the three $\lambda/k = 5.2$ cases significant negative spanwise- and temporally-averaged velocity is observed close to the bed in the middle of the cavity, while there is relatively little streamwise variation in the profiles above the roughness top, indicating a skimming type flow with stable or quasi-stable recirculations in the cavities. In each of the larger spacing cases a region of negative mean velocity is observed near the bed at $\lambda/k = 0.25$ but not at $\lambda/k = 0.5$, suggesting that reattachment to the bed occurs in the upstream half of the cavity. The fine grid simulations, F1, F2 and F3, have been included in the plots and the profiles suggest that the mean velocity predictions are not particularly sensitive to grid resolution.

A more detailed understanding of the flow field can be achieved by considering the contours of spanwise and temporal mean streamwise velocity, \bar{u} , that are presented in Fig. 4.9. For the small spacing, low submergence case (Fig. 4.9a) the contours reveal that the mean water surface is relatively flat. Non-zero contours of mean velocity are observed above the mean water surface, due to the periodic

4. LEVEL SET METHOD VALIDATION CASE

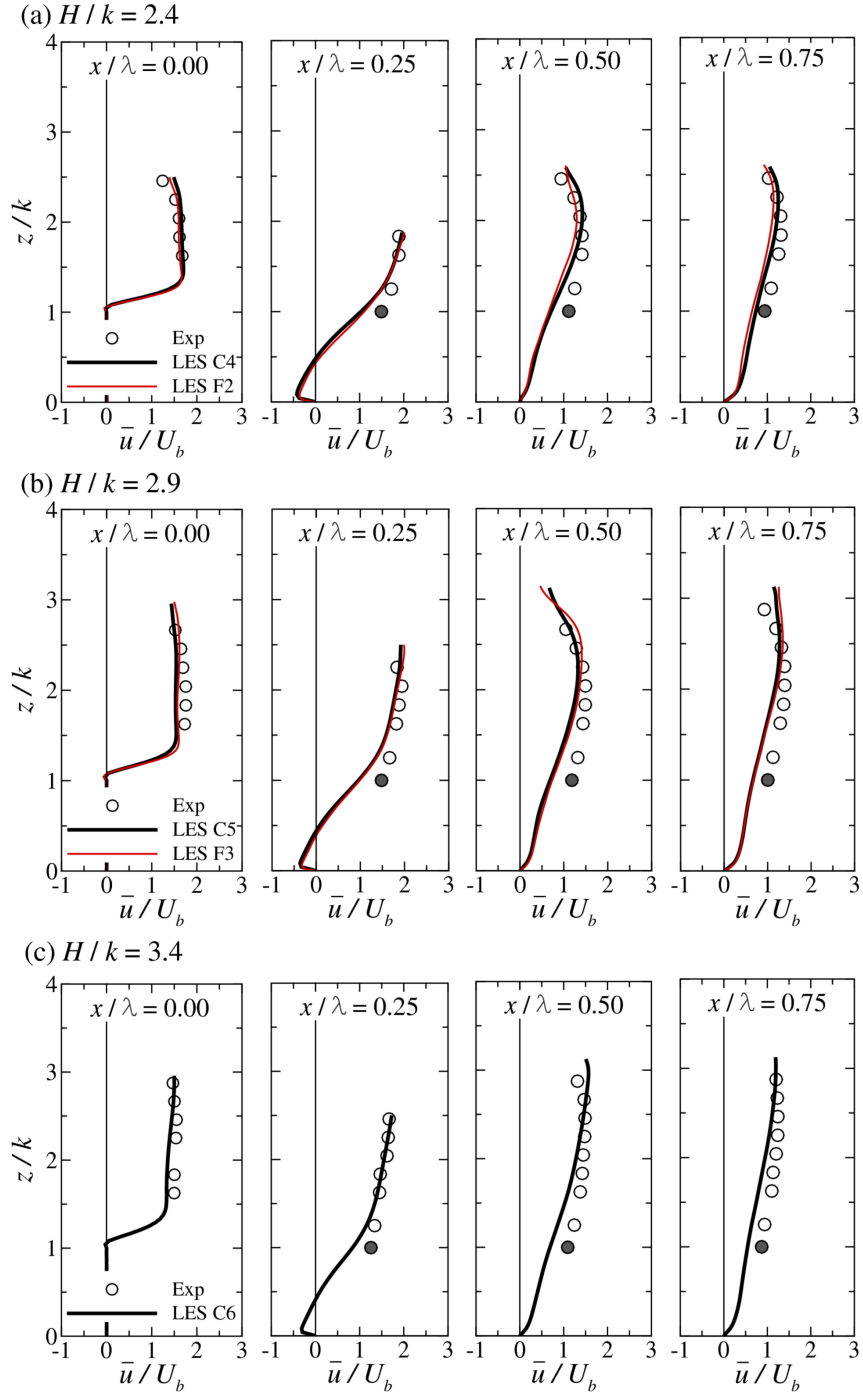


Figure 4.8: Vertical profiles of temporal and spanwise mean streamwise velocity, \bar{u} : $\lambda/k = 10.4$.

4. LEVEL SET METHOD VALIDATION CASE

establishment and disappearance of undular hydraulic jumps just upstream of the bars. When such jumps are present the local water surface rises and a non-zero velocity is observed in the near surface region, contributing to the non-zero mean. Importantly, Fig. 4.9a also shows significant streamwise variation of velocity throughout the depth, with local acceleration and deceleration occurring between and above the bars, respectively. It is worthwhile to note that computation of these phenomena is permitted by the accurate free-surface tracking algorithm employed by the numerical method; the physics would be incorrectly predicted if a standard free-slip rigid slid assumption was used to represent the water surface. In contrast to the shallow small spacing case, the two deeper small spacing cases (Figs 4.9b and c) are characterised by relatively little streamwise variation of velocity above the bars. The plots for the large spacing cases, Figs 4.9d-f, reveal regions of locally-accelerated flow that give rise to local Froude numbers close to 1.0, which in turn lead to dramatic deformations of the water surface and the formation of the hydraulic jumps. The hydraulic jumps are characterised by a small region of negative streamwise velocity produced by the plunging and breaking motion of the standing waves. The plots also confirm the presence of a mean recirculation bubble in the wake of the upstream bar, as well as a small corner vortex at the leading face of the downstream bar.

Figure 4.10 presents contours of the spanwise and temporal mean of the streamfunction, ψ , for the six cases. Note that positive streamfunction is denoted by solid contour lines while dashed lines denote negative streamfunction. The plots confirm the observations noted above regarding the velocity profiles and contours, and also offer some important additional insights. Firstly, the plots clearly show that the close spacing cases are characterised by large recirculations in the cavities, while the mean flow does reattach to the bed in the large spacing cases. The contours also confirm that the $\lambda/k = 5.2$ cases should indeed be classified as transitionally rough, rather than d -type, as the streamlines in the shear layer do not quite connect the top of the elements to create a pseudo-smooth wall, as in [Stoesser and Rodi \[2004\]](#) for example. In fact the $\psi = 0$ contour impinges on the leading faces of the roughness elements, indicating that some form drag will be experienced at the top of the bars and flow in this region will undergo some degree of unsteadiness. Therefore, although the velocity profiles in Fig. 4.7

4. LEVEL SET METHOD VALIDATION CASE

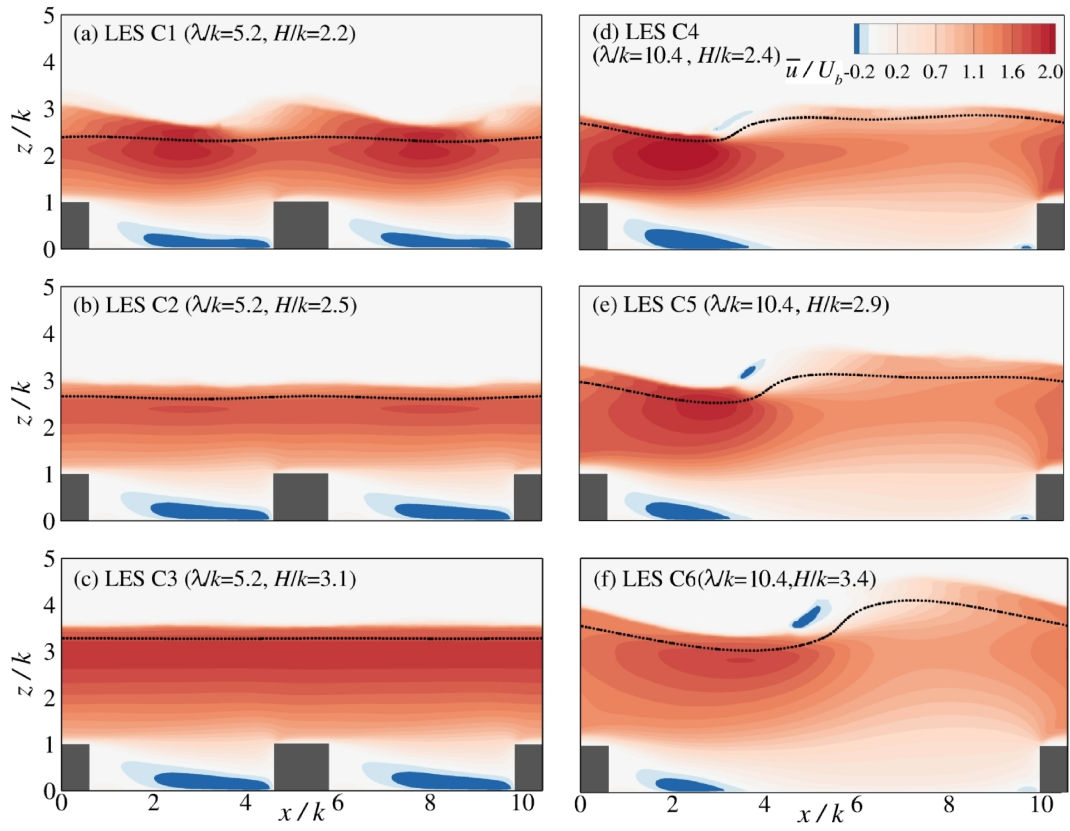


Figure 4.9: Contours of the temporal and spanwise mean streamwise velocity, normalised on bulk velocity for six cases, C1-C6.

4. LEVEL SET METHOD VALIDATION CASE

suggest relatively little streamwise variation in the streamwise velocity, the mean flow field above the roughness crests is not quite homogeneous, as would be the case in a true skimming flow. Instead, it can be considered that the bars present a pseudo-*rough* wall at the crest height, resulting in the streamwise undulations in the streamfunction contours that are visible in the plots. The lowest submergence case (Fig. 4.10a) in particular reveals a somewhat wavy streamfunction field and suggests the presence of a fairly strong undular jump at the free surface, as discussed above with reference to the contours of mean streamwise velocity. In the $\lambda/k = 10.4$ cases the mean flow reattaches to the bed between the bars and can be unequivocally categorised *k*-type roughness. The length of the mean recirculation bubble decreases as submergence increases: this will be discussed in more detail below.

Figure 4.11 illustrates how the wall-normal distance of the first computational point for streamwise velocity, $z^{+l}(= zu_*^l/\nu)$, varies along the length of the computational domain. Here u_*^l is the local friction velocity, calculated using the local shear stress, $\tau^l(= \mu\partial\bar{u}/\partial z)$, and therefore does not account for the form drag acting on the bars. The global friction velocity, $u^*(= \sqrt{gSH})$, does account for the form drag and is expected to be higher than u_*^l . Note that, because the LES are performed on a staggered grid in which the velocities are assigned to the centre of the cell faces, the normalised distance between the wall and the closest u grid point to it is half the cell height, i.e. $\Delta z^+/2$. Based on the cell dimensions given in Table 4.1, this means that the distance from the wall to the closest u grid point is in the range $18 \geq z^+ \geq 23$ for the coarse grids and $9 \geq z^+ \geq 11$ for the fine grids. The plots show, as expected, that the values of z^{+l} are much lower than the corresponding z^+ values. The plots also provide confirmation that at least one computational point is well inside the viscous sub-layer along the length of the domain, indicating that wall-resolved LES have been achieved in every case. Peaks in z^{+l} coincide with peaks in wall shear stress, and for both bar spacings the magnitude of the peak increases with increasing relative submergence. In the small spacing cases one significant peak in z^{+l} is observed on the channel bed, the result of the large quasi-steady vortex in the cavity which produces highly negative velocities in the near-wall region. In the large spacing cases a significant peak is observed in the region that is subject to negative near-wall

4. LEVEL SET METHOD VALIDATION CASE

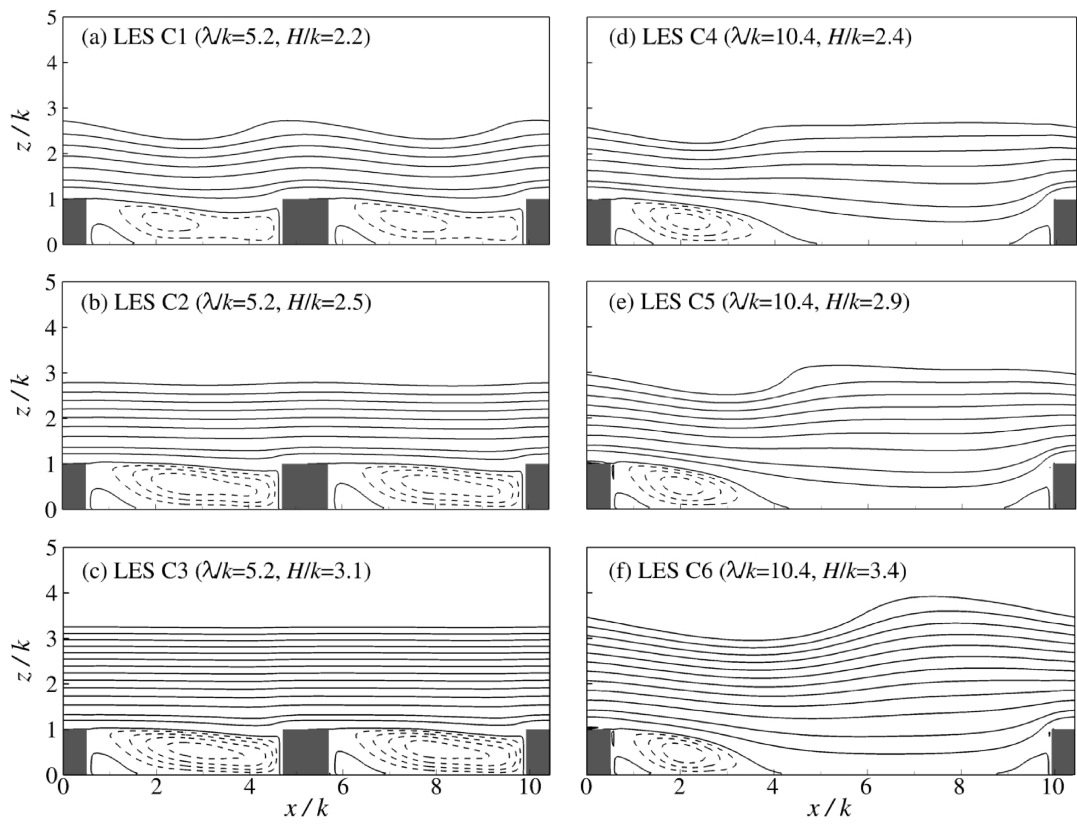


Figure 4.10: Contours of the temporal and spanwise mean streamfunction for six cases, C1-C6.

4. LEVEL SET METHOD VALIDATION CASE

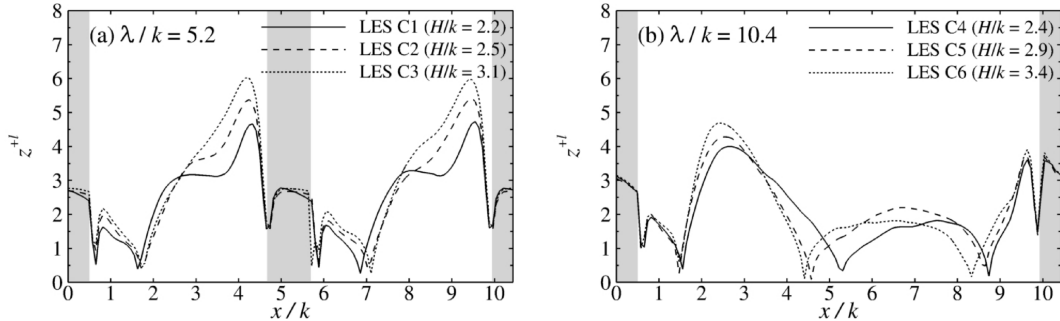


Figure 4.11: Streamwise variation of spanwise mean normalised distance from the wall to the first computational grid point. (a) $\lambda/k = 5.2$; (b) $\lambda/k = 10.4$ The grey shaded regions denote the locations of the bars.

velocities due to the presence of the recirculation in the wake. It is noteworthy that the peak values in the recirculation region are higher than those in the region $4.3 \leq x/k \leq 9.0$, which corresponds to the portion of the bed in which the flow has reattached to the wall. The minima that are visible approximately half way between the bars correspond to the position at which wall shear stress switches from negative to positive, and gives an alternative measure of the location of the reattachment point that was discussed above with reference to the streamfunction. The variation of z^+ suggests that in the lowest submergence case the flow reattaches at $x = 5.3k$ and in the highest case it reattaches at $x = 4.4k$, a decrease of approximately 17%.

4.5 Closure

Results from large eddy simulations and complementary flume experiments of turbulent open channel flows over bed-mounted square bars at intermediate submergence have been presented. In total six flow cases were investigated, comprising two roughness spacings that correspond to transitional and k-type roughness and three flow rates. The bed slope was held constant for all cases, and relative submergence therefore increased with flow rate. In the experiments the water surface was observed to be very complex and turbulent for the large spacing cases, and comprised a single hydraulic jump between the bars. The streamwise posi-

4. LEVEL SET METHOD VALIDATION CASE

tion of the jump varied between the cases, with the distance of the jump from the previous upstream bar increasing with flow rate. The free surface was observed to be less complex in the small spacing cases, particularly for the two higher flow rates, in which the flow resembled a classic skimming flow. The DarcyWeisbach friction factor was calculated for all six cases from a simple momentum balance, and it has been shown that for a given flow rate the larger bar spacing produces higher resistance.

The predictions of the LES have been shown to be in reasonably good agreement with the experiments in terms of mean free surface position and mean streamwise velocity. The position of the hydraulic jumps have been well represented. Contours of spanwise and temporal mean streamlines revealed that the small spacing cases are characterized by classic cavity flow with a quasi-rough wall presented at the height of the roughness crests. In the large spacing cases the length of the mean recirculation bubble was observed to decrease with relative submergence.

Based on the results of this chapter, the level set method as an interface capturing tool has been proven to be an accurate and reliable method in predicting the free surface of an open channel. The following chapters adopt the same method for a wider range of applications.

4. LEVEL SET METHOD VALIDATION CASE

Chapter 5

The Effect of Bridge Abutment Length on the Turbulence Structure and the Flow Through the Opening¹

5.1 Motivation and Objectives

This study attempts to contribute to the design of resilient hydraulic structures by elucidating the complex flow mechanisms around bridge abutments in changing conditions. Large eddy simulations of the turbulent flow around bridge abutments of different lengths are performed, using LSM to predict the free surface deformation. The relatively high constriction to which the flow is subjected may produce fairly high local Froude numbers that prevent the rigid lid assumption. To achieve a faithful representation of a natural river, the computational domain consists of an asymmetrical compound geometry with a parabolic main channel in which two variable-length abutments with sloped sidewalls and rounded cor-

¹Results from this chapter are directly adopted from the 3rd journal paper listed in the section of related publications.

5. THE EFFECT OF BRIDGE ABUTMENT LENGTH ON THE TURBULENCE STRUCTURE AND THE FLOW THROUGH THE OPENING

ners are placed. The challenge of the present study from a numerical point of view relies on the concurrence of several factors: a) a numerical setup that solves the larger scales of turbulence; b) fluid-structure interaction, including important flow contraction; c) free-surface prediction; d) complex and realistic (compound and asymmetric) channel. To the author's knowledge, such analysis has rarely been carried out in the past, less so with these factors combined. The present paper proceeds firstly to validate the large-eddy simulation with complementary experimental data. It then discusses the differences on the mean flow patterns between the two abutment configurations, focusing on the effect of increasing contraction on the extent of the recirculation vortices and the oscillation of the shear layer between this recirculation and the main channel flow. Thirdly, the results focus on the analysis of the coherent structures shed by the abutments, whose shapes, vorticity and periodicity are analysed by means of the Q-criterion and spectral analysis. The resulting data may contribute to the assessment of reduced-order models and the unveiling of relevant flow mechanisms.

5.2 Numerical and Experimental Setup

The computational setup shown in Fig. 5.1 replicates closely the physical experiments carried out at the Georgia Institute of Technology, US, similar to those presented in [Hong et al. \[2015\]](#). The physical model consists of a 24.4 m long steel flume of 4.26 m width and 0.76 m depth. It is an idealised hydraulic model of the Towaliga River bridge at Macon, Georgia which consists of flat horizontal floodplains on both sides of a main channel. Two spill-through abutments of depth 0.084 m, 2:1 slope and 0.636 m width with varying lengths are analysed in the large-eddy simulations. The shorter abutment (right floodplain in the downstream view) is the same length for both cases which extends to the edge of the main channel. At the left (downstream view) floodplain, two different abutment lengths, $0.41B_f$ and $0.77B_f$, are chosen - Long Setback (LSB) and Short Setback (SSB) cases respectively, where $B_f = 2.59m$ is the width of the left floodplain. The main channel is 0.96 m wide and extends streamwise along the whole length of the domain; it exhibits a parabolic cross-section with a maximum depth of 0.13

5. THE EFFECT OF BRIDGE ABUTMENT LENGTH ON THE TURBULENCE STRUCTURE AND THE FLOW THROUGH THE OPENING

m. The bridge deck (0.292 m wide and 0.033 m tall) sits on top of the abutments and spans the full width of the channel. The numerical model duplicates the geometries of the physical model except for a shorter streamwise length, which was compensated by the use of a fully-developed flow inlet condition - explained in the paragraphs to follow. The length of the computational domain is 15 m and 21 m in LSB and SSB respectively. These domain lengths are chosen by running multiple attempts to make sure all large-scale recirculation and turbulence after the abutments are captured and do not interfere with the outflow condition.

In the experiment carried out by [Hong et al. \[2015\]](#), a 16-MHz MicroADV (acoustic Doppler velocimeter) was utilized to measure instantaneous point velocities and turbulence quantities with three different types of probes: three-dimensional (3D) down-looking, 3D side-looking, and two-dimensional (2D) side-looking ([Hong et al. \[2015\]](#)). The accuracy of the ADV was evaluated by [Voulgaris and Trowbridge \[1998\]](#) in flume experiments. Typical correlation values in these experiments were greater than 90%, and the signal-to-noise ratio was greater than 15. In these experiments, the required duration of the time record at each velocity measuring point was determined to be a minimum of 2 min and as much as 5 min near the bed, and the sampling frequency was selected to be 25 Hz. The experimental conditions followed in the laboratory are carefully replicated in the numerical simulations. The water discharge for LSB and SSB cases is set to $0.085\text{m}^3/\text{s}$ and $0.108\text{m}^3/\text{s}$ respectively. The water depth was controlled by a tailgate during the experiments to ensure a water depth of 20 cm at the deepest part of the main channel under the bridge, and this condition was ensured in the simulations. The floodplain flow depth for both cases are approximately 7cm. In such conditions, labelled as 'free flow scenario', the water surface is not perturbed by the bridge at any point. The resulting bulk velocities are $U_b = 0.24\text{m}/\text{s}$ and $0.29\text{m}/\text{s}$; the Reynolds numbers, based on the bulk velocity and four times the hydraulic radius [Kara et al. \[2012\]](#), are $Re = 76, 300$ and $96, 500$; finally, the global Froude numbers, based on U_b and the average water depth D , are $Fr = 0.27$ and 0.32 for LSB and SSB cases respectively; local values based on local depths and velocities can be much higher.

Fully developed turbulent inflow conditions are prescribed at the upstream boundary of the domain. This is achieved by running precursor simulations in the

5. THE EFFECT OF BRIDGE ABUTMENT LENGTH ON THE TURBULENCE STRUCTURE AND THE FLOW THROUGH THE OPENING

absence of abutments and employing periodic open boundaries. Once the flow achieved full development (based on first and second-order statistics), the 3-D instantaneous flow field at one cross-section of the periodic channel is recorded at every time step and then provided as the inflow of the LSB and SSB simulations. The precursor inflow velocity planes are recycled every 10,000 time steps, ensuring a continuous fully-developed turbulent inflow for the duration of the simulation. This procedure has the disadvantage of introducing periodicity in the turbulence field, which was judged not particularly relevant due to the fact that the area of interest is located at the contraction and downstream, where the interaction with the abutments substantially alters the flow. Convective boundary conditions are adopted at the outlet plane. No-slip boundary conditions are employed on the side walls and channel bed while the level set method is applied to track the position of the free surface. The initial free surface height, h is estimated based on the experimental measurements and is assumed flat at the start of the simulation. The abutments, bridge, and the parabolic channel boundaries are represented by a Lagrangian field of immersed boundaries.

Both a 'coarse' and a 'fine' uniform numerical grids are generated for both scenarios. The coarser resolution for the LSB case comprises 1500x426x80 grid points in the streamwise, spanwise and vertical directions, respectively, whereas the finer mesh doubles the resolution in all directions resulting in 3000x852x160 grid points. The total number of grid points for the LSB cases are 51M and 409M for coarse and fine resolutions, respectively. The SSB has the same grid resolution as the LSB in both coarse and fine cases but requires a longer domain in the streamwise direction, resulting in 72M and 576M grid points, respectively.

5.3 Results and Discussion

5.3.1 Validation

Profiles of computed and measured time-averaged streamwise velocity at the locations described in Fig. 5.2 are plotted in Figs. 5.3 and 5.4 for LSB and SSB cases, respectively. The experimental velocities were measured with microADV probes;

5. THE EFFECT OF BRIDGE ABUTMENT LENGTH ON THE TURBULENCE STRUCTURE AND THE FLOW THROUGH THE OPENING

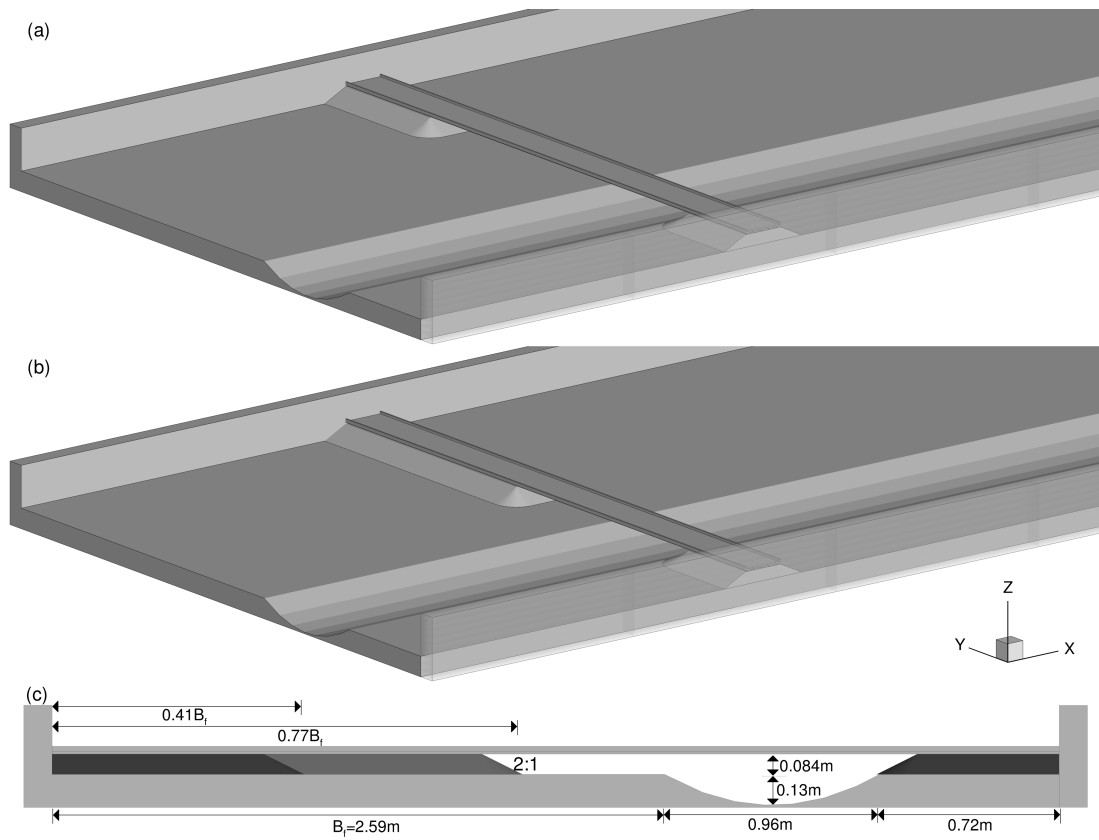


Figure 5.1: Computational domains: (a) Long-setback abutment case, LSB, (b) Short-setback abutment case, SSB, (c) Cross-section including its dimensions.

5. THE EFFECT OF BRIDGE ABUTMENT LENGTH ON THE TURBULENCE STRUCTURE AND THE FLOW THROUGH THE OPENING

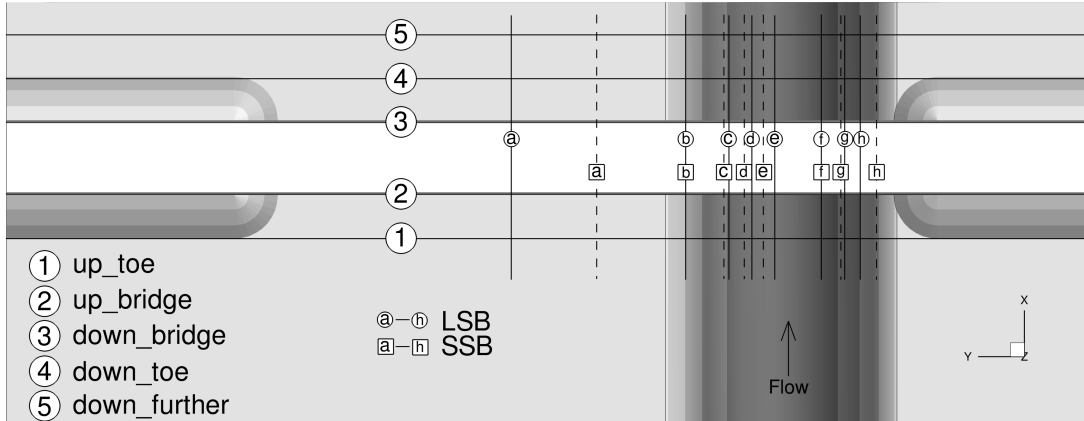


Figure 5.2: Definition sketch of the abutments and bridge area. The intersections between horizontal numbered lines (1-5) and vertical solid (LSB) and dashed (SSB) lines indicate the locations at which time-averaged streamwise velocity profiles (a)-(h) were measured experimentally.

a detailed description of the ADV setup can be found in [Hong \[2012\]](#). The validation points are located at five cross-sections: `Up_toe(1)` and `down_toe(4)` at the upstream and downstream toes of the abutments respectively; `Up_bridge(2)` and `down_bridge(3)` at the upstream and downstream faces of the bridge respectively; and `down_further(5)`, located 0.15 m downstream of `down_toe`. The intersections between the aforementioned cross-sections (1)-(5) and the solid (for LSB) and dashed (for SSB) lines from Fig. 5.2 provide the locations at which the time-averaged velocity profiles (a)-(h) exhibited in Figs. 5.3 and 5.4 are extracted. In Figs. 5.3 and 5.4, dashed horizontal lines show the approximate water surface elevation at the corresponding location while solid horizontal lines represent the channel bed. The vertical coordinate z is scaled with the initial water depth h at the deepest point ($h = 0.2039$ m for LSB and $h = 0.2068$ m for SSB). Circles, dashed line and solid line represent the experimental data, the coarse-mesh LES and the fine-mesh LES results, respectively. For brevity only the validation profiles at cross-sections 2, 3, and 4 are shown, the other two cross-sections are very similar in terms of the match between experimental and numerical data.

The overall agreement between the experimental data and the LES results for the LSB case is remarkably good. The predicted velocities match the measured ones quite well, except at the 3-4 (h) profiles, which are located in the

5. THE EFFECT OF BRIDGE ABUTMENT LENGTH ON THE TURBULENCE STRUCTURE AND THE FLOW THROUGH THE OPENING

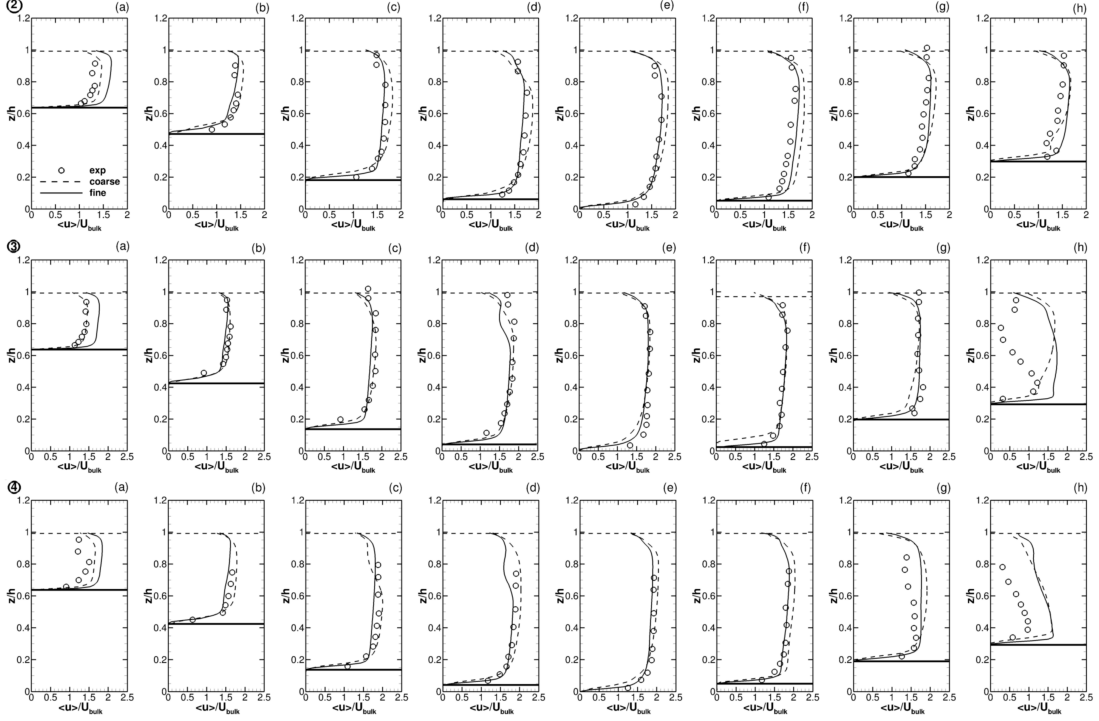


Figure 5.3: Computed and measured time-averaged streamwise velocity profiles at locations (a)-(h) (as described in Fig. 5.2) in cross-sections 2-4 of the LSB case. Experimental data (circles), coarser-mesh LES (dashed line), and finer-mesh LES (solid line).

vicinity of the right abutment, where the simulations overestimate the streamwise velocity by approximately 50%. This is probably due to slight differences in the right abutment's geometry or slight location differences between experiments and simulations. The numerical results obtained with the finer mesh (solid line) generally match better the experimental measurements in all profiles except (a), where they tend to overestimate the velocities obtained in the laboratory. The fine-mesh LES performs very well in predicting the near-bed streamwise velocity due to its higher resolution near the bed.

Fig. 5.4 allows quantitative comparisons of the simulated time-averaged streamwise velocity profiles with the experimental data for the SSB case. The agreement between the coarse and fine simulations is again convincing particularly in the main channel. Both grids seem to capture well the details of the flow when subjected to a significant contraction. As with the LSB setup, the velocities

5. THE EFFECT OF BRIDGE ABUTMENT LENGTH ON THE TURBULENCE STRUCTURE AND THE FLOW THROUGH THE OPENING

at some of the (h) profiles are overestimated by the LES in the vicinity of the right abutment. There are no significant differences between the results for two mesh resolutions for the most part, with the finer mesh slightly more accurate in the near-bed region, whereas the coarser LES arguably shows somewhat better agreement at the upper half of some profiles at cross-sections 2 and 3. Profiles 3-4 (a) show significant discrepancies between both grid resolutions, probably related to the fact that this location is under the influence of the shear layer produced by the left abutment, and slight changes in its prediction have a great effect on the local velocities. It also appears that the LES has achieved a reasonable grid convergence (the results of both meshes do not offer significant differences). The succeeding plots in this chapter are based on the data set obtained from the fine-mesh simulations.

Figs. 5.5 and 5.6 present LES-computed water surface elevations together with experimental measurement data at 15 locations along cross-sections 2, 3 and 4. The numerical data points are the level set $\phi = 0$, which represents the relatively sharp boundary between the two fluids (water and air). Overall, both LSB and SSB simulations provide a reasonable prediction of the water surface elevation. The free surface is close to horizontal with a very gradual slope towards the right abutment in the LSB case. The acceleration due to significant flow contraction of the SSB case results in a water surface deformation, in the form of a depression near the abutments. The depression is slightly more significant in the LES profile than in the experimental point gauge measurements.

5.3.2 Flow Separation

The instantaneous (a) and time-averaged (b) streamwise velocity contours for LSB and SSB in a horizontal plane located 15 cm above the deepest point (2 cm above the floodplain bed) are presented in Figs. 5.7 and 5.8. The dashed lines represent the zero streamwise velocity, hence highlighting the flow separation and recirculation downstream of the abutments. Several relevant flow phenomena can be observed in these plots. Firstly, the effect of contraction: the flow accelerates towards the abutments due to continuity, reaching at the contraction $2U_b$ in the LSB case and $2.5U_b$ in the SSB case. Secondly, the abutment induces flow

5. THE EFFECT OF BRIDGE ABUTMENT LENGTH ON THE TURBULENCE STRUCTURE AND THE FLOW THROUGH THE OPENING

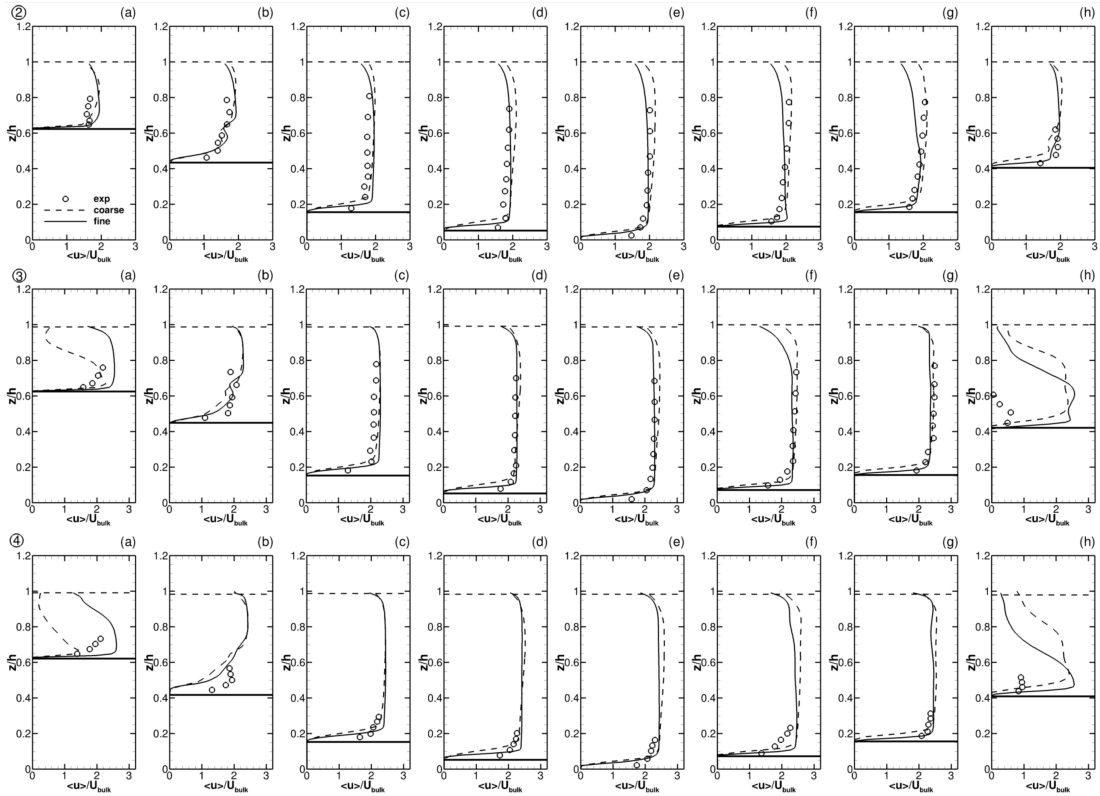


Figure 5.4: Computed and measured time-averaged streamwise velocity profiles at locations [a]-[h] (as described in Fig. 5.2) in cross-sections 2-4 of the SSB case. Experimental data (circles), coarser-mesh LES (dashed line), and finer-mesh LES (solid line).

5. THE EFFECT OF BRIDGE ABUTMENT LENGTH ON THE TURBULENCE STRUCTURE AND THE FLOW THROUGH THE OPENING

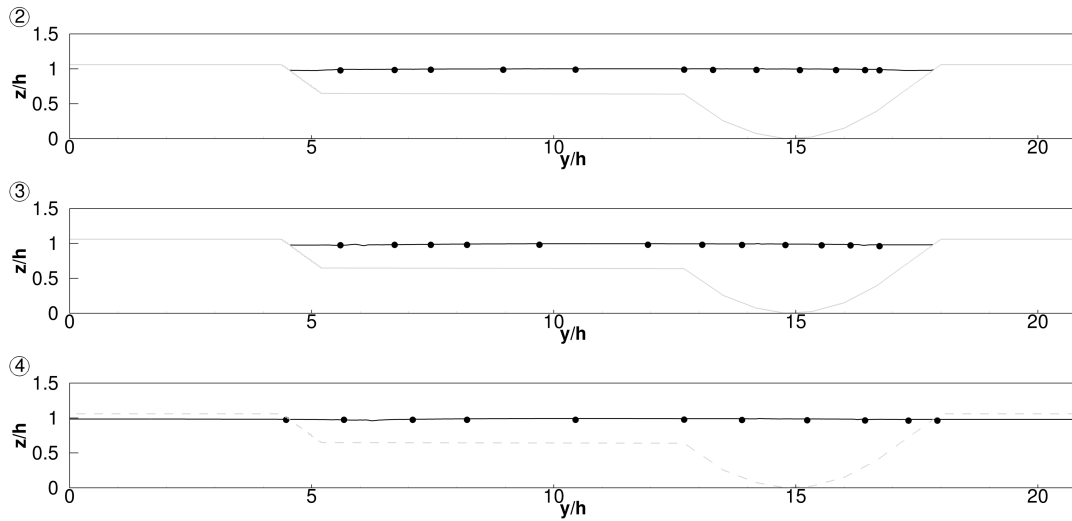


Figure 5.5: Computed (solid line) and measured (circles) profiles of the water surface for the LSB case at cross-section 2-4.

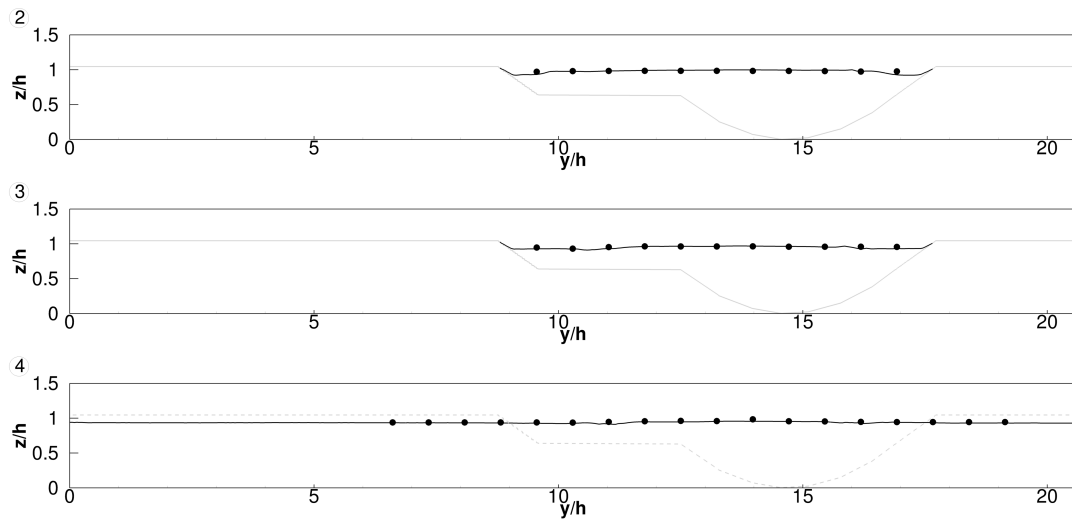


Figure 5.6: Computed (solid line) and measured (circles) profiles of the water surface for the SSB case at cross-section 2-4.

5. THE EFFECT OF BRIDGE ABUTMENT LENGTH ON THE TURBULENCE STRUCTURE AND THE FLOW THROUGH THE OPENING

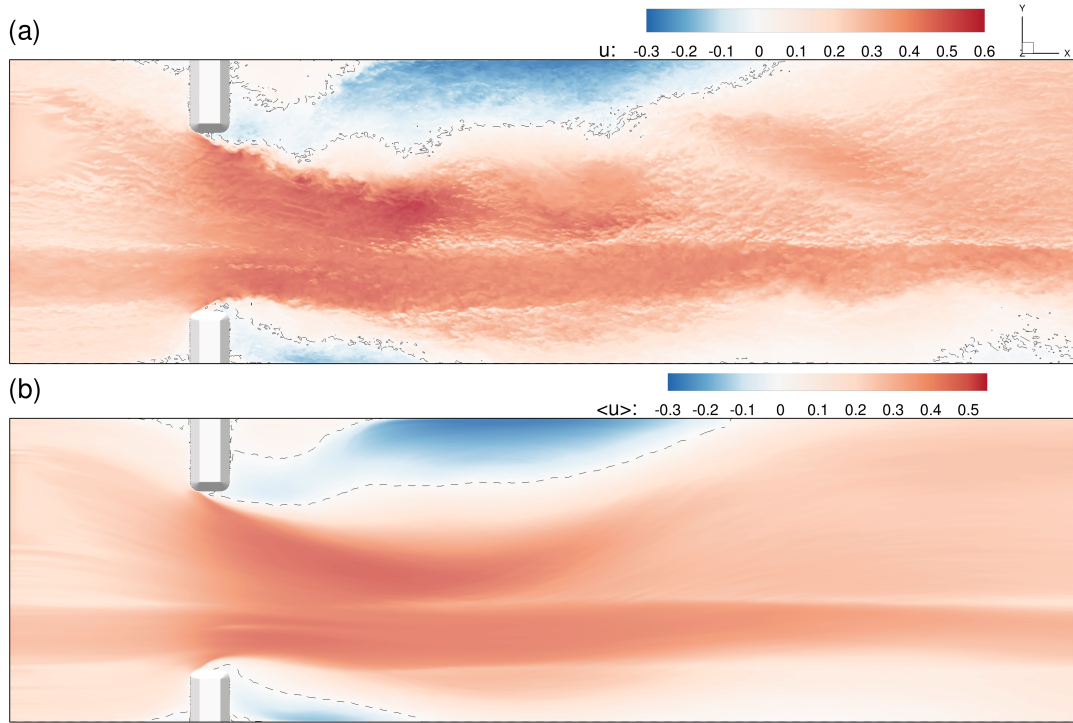


Figure 5.7: LES-predicted streamwise velocity contours in a selected horizontal plane: (a) instantaneous (b) time-averaged velocity for the LSB case.

separation and a significant recirculation bubble downstream of the abutments forms; the recirculation extends $x/b=1.82$ for LSB and $x/b=2.39$ for SSB (see Fig. 5.9 for details) cases, respectively. Thirdly, the velocity contours reflect rather clearly the banks of the main channel in the form of a velocity drop (white line), indicating the impact of the secondary motion at the channel-floodplain interface on the streamwise velocity. Regarding the differences between the time-averaged and instantaneous streamwise velocity fields, Figs. 5.7 and 5.8 rather nicely illustrate the distinctive scale of the medium-scale instantaneous eddies versus the large-scale structures of the mean flow. The meandering motion induced by the contraction on the flow in the main channel is particularly remarkable in the SSB case. Fig. 5.8a) suggests that these oscillations at the main channel interface produce periodical ejections towards the floodplains, particularly the left one.

2D (left) and 3D (right) streamlines are presented in Fig. 5.9 for LSB (top) and SSB (bottom) cases. The two-dimensional flow field is extracted at a plane

5. THE EFFECT OF BRIDGE ABUTMENT LENGTH ON THE TURBULENCE STRUCTURE AND THE FLOW THROUGH THE OPENING

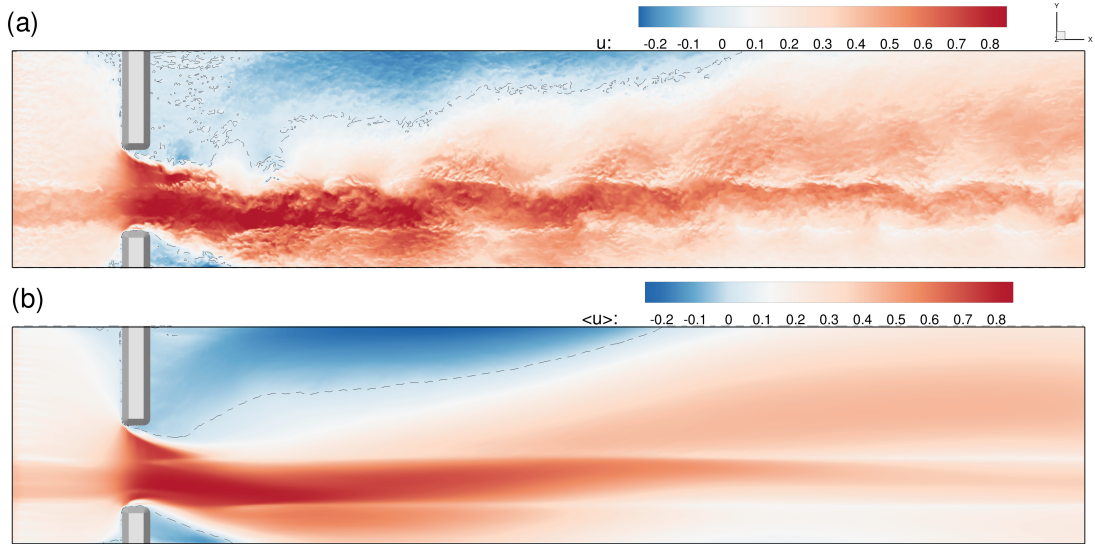


Figure 5.8: LES-predicted streamwise velocity contours in a selected horizontal plane: (a) instantaneous (b) time-averaged velocity for the SSB case.

15 cm above the deepest point of the main channel; the 3D streamlines are colour-coded by the time-averaged streamwise velocity $\langle u \rangle$. The flow separation is visualised and quantified and several recirculation zones occur. The first one is located upstream of the abutments a result of the blockage they exert on the oncoming flow. Small corner vortices are formed at the junction between the upstream toe and the side walls, which are similar in size for both setups. The flow past the abutments is dominated by large recirculation cells featuring counter-clockwise rotating vortices in both cases. The left abutment's recirculation of the SSB case extends much further downstream and reaches $x/b = 2.39$ before the flow reattaches to the side wall, whereas for LSB (shorter left abutment) the flow reattaches at approx. $x/b = 1.82$. Comparing both cases, the ratio between the lengths of the recirculation bubbles $\frac{X_{SSB}}{X_{LSB}} = 1.3$ is significantly smaller than the ratio between the left abutments' lengths $\frac{0.77B_f}{0.41B_f} = 1.9$, but rather similar to the ratio between the maximum velocities $\frac{U_{SSB}}{U_{LSB}} = 1.25$. These counter-clockwise eddies are complemented by corner vortices (labeled CV1 and CV2) at the downstream junction of the left abutment which rotate in the clockwise direction. Interestingly, while CV1 covers the whole length of the abutment, CV2 is more constrained towards the side wall, which may be explained by the dominance of

5. THE EFFECT OF BRIDGE ABUTMENT LENGTH ON THE TURBULENCE STRUCTURE AND THE FLOW THROUGH THE OPENING

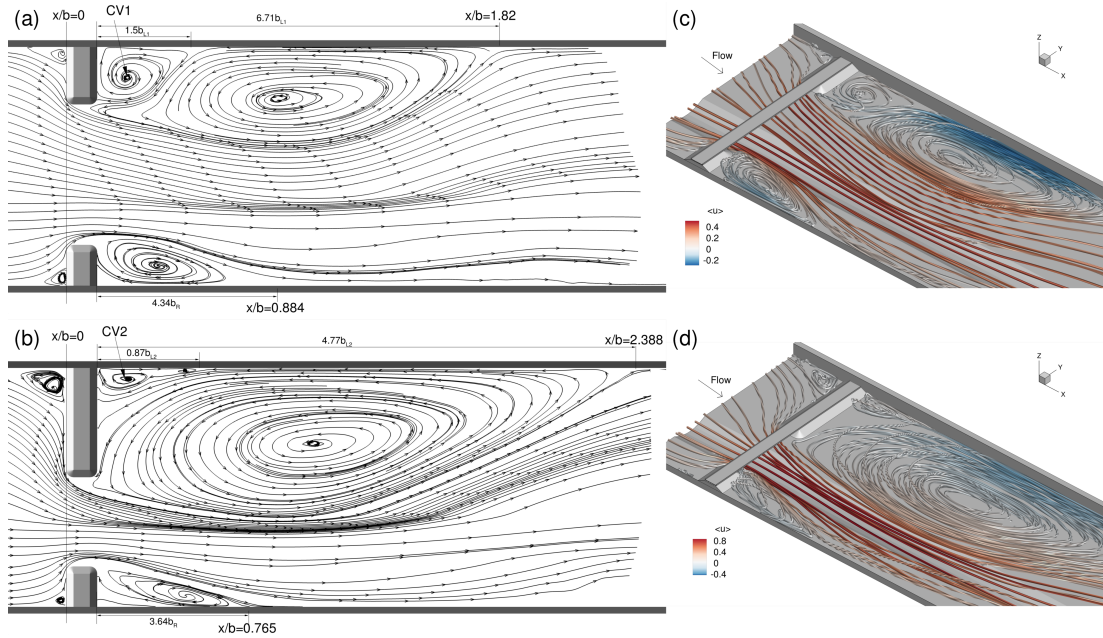


Figure 5.9: 2D streamlines near the abutment for (a) the LSB case and (b) the SSB case, 3D streamtraces colour-coded with time-averaged streamwise velocity for (c) the LSB case and (d) the SSB case.

the main recirculation cell. The larger contraction ratio of the SSB case causes the flow to veer more substantially towards the right side of the main channel; the streamlines are diverted almost immediately after the bridge opening onto the right floodplain and flow reattachment takes place at $x/b = 0.765$. For the LSB case, the main channel is not deflected towards the right bank and hence the reattachment does not occur until $x/b = 0.884$, allowing a slightly larger and more defined recirculation eddy behind the right abutment in comparison with the rather short compressed recirculation zone of the LSB case. Figs. 5.9c and 5.9d highlight again the difference in extent of recirculation between cases and also visualise the significant flow acceleration that takes place through the opening and high velocities are sustained until the end of the respective recirculation zones. The similarities of the vortical structures' shapes and sizes between the 2D and 3D figures demonstrate that the flow is predominantly two-dimensional in the shallow floodplains.

5. THE EFFECT OF BRIDGE ABUTMENT LENGTH ON THE TURBULENCE STRUCTURE AND THE FLOW THROUGH THE OPENING

5.3.3 Instantaneous Secondary Flow

The previous section discussed the main features of the time-averaged flow separation and recirculation bubbles behind the abutments. However, in the context of a turbulent flow, the shape and size of these coherent structures is subjected to the interaction with transitory structures which provoke oscillations and meandering (see Fig. 5.8a), resulting in increased turbulence. Of particular interest is the region behind the abutments which is where three turbulence structures interact: a) the shear layer between the recirculation zones and the main flow, b) the vortices shed from the abutments' tip, c) the transition between the main channel and the floodplain.

Fig. 5.10 presents isosurfaces of the Q-criterion together with vorticity contours in selected cross-sections. The Q-criterion (e.g. [Dubief and Delcayre \[2000\]](#)) is defined as:

$$Q = \frac{1}{2}(|\Omega| - |S|) \quad (5.1)$$

in which $|\Omega|$ and $|S|$ are the rotation and strain rates, respectively:

$$|\Omega| = \sum_{i,j=1}^3 \left[\frac{1}{2} \left(\frac{\partial u_i}{\partial x_j} - \frac{\partial u_j}{\partial x_i} \right) \right]^2 \quad (5.2)$$

$$|S| = \sum_{i,j=1}^3 \left[\frac{1}{2} \left(\frac{\partial u_i}{\partial x_j} + \frac{\partial u_j}{\partial x_i} \right) \right]^2 \quad (5.3)$$

where u_i and u_j are instantaneous velocity components. Positive isosurfaces of Q isolate areas where the strength of rotation overcomes the strain, thus visualising rotation in the form of vortex tubes. The Q-criterion isosurfaces are colour-coded with the streamwise vorticity ω_x , which measures the rotation intensity around the streamwise x axis, hence on the YZ cross-sectional plane. Positive streamwise vorticity (red) corresponds to clockwise rotation while blue represents

5. THE EFFECT OF BRIDGE ABUTMENT LENGTH ON THE TURBULENCE STRUCTURE AND THE FLOW THROUGH THE OPENING

anti-clockwise motion. The Q-criterion isosurfaces are complemented with three cross-sectional slices of the ω_x field in between and downstream of the abutments to help understand the secondary motion. The vortex tubes labelled SSL are shed from the tip of the abutments and then convected downstream along the shear layer formed between the accelerated flow through the opening and the recirculating, low-momentum zones of the floodplains and downstream of the abutments. The NV label identifies 'necklace vortices', which can be found near the abutments as an offset of the SSLs towards the main channel. NVs form before approaching the abutments, more noticeably for the right abutment in both cases. NVs are better defined and exhibit a more consistent streamwise vorticity colouring than SSLs, i.e. they portray their stable rotating motion (clockwise by the left abutment and anti-clockwise by the right one). In both LSB and SSB cases, a long patch of interface vortices (IV) appear as a result of the momentum exchange between the right edge of the main channel and the floodplain; starting upstream of the right abutment as the flow is forced into the main channel. The same flow mechanism produces a very well-defined IV at the interface between the main channel and the left floodplain but only for the SSB case (Fig. 5.10b). In the LSB case (Fig. 5.10a), no IV is found on the left side of the main channel, highlighting the differences between the two contraction ratios. Interestingly, a counter-rotating vortex pair near the water surface labelled as SV can only be found in the LSB results. The SV pair consists of both short clockwise and long anti-clockwise rotating vortices side by side near the surface and off centre towards the left of the main channel. When visualising simultaneously instantaneous velocity streamlines (not shown for clarity and brevity), the SV pair forms where the surface flow coming from the left and right floodplains meet over the main channel.

Fig. 5.11 presents three-dimensional views of the water surface ($\phi = 0$ level-set isosurface) at an instant in time for the LSB and SSB cases, respectively. The vertical axis is exaggerated to highlight better the features of the water surface deformations. The coherent structures described in Fig. 5.10 have a clear signature at the free surface; regularly recurring dips in the water surface are the low-pressure core of the shear layer vortices in both cases, although the dips are more prominent in the SSB geometry due to a stronger shear layer and vortices.

5. THE EFFECT OF BRIDGE ABUTMENT LENGTH ON THE TURBULENCE STRUCTURE AND THE FLOW THROUGH THE OPENING

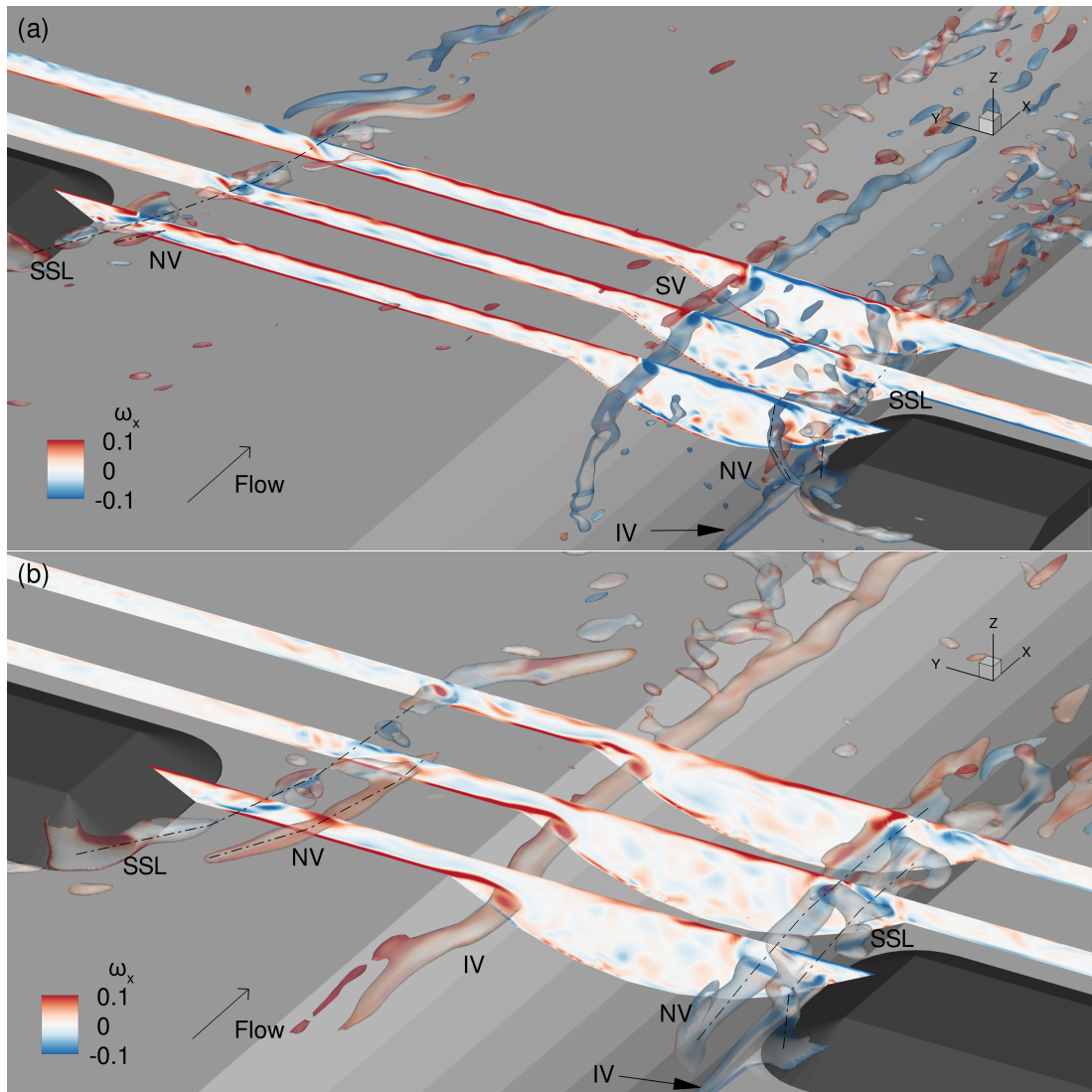


Figure 5.10: Isosurfaces of the Q-criterion together with contours of the stream-wise vorticity in selected cross-sections: (a) LSB case, (b) SSB case.

5. THE EFFECT OF BRIDGE ABUTMENT LENGTH ON THE TURBULENCE STRUCTURE AND THE FLOW THROUGH THE OPENING

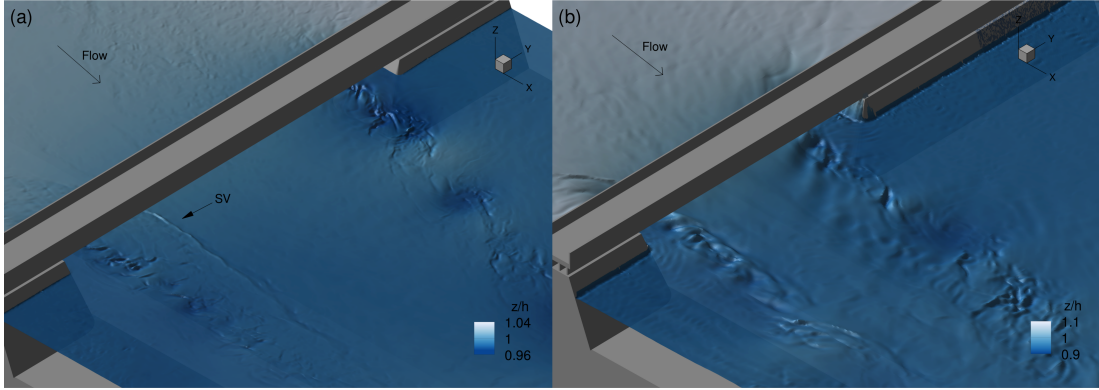


Figure 5.11: Water surface deformation represented by zero level set and colour-coded by water depth for (a) LSB case and (b) SSB case.

The effect of the SV on the free surface of the LSB setup is very noticeable and it appears in Fig. 5.11a) as a persistent bulging line.

5.3.4 Shear Layer Oscillation and Vortex Shedding

With the aim of quantifying the oscillations and the vorticity generated in the shear layer behind the abutments for different contraction ratios, several time-series of velocity are recorded at selected sampling points for both LSB and SSB cases over a long period of simulation time (150 seconds approx.) and at a frequency of 500Hz. The time-series obtained are analysed using: probability density function, quadrant analysis and power density spectra, and the data are related to the physics of the instantaneous flow.

Fig. 5.12a depicts the locations where velocity time signals are recorded for the LSB case with L and R being the label for those points in the vicinity of the left or right abutment, respectively. The probability density function (PDF) of the turbulent fluctuation of the streamwise velocity u' , normalised by its root-mean-square value u'_{RMS} is calculated at each sampling point and plotted together with the Gaussian distribution (solid line). Fig. 5.12b plots the pdfs for the LSB's left abutment and as can be seen almost all the pdfs exhibit a skewness towards the positive except for the pdf at L1 which follows the Gaussian distribution fairly well. L1 is located in the vicinity of the tip of the abutment, where the separation begins. From L2 onwards, the pdfs show a clear deviation of the mean u'/u'_{RMS}

5. THE EFFECT OF BRIDGE ABUTMENT LENGTH ON THE TURBULENCE STRUCTURE AND THE FLOW THROUGH THE OPENING

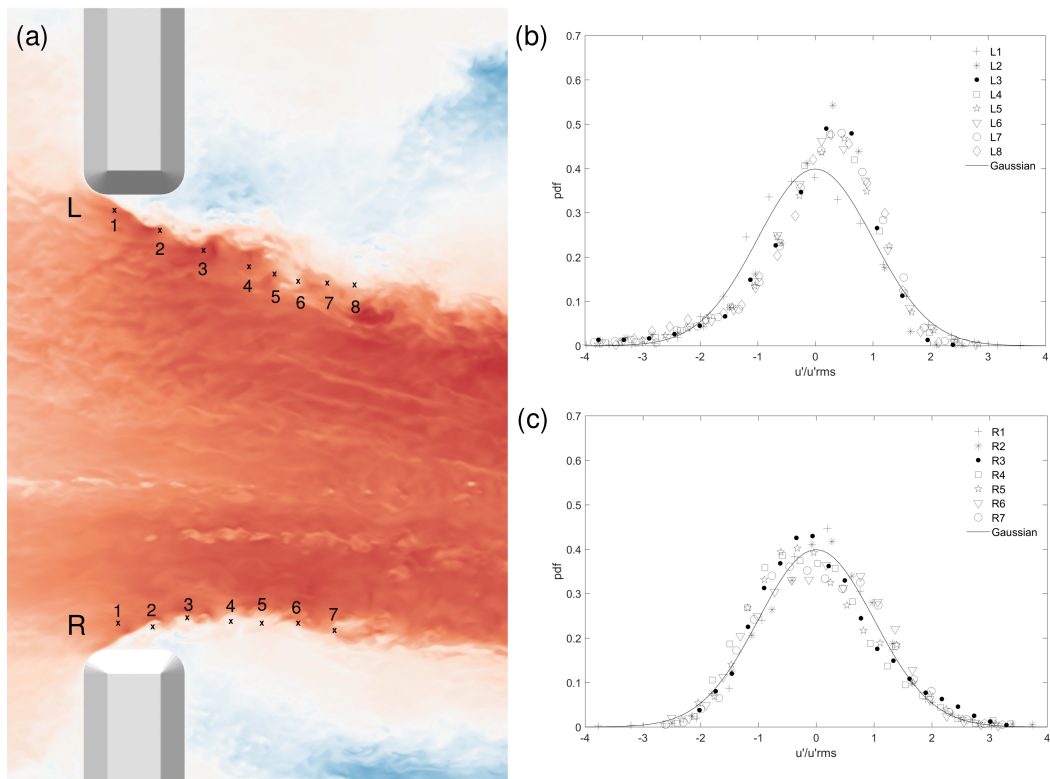


Figure 5.12: LSB case: (a) Locations along the estimated separated shear layer where velocity time signals are recorded. (b) Probability density function of streamwise velocity fluctuation normalised by the root-mean-square of the streamwise velocity fluctuation near the left abutment at all locations and (c) Probability density function of streamwise velocity fluctuation at all location in the vicinity of the right abutment. All sampling data are taken at approximately mid depth of the floodplain.

5. THE EFFECT OF BRIDGE ABUTMENT LENGTH ON THE TURBULENCE STRUCTURE AND THE FLOW THROUGH THE OPENING

from Gaussian towards the positive side, centred around $u'/u'_{RMS} = 0.4$ approx. The amplitude of the u' fluctuations is also skewed, ranging from $u'/u'_{RMS} = -4$ on the negative side of the axis to less than $u'/u'_{RMS} = 3$ on the positive values. This suggests that the flow at these locations feature many acceleration slightly stronger (than the average) accelerations due to the bridge contraction (hence the positive u'/u'_{RMS} mean from L2 onwards) combined with more significant low frequency events in which the recirculation bubble expands into the shear layer along which points L2-L8 are located (hence the long negative tail of the PDFs). The seven R points located in the shear layer of the right abutment (Fig. 5.12c) follow quite closely the normal distribution, although with a very slight bias towards the negative side and a very slight tailing towards the positive side. This indicates a lower occurrence of high-momentum ejections from the right abutment's tip and a more balanced equilibrium between the recirculation and the main channel flow overall. The different turbulence characteristics in terms of streamwise velocity fluctuation of the flow around the two abutments is the consequence of the different abutment length (however not very significant in the LSB case) and the geometrical asymmetry of the compound channel; the left floodplain is much wider and carries more mass and momentum so that flow acceleration due to contraction is more significant in the shear layer of the left abutment than in the one of the right abutment.

Fig. 5.13 shows the locations where velocity time signals are recorded and the corresponding u'/u'_{RMS} pdfs for the SSB case. Overall, the pdfs at those points follow but amplify the trends from the LSB case, as it is expected given the greater contraction ratio. From the u'/u'_{RMS} pdfs along the left shear layer (L locations), only L2 appears to be Gaussian distributed. All other L signals exhibit a clear skewness, following the normal distribution up to $u'/u'_{RMS} = -1$, having a maximum at approx. $u'/u'_{RMS} = 0.75$ and then falling abruptly. The exception is L3, which peaks at approximately $u'/u'_{RMS} = -0.6$. L3 is situated at the point where small vortical eddies start to form shortly after the flow separates from the abutment tip. The behaviour of the points L2 and L4-L9 correlates with the frequent occurrence of ejections of high momentum flow (local accelerations) from the opening and low frequency events occur due to the expansion of the recirculation zone similar the LSB case. The meandering of the instantaneous

5. THE EFFECT OF BRIDGE ABUTMENT LENGTH ON THE TURBULENCE STRUCTURE AND THE FLOW THROUGH THE OPENING

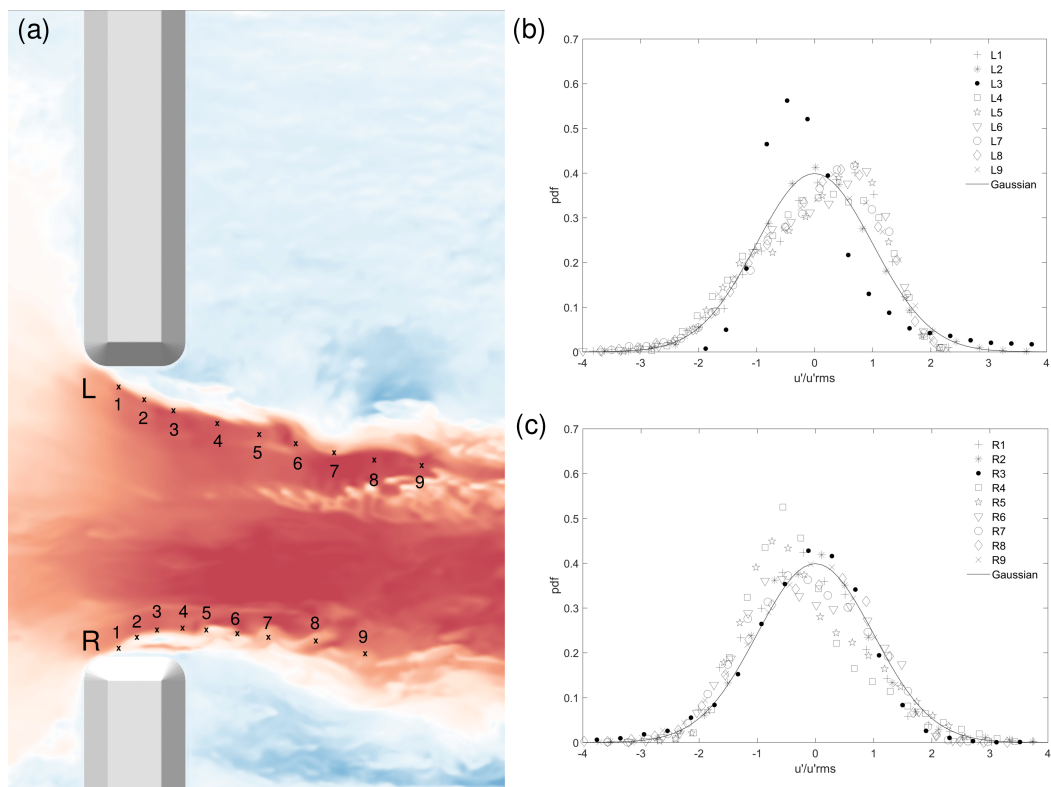


Figure 5.13: (a) SSB case: (a) Locations along the estimated separated shear layer where velocity time signals are recorded. (b) Probability density function of streamwise velocity fluctuation normalised by the root-mean-square of the streamwise velocity fluctuation near the left abutment at all locations and (c) Probability density function of streamwise velocity fluctuation at all locations in the vicinity of the right abutment. All sampling data are taken at approximately mid depth of the floodplain.

5. THE EFFECT OF BRIDGE ABUTMENT LENGTH ON THE TURBULENCE STRUCTURE AND THE FLOW THROUGH THE OPENING

velocities in the SSB setup as observed in Fig. 5.8a is the direct result of the oscillating recirculation zone. The pdfs at the locations near the right abutment (Fig. 5.13c) mostly follow the Gaussian distribution, except for R4 and R5 which are rather biased towards negative values on the u'/u'_{RMS} axis. This suggests a stronger recirculation behind the right abutment that pushes the shear layer towards the main channel when compared to the LSB results. This correlates well with the observations made from Fig. 5.9b.

The quadrant analysis of the streamwise u'/u'_{RMS} and spanwise v'/u'_{RMS} velocity fluctuations are plotted in Figs. 5.14 and 5.15 for the LSB or SSB cases, respectively. Unlike the conventional quadrant analysis [Lu and Willmarth \[1973\]](#) that investigates the sweeping and ejecting motion of the flow near the bed, here the analysis focuses on the horizontal turbulence events of the streamwise and spanwise directions in the separated shear layers. For brevity, only four points from each abutment are chosen and to be displayed and the vertical fluctuations w'/w'_{RMS} were omitted given the strong two-dimensional nature of the recirculations and the shear layers on the shallow floodplains. The location of the points is indicated in Figs. 5.12a and 5.13a, assuming positive directions for u'/u'_{RMS} and v'/u'_{RMS} east (flow towards the outlet) and north (flow towards the left side), respectively.

Fig. 5.14 shows the quadrant analysis for the LSB case. Points L3, L5, and L7 confirm the findings from Fig. 5.12b, with most points concentrated in Q1 ($u'/u'_{RMS} > 0, v'/u'_{RMS} > 0$) corresponding to fast-flow ejections from the contracted flow through the bridge opening, and fewer but higher-magnitude points recorded in Q3 ($u'/u'_{RMS} < 0, v'/u'_{RMS} < 0$), indicating lower-frequency intrusions of the recirculating flow in the shear layer. L1 exhibits a more balanced, isotropic trend, characterised by an oval shape which is characteristic of streamwise fluctuations. Points R3, R5, and R7 reproduce a more balanced oval shape dominated by Q2 and Q4 events ($u'/u'_{RMS} < 0 - v'/u'_{RMS} > 0$ and $u'/u'_{RMS} > 0 - v'/u'_{RMS} < 0$ respectively), as the relative position of floodplain and main channel switches from left to right abutment. Point R1, by the flow around abutment's tip has a slight tendency for Q2 and Q4 events but it is more isotropic than the other locations.

Fig. 5.15 shows the quadrant analysis for the SSB case. The data sampled

5. THE EFFECT OF BRIDGE ABUTMENT LENGTH ON THE TURBULENCE STRUCTURE AND THE FLOW THROUGH THE OPENING

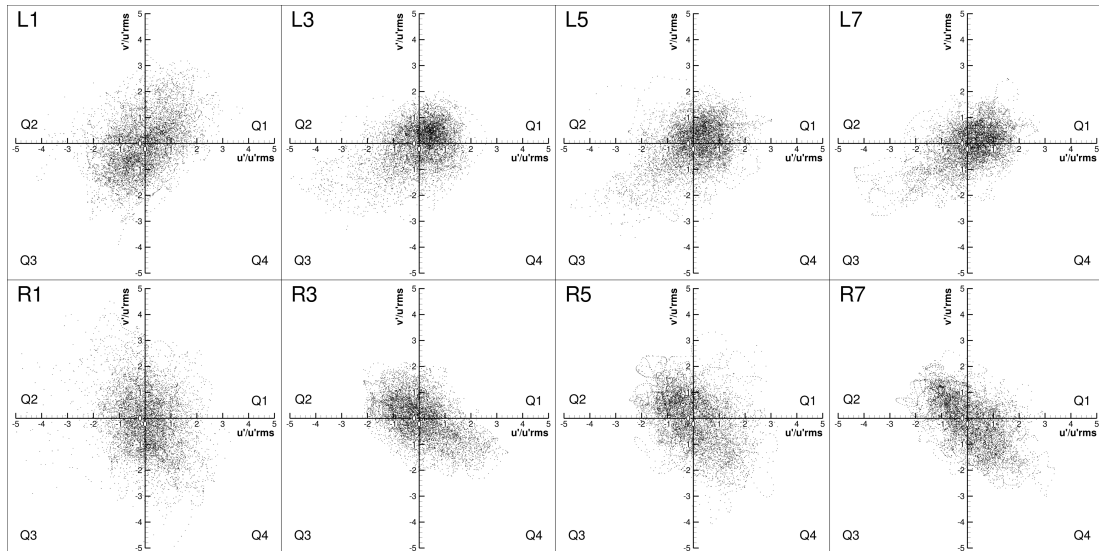


Figure 5.14: Quadrant analysis of the streamwise and spanwise velocity fluctuation normalized with u'_{RMS} for the LSB case.

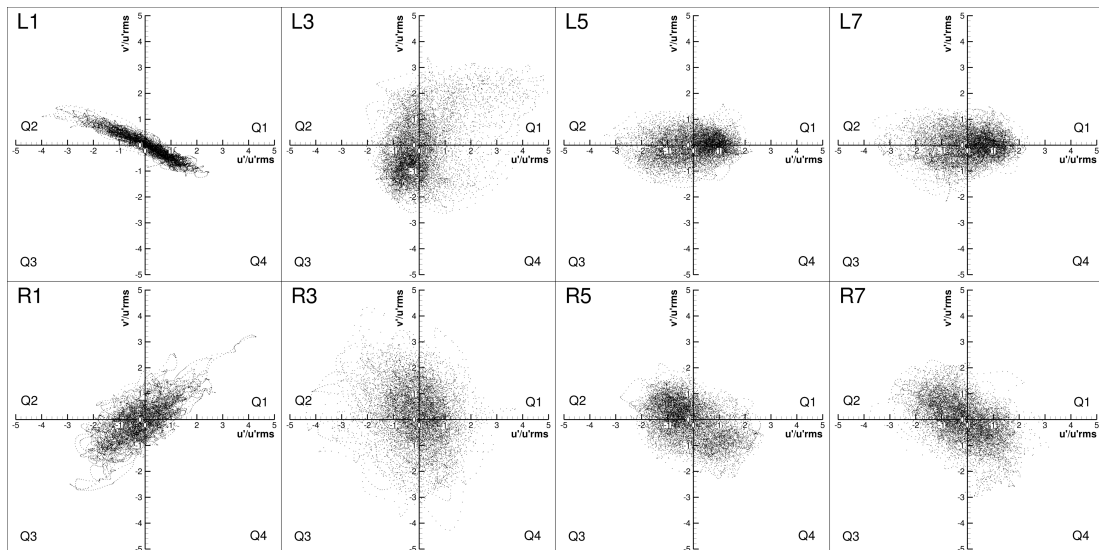


Figure 5.15: Quadrant analysis of the streamwise and spanwise velocity fluctuation normalized with u'_{RMS} for the SSB case.

5. THE EFFECT OF BRIDGE ABUTMENT LENGTH ON THE TURBULENCE STRUCTURE AND THE FLOW THROUGH THE OPENING

at the L locations (left abutment) show three different patterns. At location L1, by the abutment tip, the data points show significant linearity in the axis Q2-Q4 ($u'/u'_{RMS} < 0$ - $v'/u'_{RMS} > 0$ and $u'/u'_{RMS} > 0$ - $v'/u'_{RMS} < 0$, respectively), revealing an almost one-dimensional flow, resembling a jet, as the water from the left floodplain is forced to pass around the left abutment. At location L3 at which eddies start to form, a more balanced, isotropic behaviour of the flow is observed, with a slight majority of turbulent events in Q3 ($u'/u'_{RMS} < 0$, $v'/u'_{RMS} < 0$) and fewer and more dispersed points in Q1 ($u'/u'_{RMS} > 0$, $v'/u'_{RMS} > 0$), indicating a dominance of the recirculation bubble at this location, with periodic intrusions of high-speed flow from the contraction, in agreement with the observations from Fig. 5.13b. The data at locations L5 and L7 are similarly in their oval shape and clustered around the u'/u'_{RMS} axis. The higher contraction induces strong acceleration and hence significant one-dimensionality of the flow, albeit the shift between positive and negative values of u'/u'_{RMS} reflects the meandering of the shear layer in the left abutment's shear layer. The flow is significantly anisotropic with u' having a greater variance than v' . Near the right abutment, the flow at R1 appears similar the flow at L1 (switching the axis from Q2-Q4 to Q1-Q3 due to the opposite orientation of the abutment) but is not quite as one-dimensional than at L1. At R3 the data show a rather isotropic distribution of turbulent events, that turns into an oval shape in the axis Q2-Q4 for R5 and R7 as small eddies roll up and being less one-dimensional than their left side counterparts.

Figs. 5.16-5.18 and Fig. 5.20 offer further insights into the turbulence structure at two chosen locations (L7 and R5) near each abutment and for both cases. Each figure consists of four sub-plots, from top-left to bottom-right: (a) power spectra of both the streamwise u' and the spanwise v' turbulent fluctuations in the domain of frequency (logarithmic scale) obtained through Fast Fourier Transformation; (b) power spectra in a semilog plot to identify high-energy events; (c) wall-normal vorticity contours ω_z , with white contours represent strong anti-clockwise motion ($\omega_z < 0$) and black contours represent strong clockwise motion ($\omega_z > 0$) (contours extracted at 0.015 m below the water surface); (d) top view of the water surface ($\phi = 0$) at the same instant as in (c) to illustrate the correlation between the wall-normal vorticity and the free surface undulation. The free surface is colour-coded with water depth where dark blue depicts the depressions

5. THE EFFECT OF BRIDGE ABUTMENT LENGTH ON THE TURBULENCE STRUCTURE AND THE FLOW THROUGH THE OPENING

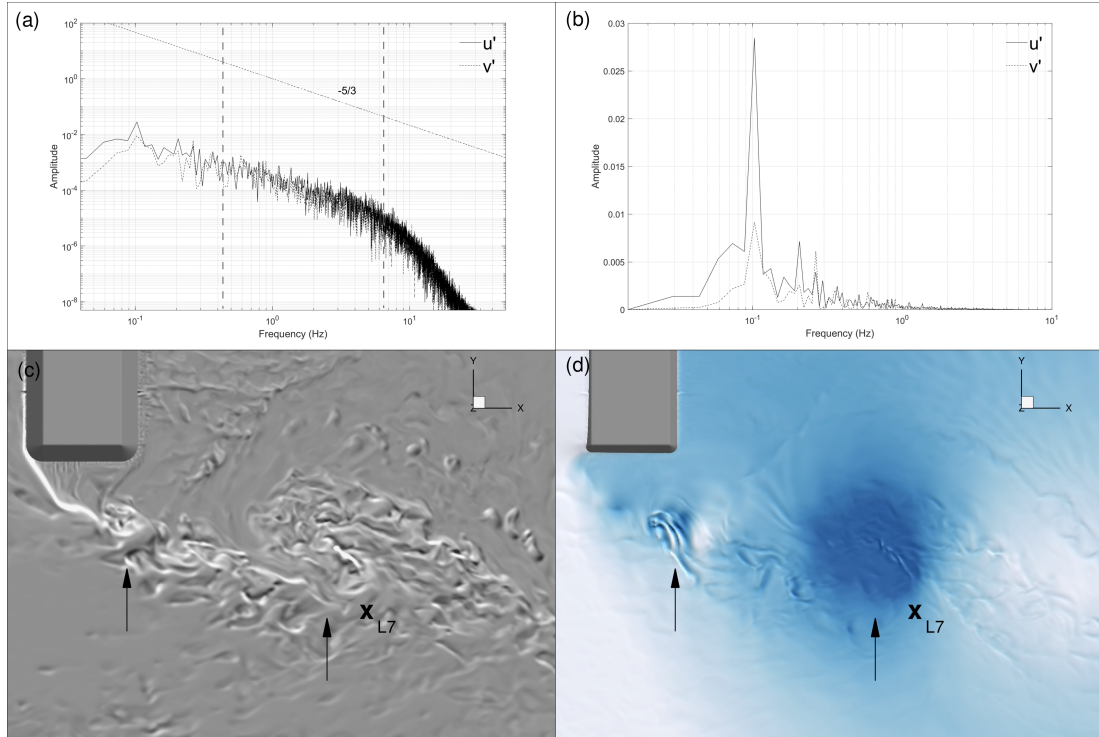


Figure 5.16: Power spectra of a streamwise and spanwise velocity fluctuation time series at location L7: (a) in log-log scale, (b) in semi-log scale, (c) wall-normal vorticity contours in a horizontal plane near the water surface and (d) water surface represented by zero level set colour-coded by the water depth for the LSB case.

in the water surface.

The power spectra from all four points (Figs. 5.16a - 5.18a and 5.20a) follow the $-5/3$ slope, indicating homogenous turbulence, before a faster decay of energy is observed at higher frequencies which is mainly induced by the SGS model. The plots demonstrate that the inertial sub-range of the energy cascade for u' and v' is well resolved that the finer mesh resolves satisfactorily the energy-containing scales of the flow. In total over two frequency decades of the flow, between the production of energetic large-scale vortices and the dissipation of the small scale turbulence are resolved by the LES of both cases.

Fig. 5.16 reveals the vortex shedding at L7, located downstream of the left abutment of the LSB setup. The power spectra of u' and v' at L7 show a very distinct peak at approximately 0.1 Hz, revealing the persistent occurrence of a

5. THE EFFECT OF BRIDGE ABUTMENT LENGTH ON THE TURBULENCE STRUCTURE AND THE FLOW THROUGH THE OPENING

turbulent event with a 10 s periodicity. This peak is particularly well depicted in Fig. 5.16b, where the logarithmic scale for the spectral amplitude of the velocity signal has been removed. This event captured in the spectral analysis is a vortex that rolls up in the shear layer downstream of the left abutment which is convected downstream. The area of high vorticity ω_z in Fig. 5.16c and the depressions in the water surface map Fig. 5.16d (indicated with arrows) visualise two of these vortices each at a different stage of their evolution. The vortex closer to the abutment (above the left arrow) has just rolled up whereas the vortex further downstream (above right arrow) has reached its maximum size and is being convected by the flow downstream. The average period of occurrence of this vortex is approximately 10 s. The vortex can also be identified from the quadrant analysis at L7 (Fig. 5.14), where the dominant high-frequency $u' > 0$ ejections are complemented with few but significant (low-frequency) $u' < 0$ events, which is the typical signature of the passing vortex.

Fig. 5.17 quantifies periodical turbulent events at R5, i.e. downstream of the right abutment of the LSB case. The u' spectrum (Figs. 5.17a-b) exhibits two high-energy peaks which correspond to approx. 10s and 6.2s periodicity (or in terms of frequency to 0.1 Hz and 0.16 Hz, respectively). The latter peak is also seen in the v' spectrum. The ω_z contours and water surface maps (Figs. 5.17c-d) reveal vortex roll-up and shedding from the tip of the abutment, albeit more irregular than around the left abutment. The vortex generation and roll-up are highlighted with arrows in Figs. 5.17c-d. Unlike the left abutment, there appears to be a bi-modality in the vortex formation, also just noticeable in the equivalent pdf (5.12c). This bi-modal behavior is probably due the interaction of the vortex with the secondary flow near the main channel-floodplain interface, dominated by the SSL, IV and NV vortices described in Fig. 5.10.

Fig. 5.18 reveals large-scale turbulence at L7, downstream of the left abutment of the SSB case. The u' energy spectra (Figs. 5.18a-b) exhibit a very prominent low-frequency peak at 0.1 Hz (10 s period). However, the vortices (Figs. 5.18c) do not appear to roll-up into distinct eddies such as those seen behind the LSB abutment, but rather are stretched due to the strong acceleration and stay within a narrow band along the shear layer. The water surface elevation plot (Fig. 5.18d) does not depict significant depressions suggesting the absence of a well-defined

5. THE EFFECT OF BRIDGE ABUTMENT LENGTH ON THE TURBULENCE STRUCTURE AND THE FLOW THROUGH THE OPENING

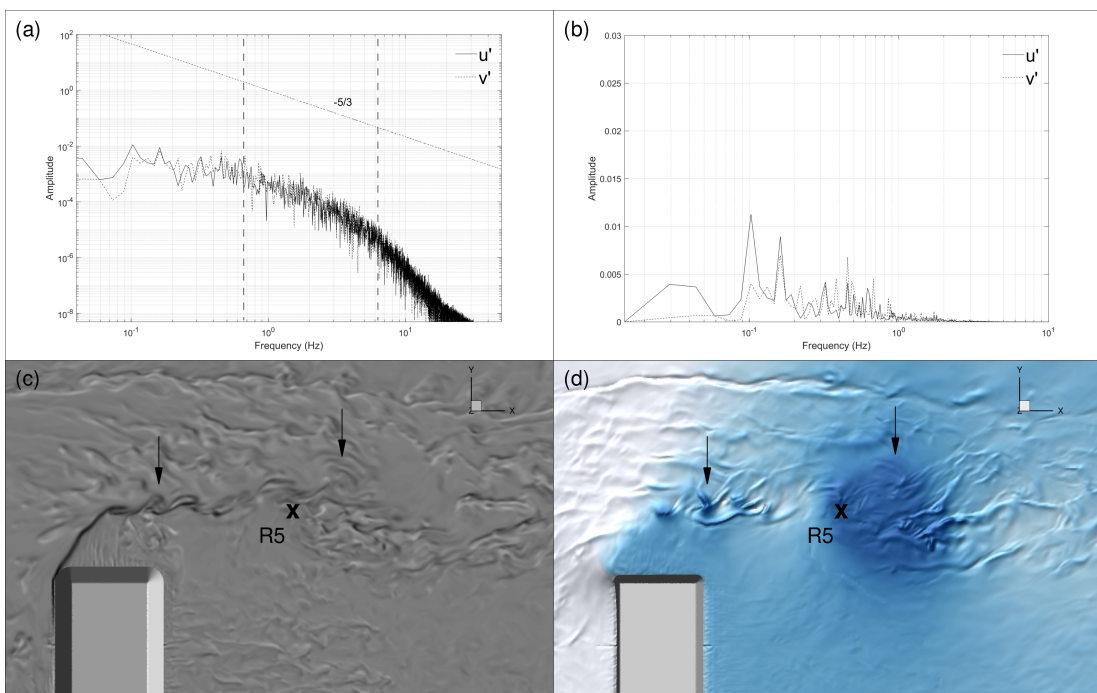


Figure 5.17: Power spectra of a streamwise and spanwise velocity fluctuation time series at location R5: (a) in log-log scale, (b) in semi-log scale, (c) wall-normal vorticity contours in a horizontal plane near the water surface and (d) water surface represented by zero level set colour-coded by the water depth for the LSB case.

5. THE EFFECT OF BRIDGE ABUTMENT LENGTH ON THE TURBULENCE STRUCTURE AND THE FLOW THROUGH THE OPENING

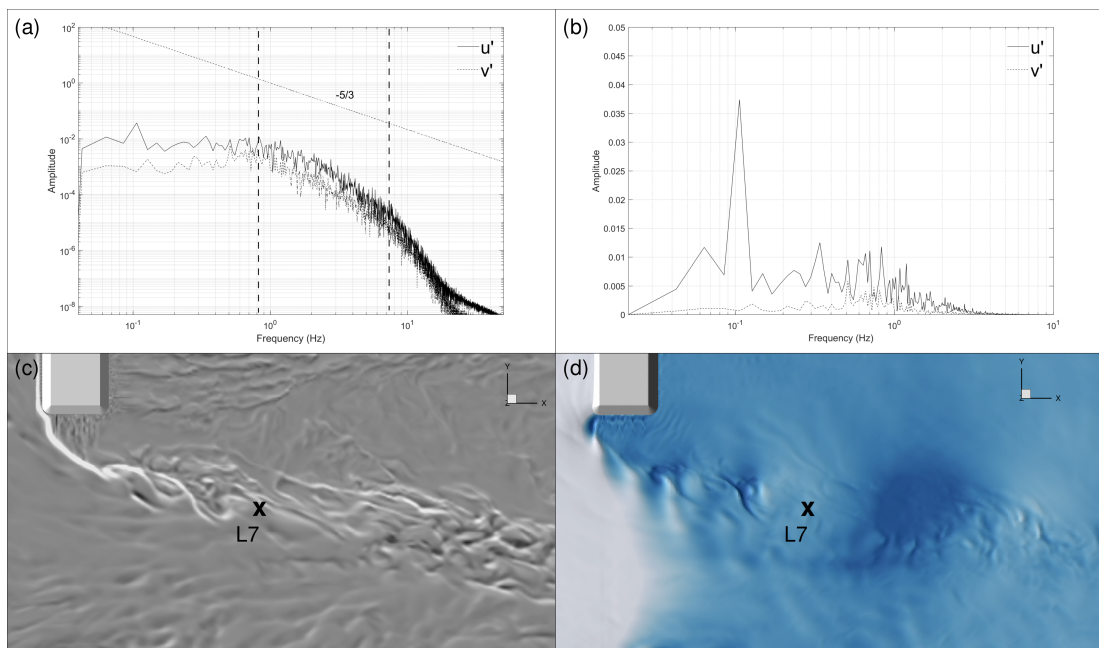


Figure 5.18: Power spectra of a streamwise and spanwise velocity fluctuation time series at location L7: (a) in log-log scale, (b) in semi-log scale, (c) wall-normal vorticity contours in a horizontal plane near the water surface and (d) water surface represented by zero level set colour-coded by the water depth for the SSB case.

5. THE EFFECT OF BRIDGE ABUTMENT LENGTH ON THE TURBULENCE STRUCTURE AND THE FLOW THROUGH THE OPENING

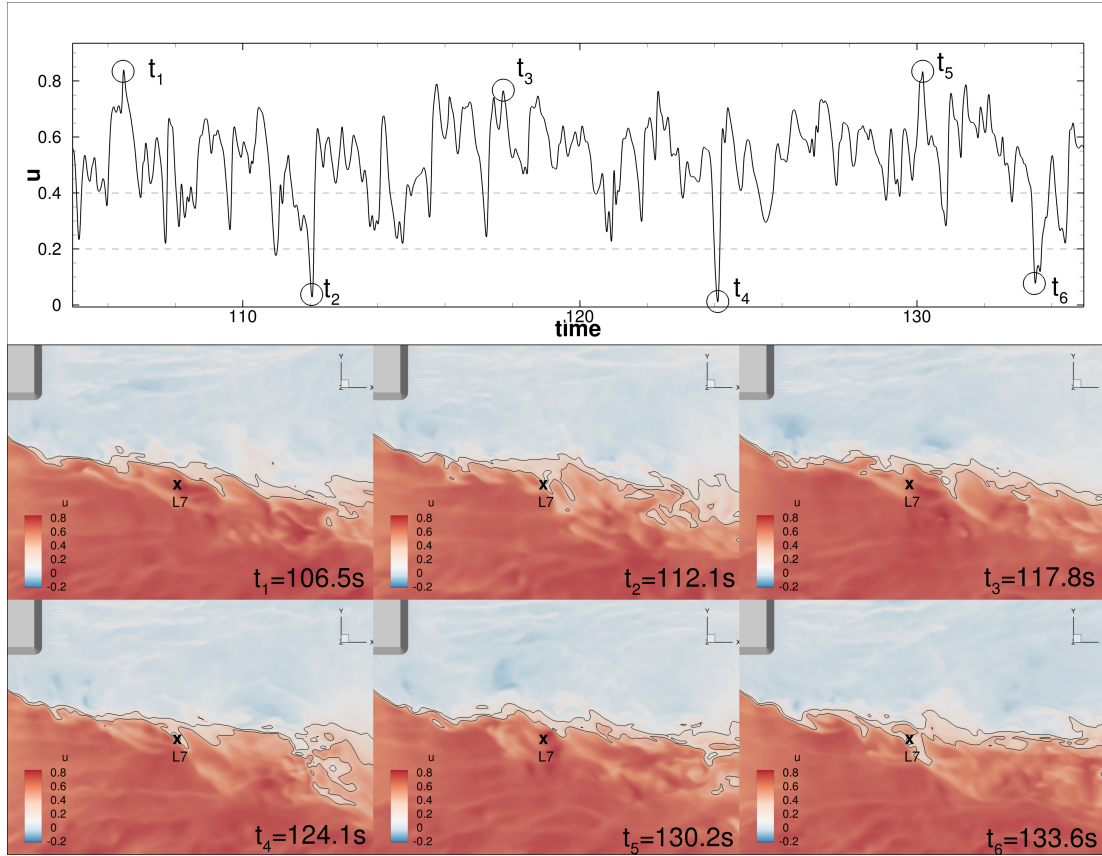


Figure 5.19: Time series of the streamwise velocity at location L7 of the SSB case and streamwise velocity contours at six selected instants in time labeled t_1 - t_6 .

eddy downstream of the left abutment and this can also be concluded from the fact that the v' spectra do not show any low-frequency peak. Moreover, the quadrant analysis (Fig. 5.15) also reveals the jet-like acceleration (almost one-dimensional flow) due to the narrow bridge opening with significantly greater u' than v' values. From animations of the flow downstream of the abutment it is seen that the 10s-periodicity correlates with a low-frequency meandering of the main channel flow as visualised by the instantaneous streamwise velocity flow field depicted in Fig. 5.8a.

Fig. 5.19 (top) shows a time series of the instantaneous streamwise velocity at L7 where distinctive high- and low-velocity peaks occur approximately every 10 s. The instantaneous streamwise velocity u contours at the six instants in time labelled in the time series (t_1 - t_6) are also presented below the timeseries

5. THE EFFECT OF BRIDGE ABUTMENT LENGTH ON THE TURBULENCE STRUCTURE AND THE FLOW THROUGH THE OPENING

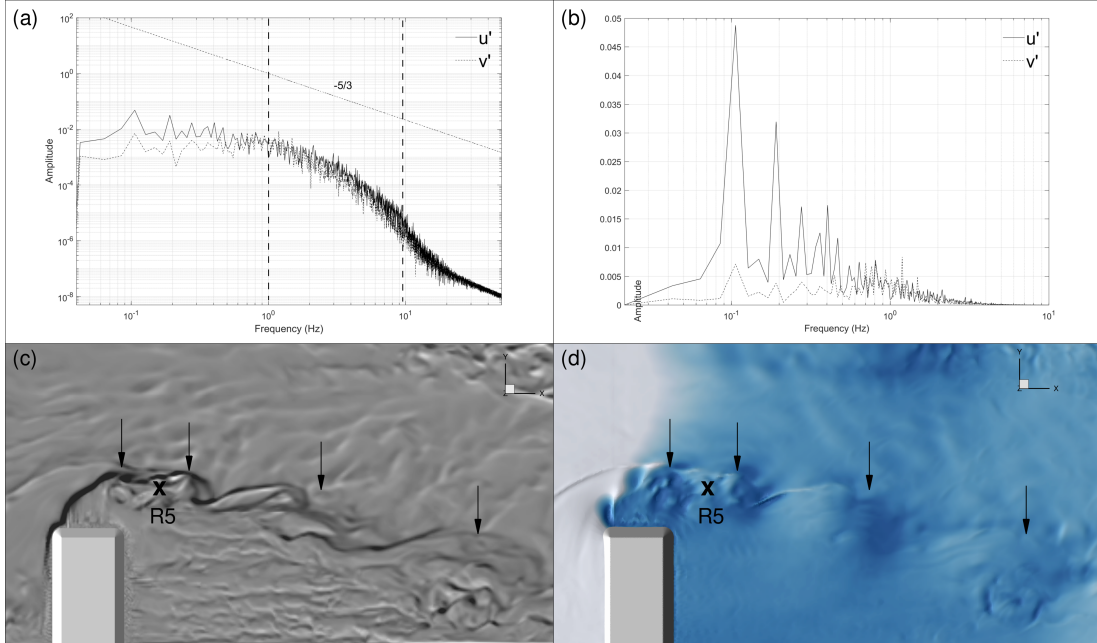


Figure 5.20: Power spectra of a streamwise and spanwise velocity fluctuation time series at location R5: (a) in log-log scale, (b) in semi-log scale, (c) wall-normal vorticity contours in a horizontal plane near the water surface and (d) water surface represented by zero level set colour-coded by the water depth for the SSB case.

to illustrate the shift between high velocities (dominant most of the time) and sudden low velocity peaks (at t_2 , t_4 and t_6). Two black lines representing 0.2 m/s and 0.4 m/s contours are included in the figure to highlight the boundary between the recirculation bubble and the main flow. This boundary oscillates due to the combination of the vorticity generated by the ejections from the bridge opening and the secondary flow at the main channel-floodplain interface, resulting in the characteristic 0.1 Hz meandering motion.

The turbulence characteristic at R5, downstream of the right abutment of the SSB case, is revealed with Fig. 5.20. The power spectra (Figs. 5.20a-b) show multiple peaks ranging from 0.1 Hz to 0.47 Hz, that can be correlated with several eddies (with periods between 2-10 s approx.) springing off the right abutment's tip as can be appreciated from Figs. 5.20c-d. The flow in this location is similar to the one behind the LSB abutment, however the relatively small peaks in the v' spectra suggest that the flow accelerates in a similar fashion at the right abutment

5. THE EFFECT OF BRIDGE ABUTMENT LENGTH ON THE TURBULENCE STRUCTURE AND THE FLOW THROUGH THE OPENING

than at the left leading to more irregular shedding of vortices and similarly to the LSB case, affected by the SSL, IV and NV vortices.

5.4 Closure

In this study the method of large eddy simulation (LES) has been employed to shed light on the complex flow around bridge abutments of different lengths, i.e. a long setback (LSB) abutment and a short setback (SSB) abutment, placed in a compound and asymmetric channel. A free surface algorithm has been included in the LES which has allowed predicting the free-surface deformation of the two investigated scenarios. Experimental data has been used to validate the two simulations and very convincing agreement of computed streamwise velocity profiles with the measured ones has been found. Similarly good agreement of LES-computed water surface elevations with experimental data has been observed and has thus established the credibility of the numerical method. The effect of the abutment length on the flow through and behind the bridge opening is visualised and quantified through instantaneous and time-averaged streamwise velocity contours as well as 2D and 3D streamlines which reveal several key differences: a) a significantly larger recirculation zone downstream of the left abutment but a smaller corner vortex in in SSB case in comparison with the LSB case; b) the main channel flow in the SSB is skewed more clearly towards the right bank due to the more accelerated flow and the larger recirculation zone downstream of the abutment of the SSB case; and c) more significant meandering of the flow downstream of the abutment in the SSB case. Turbulence structures, such as rolled-up shear layer-, necklace- and interface vortices due to the secondary flow, generated by the abutments and/or the compound channel geometry, respectively, are visualised using isosurfaces of the Q-criterion and wall-normal vorticity contours. The differences between LSB and SSB cases are: a) only in the SSB case, a very well-defined interface vortex is found at the interface between the main channel and the left floodplain; b) only in the LSB case, a pair of counter-rotating vortices appears near the surface in the vicinity of the left floodplain, being reflected in the free surface deformation in the form of a persistent bulging line.

5. THE EFFECT OF BRIDGE ABUTMENT LENGTH ON THE TURBULENCE STRUCTURE AND THE FLOW THROUGH THE OPENING

The turbulence structures have been quantified using three different techniques: probability density functions, quadrant analysis and power density spectra. The analyses of the time series of instantaneous velocity signals has quantified the complex turbulent flow near the abutments including: a) in the vicinity of the long setback abutment frequent occurrence of ejections of high momentum flow in the form of vortices springing off the tip of the abutment and rolling-up into low-frequency vortices, b) in the vicinity of the short setback abutment and due to the higher contraction ratio highly accelerated jet-like flow is dominating the turbulence which is fairly one-dimensional and persists over a substantial distance downstream of the abutment while convecting elongated shear layer vortices before they roll-up to become larger scale vortices c) the downstream flow of the short-setback abutment case is dominated by a meandering of the wake, and d) the flow around the right abutment in both cases features irregularity of vortex generation and shedding due to their interaction of with main-channel/floodplain interface vortices due to the secondary flow and necklace vortices.

5. THE EFFECT OF BRIDGE ABUTMENT LENGTH ON THE
TURBULENCE STRUCTURE AND THE FLOW THROUGH THE
OPENING

Chapter 6

Free Surface Flow around Bridge Abutment on Pre-scour and Equilibrium Scour Condition¹

6.1 Motivation and Objectives

This study attempts to contribute to the understanding of the complex flow mechanisms around bridge abutments in different scour stages. Large eddy simulations of the turbulent flow around the bridge abutments in two different bathymetries are performed, using the LSM to predict the free surface deformation. The first case is the flat bed case (FB) which corresponds to the initial pre-scour condition while the second case, the deformed bed case (DB), represents the equilibrium scour condition. Clear-water scour condition is applied in all cases where no sediment motion is considered upstream of the abutment. To achieve the best representation of a natural river, the computational domain consists of an asymmetrical compound geometry with a parabolic main channel in which two different length abutments with sloped sidewalls and rounded corners are placed. In order

¹Results from this chapter are directly adopted from the 4th journal paper listed in the section of related publications.

6. FREE SURFACE FLOW AROUND BRIDGE ABUTMENT ON PRE-SCOUR AND EQUILIBRIUM SCOUR CONDITION

to reduce the complexity and computational cost of the deformed bed case, only the scour bathymetry from the left side of the abutment (downstream view) is included. The convincing arguments from experiment observations are that as long as the scour hole does not extend to the opposite side of the scour hole (middle section remains undisturbed), the abutment scour can be considered as a local phenomenon and is independent of the contraction ratio [Cardoso and Bettess \[1999\]](#); [Laursen \[1963\]](#); [Melville \[1992\]](#). The novelty of the present study relies on the combination of several factors: a) a numerical setup that solves the larger scales of turbulence; b) fluid-structure interaction; c) free surface prediction; d) complex and realistic (compound and asymmetric) computational domain; and e) accurate representation of the scour bathymetry. To the best of the authors' knowledge, numerical work of such complexity has rarely been presented in the past. The present chapter begins with the validation of the large eddy simulation with complementary experimental results. Then, a discussion focusing on the change in flow behaviour before and after the scour formation is presented by means of time-averaged streamtraces, streamwise velocity, vertical velocity and turbulent kinetic energy. This is followed by the comparison of free surface undulation patterns between the cases. Lastly, near-bed quantities including the bed shear stress and near-bed turbulent kinetic energy are presented to highlight the transformation between scour stages.

6.2 Numerical and Experimental Setup

Two scenarios are simulated and discussed in this study: A flat bed (FB) simulation and a deformed bed (DB) simulation; representing the pre-scour flow condition and the equilibrium scour flow condition, respectively. The FB simulation is the same case as the LSB case presented in Chapter 5 and the results from that study is adopted here. Fig. 6.1(a) shows the full computational domain of the FB case which consists of a parabolic main channel, floodplains and abutments of unequal width and a bridge deck. This represents closely the physical domain of the complementary movable-bed experiment carried out at Georgia Institute of Technology, US ([Hong et al. \[2015\]](#)). The DB simulation includes

6. FREE SURFACE FLOW AROUND BRIDGE ABUTMENT ON PRE-SCOUR AND EQUILIBRIUM SCOUR CONDITION

the scour bathymetry near the left abutment which is obtained at the end of that experiment. The experiment allowed the flow to erode the moveable-bed for 5-6 days until equilibrium (bed elevation showed no change on its mean level for more than 24 hours) is achieved. The measurement of velocities and scour bed elevations were performed with a 3D down-looking ADV and point gauge around the abutments. The ADV can measure the distance from the center of the sampling volume to a solid boundary with $\pm 1mm$ uncertainty. However, sometimes the ADV is not able to detect precisely bed elevations along a steep slope so that measurements with a point gauge are needed. The point gauge has an uncertainty of $\pm 0.1mm$. The scour bathymetry surface was digitised and represented through a mesh of immersed boundary points to mimic an irregular solid boundary. Fig. 6.1(b) presents a zoomed-in view at the equilibrium bed bathymetry near the left abutment of the DB case (bridge not included in figure for unobstructed view). The bed bathymetry is colour-coded by the bed elevation in which zero value represents the deepest point of the main channel. 20 white columns are placed in the scour area to mark the locations where time-averaged streamwise velocity, $\langle u \rangle$ are extracted and compared between the two cases (will be presented in Fig. 6.5).

The full numerical domain is 4.26 m wide, 0.4 m deep (includes air above the free surface) and 15 m long. The left and right (downstream view) spill-through abutments which consist of a side slope of 2:1 are 1.06 m and 0.72 m long, respectively and have the same width and depth of 0.636 m and 0.084 m, respectively. The parabolic main channel has a width and depth of 0.96 m and 0.13 m, respectively. Lastly, a bridge (0.292m width) which spans the width of the domain is placed on top of the abutments.

The experimental conditions followed in the laboratory are carefully replicated in the numerical simulations. The flow conditions are identical in both FB and DB. The water discharge is set to $0.085 m^3/s$. The water depth was controlled by a tailgate during the experiments to ensure a water depth of 20 cm at the deepest part of the main channel under the bridge. In this 'free flow scenario', the water surface is not perturbed by the bridge at any point. The resulting bulk velocity is $U_b = 0.24 m/s$; the Reynolds numbers, based on the bulk velocity and four times the hydraulic radius Kara et al. [2012], is $Re = 76,300$; finally, the

6. FREE SURFACE FLOW AROUND BRIDGE ABUTMENT ON PRE-SCOUR AND EQUILIBRIUM SCOUR CONDITION

global Froude number, based on U_b and the average water depth is $Fr = 0.27$; local values based on local depths and velocities can be much higher.

The inflow condition of the simulation was fulfilled by fully developed turbulent flow. This was achieved by running precursor simulations in the absence of abutments and periodic open boundaries until convergence of first and second-order statistics was achieved. 10,000 time steps of 3-D instantaneous flow field at one cross-section of the periodic channel are recorded and are fed into the actual computational domain with bridge abutments. The inlet data are recycled to ensure a continuous fully-developed turbulent inflow for the duration of the simulation. Regarding the other boundary conditions, convective boundary conditions were adopted at the outlet which was conveniently located away from the scour and recirculation area ($\approx 12m$ downstream of abutment) to avoid interference with the focus of the simulation. The bed of the compound channel and side walls were treated as no-slip boundaries while the water surface was tracked using the level set method. The free surface was set as flat at the start of the simulation to an initial depth, h estimated from the experiment. The abutments, bridge, scour bathymetry and the parabolic channel boundaries are represented by Lagrangian immersed boundaries.

The domain was discretised into uniform grids of $3000 \times 852 \times 160$ in the streamwise, spanwise and wall normal directions, respectively, identical in both FB and DB cases. Total number of grid points of the entire domain is roughly 409 millions. The computational domains were divided into 3072 sub-domains for mpi-parallelisation. Each simulations were performed on 1024 cores on Supercomputing Wales' supercomputer and each simulations consumed approximately 200,000 CPU hours.

6.3 Results and Discussion

6.3.1 Validation

Profiles of computed and measured time-averaged streamwise velocity at six locations near the left abutment are plotted in Fig. 6.2 for the FB case. Points

6. FREE SURFACE FLOW AROUND BRIDGE ABUTMENT ON PRE-SCOUR AND EQUILIBRIUM SCOUR CONDITION

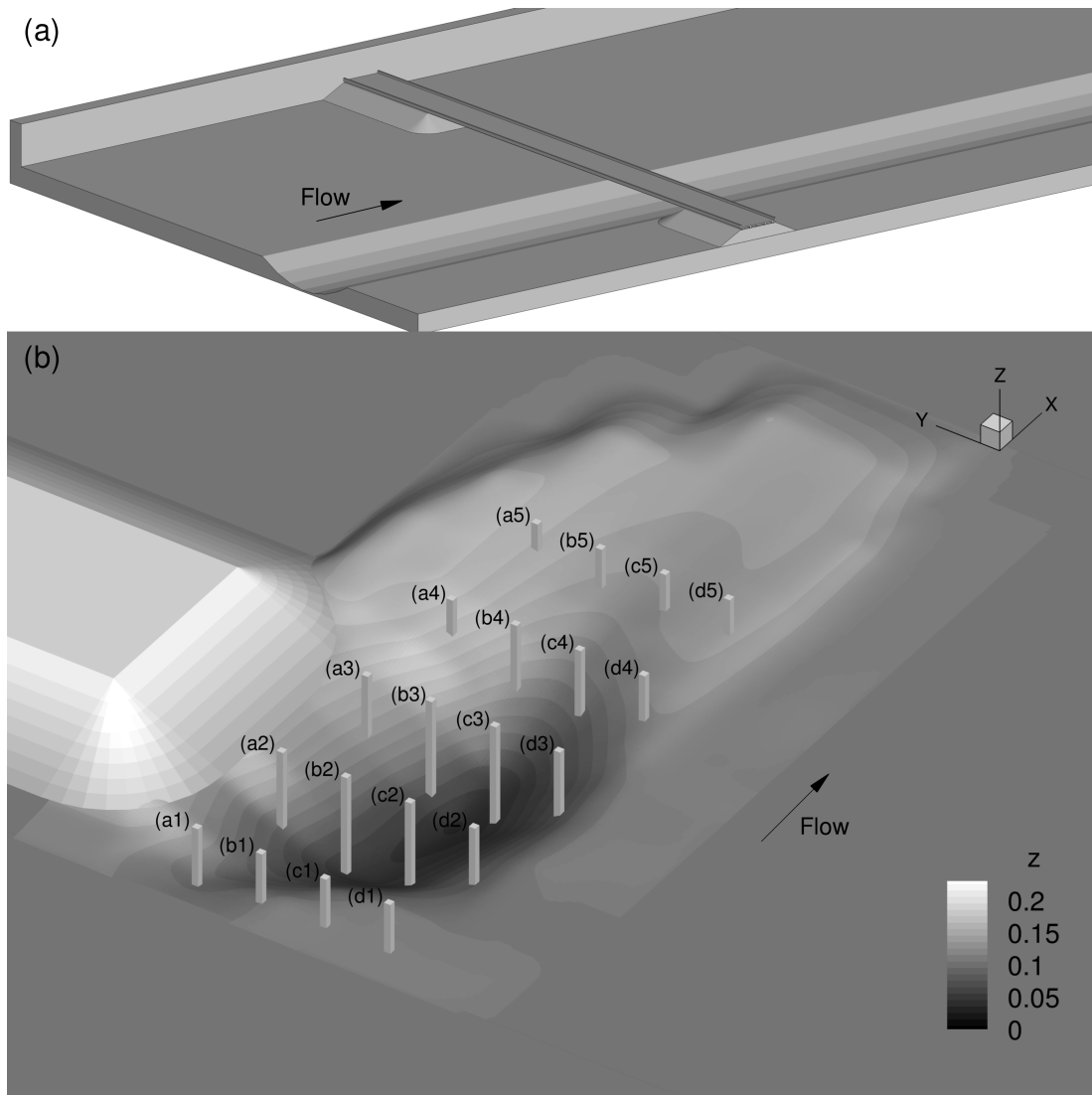


Figure 6.1: Computational Setup: (a) Flat bed case, FB; (b) Zoomed-in view of the scour bathymetry near the left abutment colour-coded with depth, z in the deformed bed case, DB. White columns are the markers of locations for the time-averaged streamwise velocity profile comparisons.

6. FREE SURFACE FLOW AROUND BRIDGE ABUTMENT ON PRE-SCOUR AND EQUILIBRIUM SCOUR CONDITION

(a)-(c) fall in line with the upstream toe of the abutment while points (d)-(f) are at the downstream face of the bridge. The profiles show reasonable agreement with the LES results despite a general overestimation of approx. 5-10%. The overestimation might be a result of any minor mismatch on the abutment and bed geometries. The velocity profiles away from the abutments including the main channel, nonetheless, are remarkably good as presented in Chapter 5. The LES result in profile (d), however, does not match the experiment very well in magnitude even though the shape of the profile follows the trend. This discrepancy could be related to the very unsteady nature inside the separated shear layer which increased the difficulty of measurement thus leading to some unavoidable errors. Grid sensitivity for the flat bed case is presented in Chapter 5 and have shown no significant improvement from coarse to fine grid resolution except at the near-bed region, which is important for scour related studies. The fine grid resolution is adopted in this paper for both cases.

6.3.2 Flow separation

3D streamtraces of the mean flow of both flat bed and deformed bed simulations are presented in Fig. 6.3, colour-coded with time-averaged streamwise velocity, $\langle u \rangle$. The general trends observed in both FB and DB cases are as follows: a) flow contraction happens as it approaches the abutments; b) flow separates at the tip of the upstream face of the abutments; and c) recirculation vortices form at the downstream end of the abutment. In the FB case, the flow motion is predominantly two-dimensional in the flat shallow floodplain. Two counter-rotating vortices can be found behind the left abutment: the smaller, corner vortex (CV) is circular with a diameter of roughly the length of the left abutment while the main vortex (MV) is oval and long (see Fig. 6.3(a)). Zooming in at the tip of the left abutment (Fig. 6.3(b)), the flow creates a distinct separated shear layer (SSL) which is a result of the interaction between the fast flowing contraction flow and recirculation zone behind the abutment (highlighted as dashed line in Fig. 6.3(b)). Within the SSL, coherent structures shed from the abutment tip, interact with each other, travel downstream and subsequently break down into smaller scale structures. Detailed description of this shedding mechanism can be

6. FREE SURFACE FLOW AROUND BRIDGE ABUTMENT ON PRE-SCOUR AND EQUILIBRIUM SCOUR CONDITION

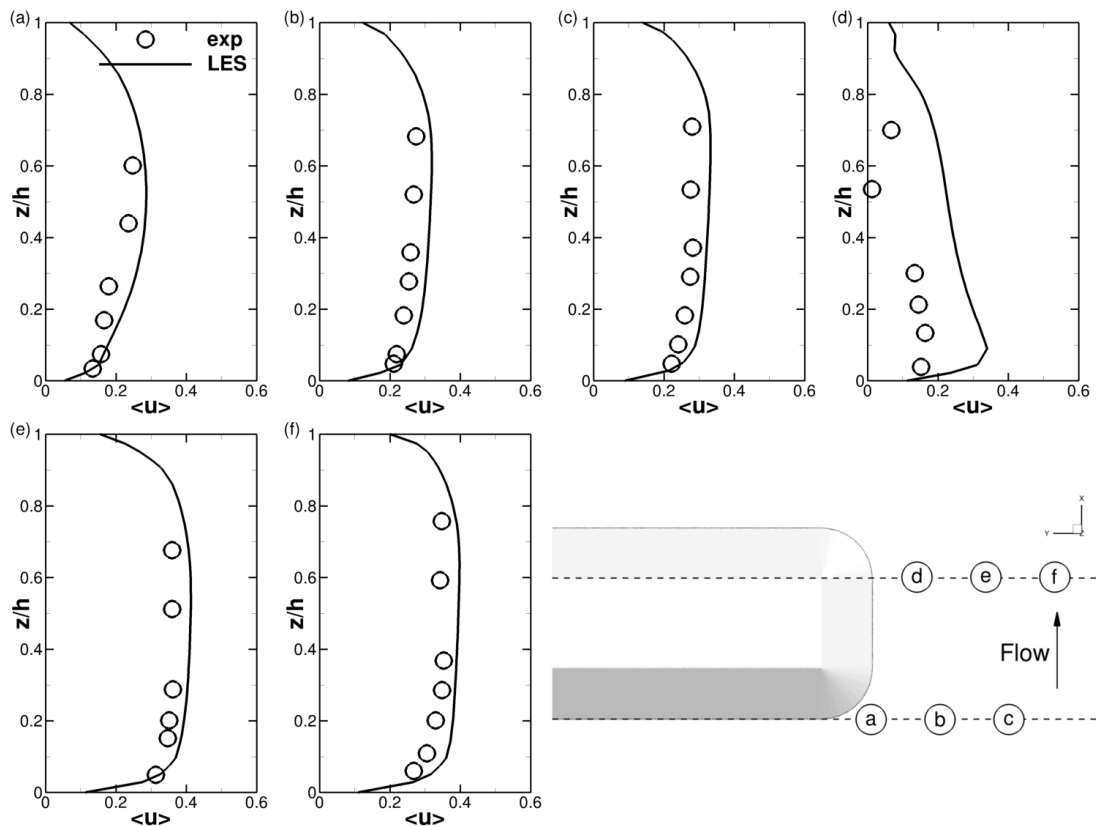


Figure 6.2: Validation of LES time-averaged streamwise velocities with experimental data for FB case near the left abutment; Circle represents experimental data and solid line represents LES; Locations of profiles (a)-(f) are marked in the bottom right sub-figure.

6. FREE SURFACE FLOW AROUND BRIDGE ABUTMENT ON PRE-SCOUR AND EQUILIBRIUM SCOUR CONDITION

found in Chapter 5.

The flow behaviour in DB is significantly different from that in FB due to the deformed bed geometry. A tiny recirculation bubble can be found inside the scour hole which completely disrupts the separation at the abutment's tip. The streamtraces reveal how flow rushes into the scour hole underneath the recirculation bubble and leaves the scour region in a non-uniform manner. The result is a complex three-dimensional flow at the abutment's tip (see Fig. 6.3(d)). A small portion of the flow (indicated by small arrow in Fig. 6.3(d)) escapes the scour hole and travels directly to the back of the left abutment. This may have caused the CV found behind the left abutment in FB case to lose its regularity and to detach from the left abutment. Consequently, the core of the main recirculating eddy, MV is split into two by the CV in between and is pushed further downstream, reaching up to $x/b = 2.42$ in contrast to only $x/b = 1.82$ in FB. The angle of the flow separation has also been reduced quite notably after the scour formation has happened (12.1° in FB to 8.1° in DB). The streamtraces in DB immediately downstream of the deformed region are almost parallel to the side walls; as opposed to FB, the streamtraces curve noticeably more towards the main channel. On the other side of the channel, the corner vortices behind the right abutment for both cases are close to identical as both flows reattach to the right wall at same distance downstream.

As expected, the contraction between the abutments causes the flow to accelerate very significantly. In both FB and DB, the highest streamwise velocity region, up to twice the bulk velocity, concentrates above the main channel downstream of the abutments. However, the streamwise velocity of the MV recirculation cells are markedly different between the two cases; the MV in DB case has a significantly lower velocity, maxing out at approximately 0.15 m/s in both positive and negative directions whereas in FB, the MV circulates at a velocity of more than 0.25 m/s . This is due to the momentum invested in the scour hole vorticity. Generally, the existence of the deformed bed region has resulted in a considerably weaker recirculation system behind the left abutment which highlights the transition of flow behaviour before and after a scour formation.

To investigate further the three-dimensional behaviour of the flow after the scour equilibrium, longitudinal XZ sections of the time-averaged vertical velocity,

6. FREE SURFACE FLOW AROUND BRIDGE ABUTMENT ON PRE-SCOUR AND EQUILIBRIUM SCOUR CONDITION

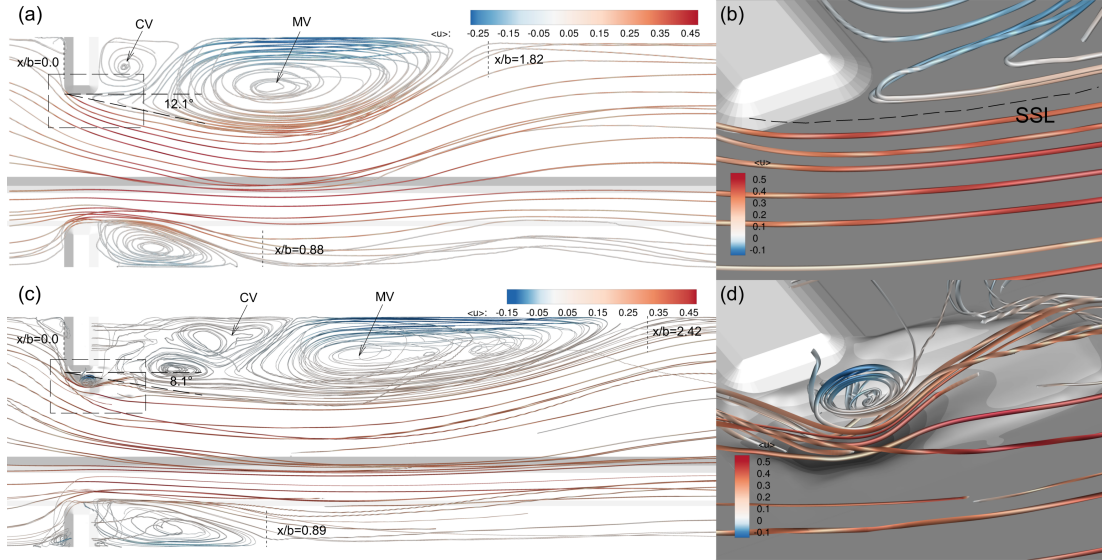


Figure 6.3: Time-averaged 3D streamtraces colour-coded by time-averaged streamwise velocity; On the left, top-down views of (a) FB and (c) DB; on the right, zoomed-in views of (b) FB and (d) DB, near left abutment.

$\langle w \rangle$ contour (normalised by the critical shear velocity for initiation of motion, u_{*c0}) near the left abutment for both FB and DB are displayed in Fig. 6.4(a) and (b), respectively. The values of the vertical velocity greatly differ between the cases, being $\langle w \rangle$ in DB almost an order of magnitude larger than that in the FB setup (i.e. $-9.6 < \langle w \rangle / u_{*c} < 10.2$ in DB and $-1.3 < \langle w \rangle / u_{*c} < 1.5$ in FB). As the flow approaches the abutment and the scour hole, it plunges into the deepest part of the erosion with high negative vertical velocity followed by an immediate upflow over the deposition zone (most noticeable in the second XZ slice away from the abutment (Fig. 6.4(b)). The same phenomena cannot describe the FB case as vertical flow is virtually negligible. The only notable downflow area is found near the upstream corner of the abutment where an increase of velocity and consequently drop in pressure is observed.

The normalised turbulence kinetic energy (tke), k/u_{*c0}^2 contours on four XZ slices near the left abutment for both FB and DB are presented in Fig. 6.4 (c) and (d), respectively. Both cases portray the tke contours very differently. In the flat bed simulation (Fig. 6.4(c)), the high value of k occurs at the separated shear layer where most of the coherent structures are shed and convected down-

6. FREE SURFACE FLOW AROUND BRIDGE ABUTMENT ON PRE-SCOUR AND EQUILIBRIUM SCOUR CONDITION

stream, indicating the high degree of turbulence in the region. Nonetheless, in the deformed bed simulation, the high tke regions follow a more complex pattern (Fig. 6.4(d)). Interestingly, at the downslope of the third XZ slice away from the abutment, a peak (signaled with small arrow) is found very close to the bed. This peak is most likely associated with the plunging flow coming into the scour hole which interacts with the low velocity region in the scour to produce high turbulence.

Fig. 6.5 presents the time-averaged streamwise velocity profiles, $\langle u \rangle$ normalised by the critical shear velocity at flat bed, u_{*c0} of FB and DB cases at 20 locations previously labelled in Fig. 6.1(b). The vertical axis is depth, z normalised by the approximate water depth at the respective locations, h_w to enable both cases on the same scale axis even though bed elevation differs from point to point. Dashed lines and solid lines represent flat bed and deformed bed simulations, respectively. In the first row of points, a1-d1, both simulations show similar streamwise velocity profiles since the points are located just upstream of the abutment with little to none bed erosion. As flow progresses into the scour area, significant divergence between the profiles are noticed. The streamwise velocity gradient near to the bed is markedly lower in the DB case especially at points b2, c2, and d2-d5, revealing that the scoured bed in equilibrium minimises the bed shear stresses on the bed for DB. Profiles a2-a5 are with smallest values and both cases exhibit very different dynamics in this area. DB decelerates much earlier down to near zero velocity at a4 and immediately accelerates up the deposition area at a5. The negative velocity at a3 supports the presence of the tiny recirculation zone discussed in Fig. 6.3(d). In contrast, the flow in FB gradually slows down to zero velocity at a5 which it falls at the tip of the MV vortex shown in Fig. 6.3(c).

6.3.3 Free surface

Fig. 6.6 presents the instantaneous free surface deformation around the scour hole represented by $\phi = 0$ level-set isosurface for (a) FB and (b) DB. The vertical axis of the figures is exaggerated to highlight surface deformation features. The isosurfaces are colour-coded by the normalised water depth, z/h in which dark

6. FREE SURFACE FLOW AROUND BRIDGE ABUTMENT ON PRE-SCOUR AND EQUILIBRIUM SCOUR CONDITION

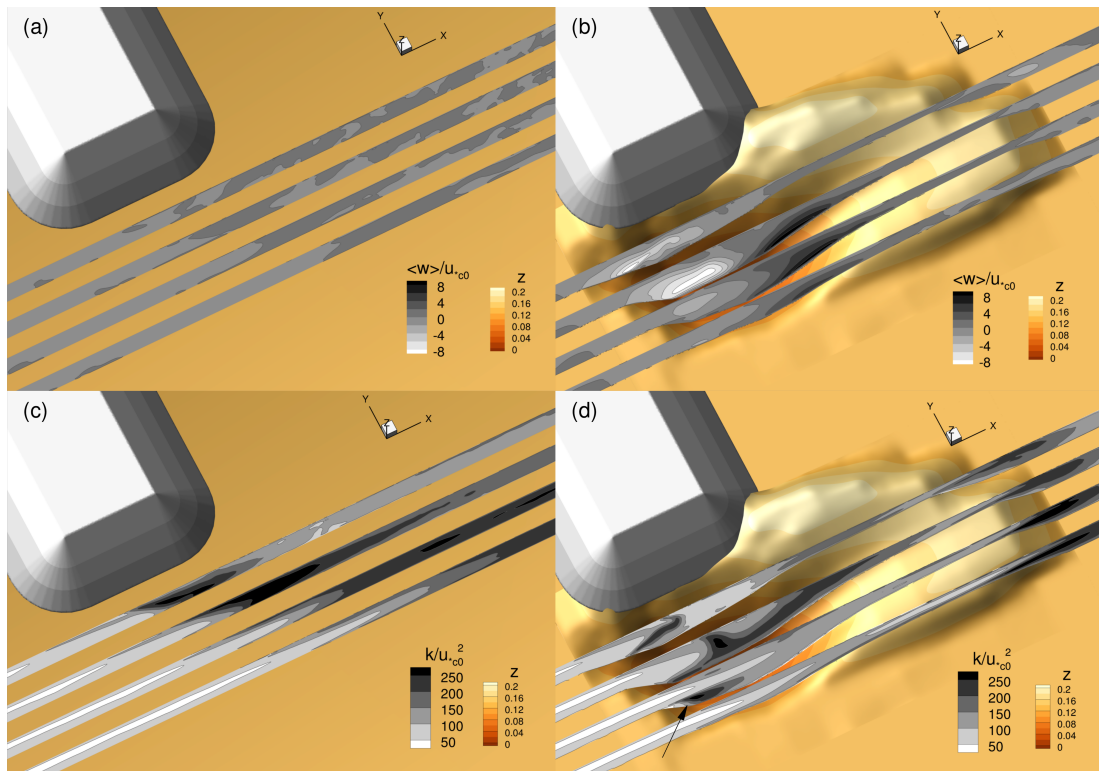


Figure 6.4: (a)-(b) Non-dimensional time-averaged vertical velocity contours for FB (left) and DB (right), respectively; (c)-(d) Non-dimensional turbulent kinetic energy contours for FB and DB, respectively; All contours on four XZ slices near left abutment.

6. FREE SURFACE FLOW AROUND BRIDGE ABUTMENT ON PRE-SCOUR AND EQUILIBRIUM SCOUR CONDITION

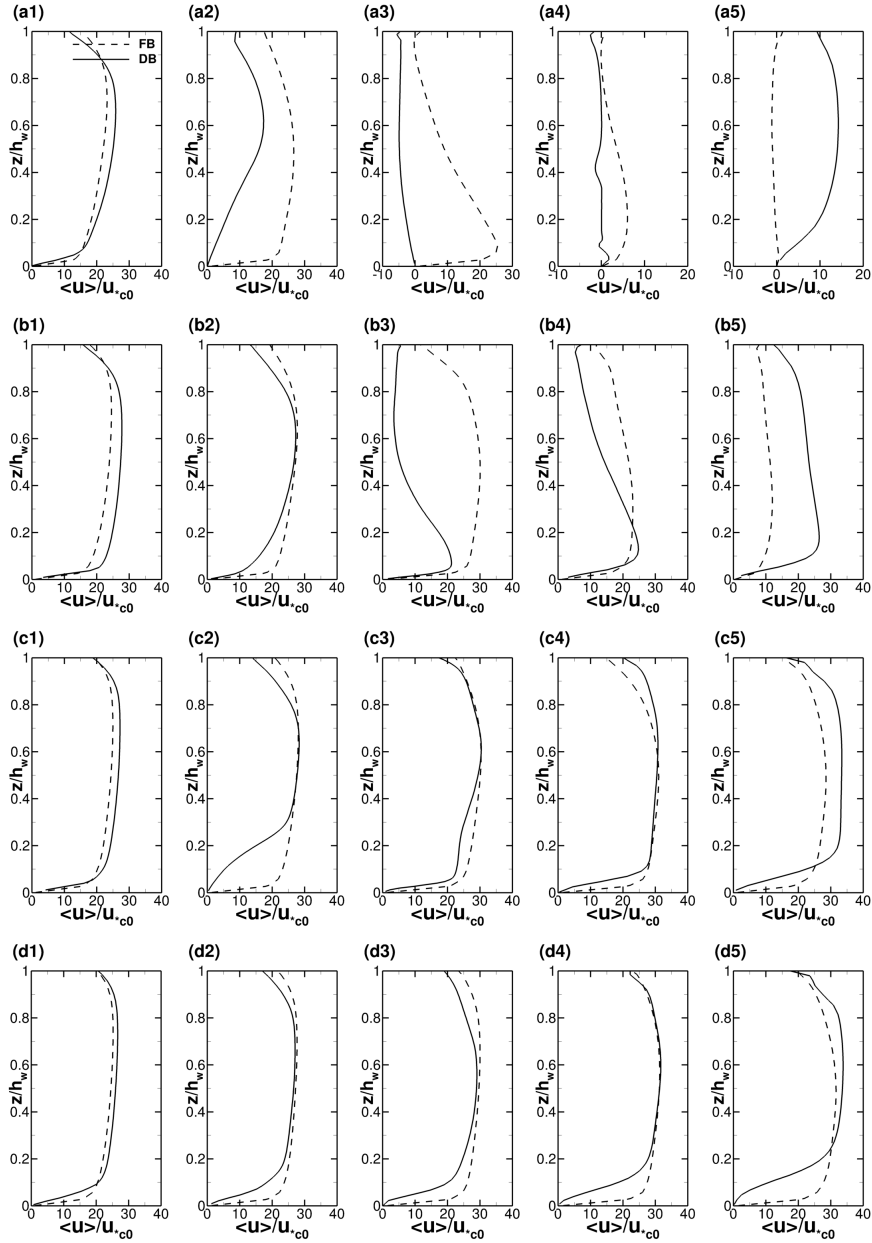


Figure 6.5: Time-averaged streamwise velocity profiles at 20 locations labeled in Fig. 6.1(b) for FB (dashed line) and DB (solid line).

6. FREE SURFACE FLOW AROUND BRIDGE ABUTMENT ON PRE-SCOUR AND EQUILIBRIUM SCOUR CONDITION

blue depicts the depressions and white portrays high elevation. The difference in the pattern of the water surface deformation is fairly obvious between the two cases. For instance, in FB, the water surface disturbance follows the path of the SSL shown in Fig. 6.3. Patches of depression (signalled with small arrows in Fig. 6.6(a)) are observed to travel downstream periodically due to the presence of coherent structures underneath. In DB, however, the area of water surface disturbance is more widely spread out in the all directions. Looking at the free surface animations, tiny tornado-like features are spotted above the deepest part of the scour hole (signalled with small arrow in Fig. 6.6(b)), but are quickly broken down as they approach the deposition zone. Interestingly, in the DB case, waves/ripples are observed diagonally downstream of the left abutment are possibly caused by the occurrence of the plunge/ejection actions in the scour hole.

To quantify the actual difference in water elevation between the cases, profiles of the isosurfaces at five planes (see labels in Fig. 6.6) are extracted and being plotted against each other in Fig. 6.7. Solid lines represent the flat bed, FB case whereas circles with solid lines represent the deformed bed, DB case. The general trend of the comparison shows that the integral water elevation in DB is lower than that in FB. The x1 profile is located at the upstream face of the bridge where the flow turns around the upstream corner of the abutment and due to the acceleration caused by the flow contraction, both surfaces dip significantly. However, the depression in DB extends further away from the abutment up to two times of that found in FB, highlighting the influence of the scour hole towards the free surface. Moving even further away from the abutment, the effect of local acceleration loses its influence on the free surface as both surface lines meet at 0.2025 m height. The surface dip in FB due to the vortex shedding pointed out in Fig. 6.6(a) shows up in x2 and y1 profiles at approx. $y = 0.16 \text{ m}$ and $x = 0.41 \text{ m}$, respectively. The flow contraction causes the water surface to rise upstream of the abutments, followed by a drop while passing them and this is portrayed in the longitudinal profiles, y1 and y2. Both FB and DB lines have a downward slope as they approach the abutment but DB enters the area with an overall lower depth. The rise and drop of the surface for DB shown in y1 between $x = 0.6 - 1.0 \text{ m}$ indicates the presence of the deposition 'hill' after the scour hole (Fig. 6.7(y1)). The y3 profile is located furthest away from the abutment. The FB line has a

6. FREE SURFACE FLOW AROUND BRIDGE ABUTMENT ON PRE-SCOUR AND EQUILIBRIUM SCOUR CONDITION

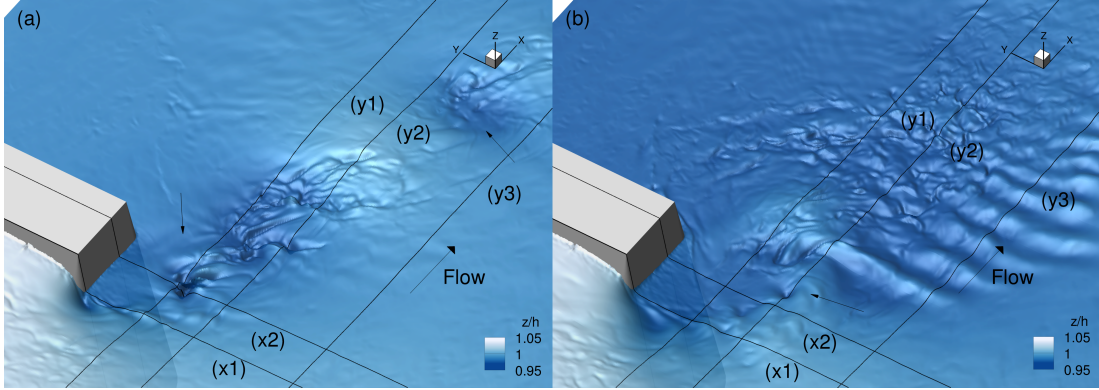


Figure 6.6: Water surface deformation (represented by zero level set) colour-coded by the normalised water depth, z/h near the left abutment, (a)FB, (b) DB.

very flat profile where not much disturbance is observed. For DB, however, the wavy surface is captured and it is noticeable only after $x \approx 0.65$ where the scour region ends. This is an interesting finding as it shows that the plunge/ejection mechanism has affected the water surface fairly significantly albeit away from the scour region.

6.3.4 Bed shear stress

Fig. 6.9 demonstrates the bed shear stress, τ_w comparison near the abutment between the flat bed and the deformed bed cases. Both instantaneous and time-averaged bed shear stress are normalised by the critical bed shear stress for the initiation of motion, $\tau_{wc0} = \rho u_{*c0}^2$ on the flat bed, where ρ is the density of fluid and u_{*c0} is the critical value of shear velocity based on the Shield's diagram on flat bed (Sturm [2001]). For DB, this critical value, however, has to be adjusted accordingly to take into account the gravitational bed slope effects at the scour region. The adjustment formula proposed by Jensen et al. [2006] is adopted which accounts for bed slope effects based on the angle of repose of sand (33° in present simulation) and the local maximum angle of the inclined surface with the horizontal. The adjusted critical bed shear stress is $\tau_{wc} = \rho u_{*c}^2$. Compared to the horizontal flat bed, the critical bed shear stress for sediment motion is increased up a slope and reduced for sediment motion down a slope. Zones of $\frac{\tau_w}{\tau_{wc0}} > 1$ and $\frac{\tau_w}{\tau_{wc}} > 1$ which depict possible sediment entrainment activities are

6. FREE SURFACE FLOW AROUND BRIDGE ABUTMENT ON PRE-SCOUR AND EQUILIBRIUM SCOUR CONDITION

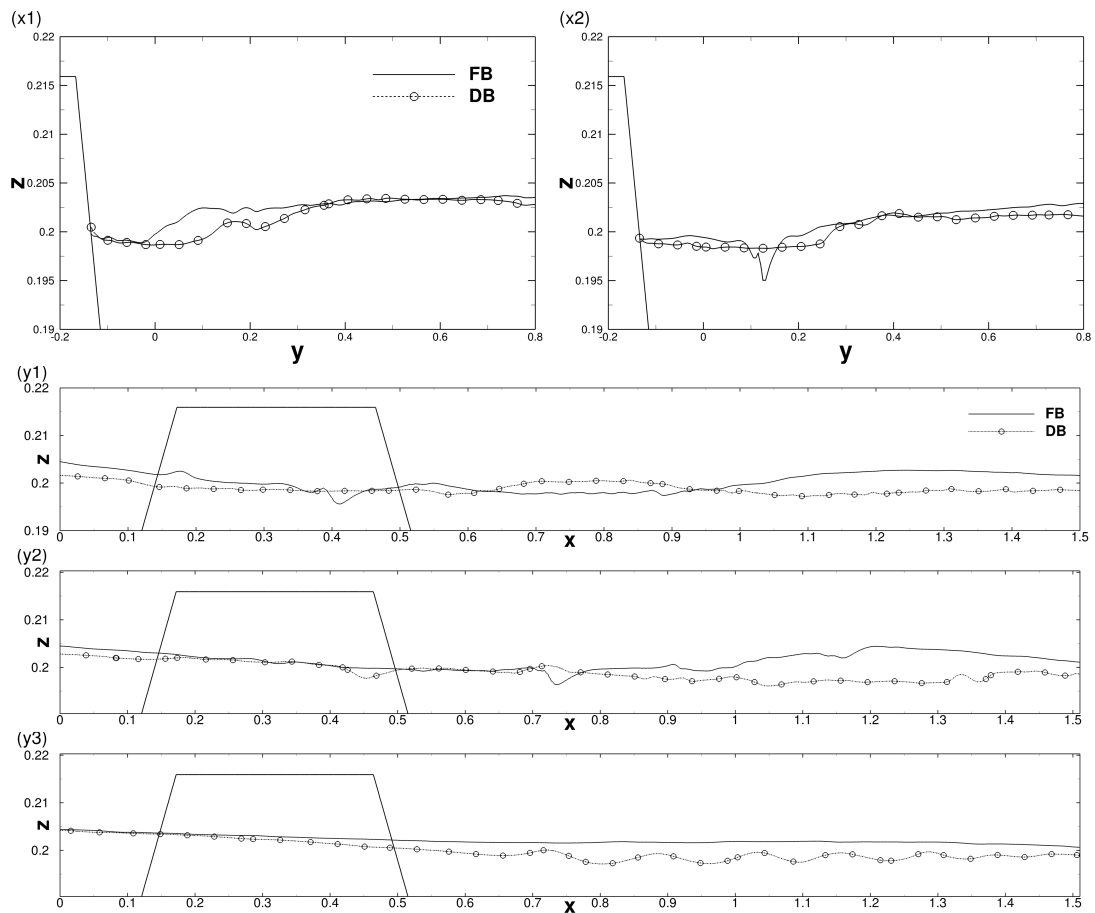


Figure 6.7: Instantaneous water surface profiles at transverse planes (x1)-(x2) and longitudinal planes (y1)-(y2) for FB (solid lines) and DB (circles with solid lines).

6. FREE SURFACE FLOW AROUND BRIDGE ABUTMENT ON PRE-SCOUR AND EQUILIBRIUM SCOUR CONDITION

highlighted with white borders.

The instantaneous dimensionless bed shear stress contour of FB (Fig. 6.8(a)) shows several peaks of $\tau_w > \tau_{wc0}$ along the observed separated shear layer. These peaks coincides with the vortex cores shed from the abutment as flow divergence happens. As this value is averaged over time (Fig. 6.8(c)), a single peak of τ_w greater than the critical value is found at the upstream corner of the abutment where the scouring process is expected to begin. This observation agrees well with experimental observations found in [Ettema et al. \[2010\]](#). Comparing to the DB case in Fig. 6.8(b) and (d), the normalised bed shear stress in the equilibrium state is reduced considerably over the whole area, consistent with the previous observations on the streamwise velocity bed gradients (Fig. 6.5). To quantify this, two longitudinal slices (y1 and y2) and two transverse slices (x1 and x2) of the time-averaged dimensionless bed shear stress are extracted from both cases and plotted against each other in Fig. 6.9. It is clear that the overall bed shear stress in the scour region has been reduced significantly (circles with solid lines in Fig. 6.9), down to zero in areas away from the scour hole. In deeper parts of the scour hole, the normalised bed shear stress is higher. Two particularly interesting peaks of $\frac{\tau_w}{\tau_{wc}} > 1$ are found in both instantaneous and time-averaged plots (Fig. 6.8(b) and (d)). The first peak is located at the downslope of the scour hole where the plunging flow described in Fig. 6.4(b) takes place. Due to this strong downflow, it is reasonable to expect that the scour process was, strictly speaking, still happening. These sediments are very likely to be entrained into the mini recirculation zone shown in Fig. 6.3(d) where the slow-moving vortex keeps the sediment from escaping the scour hole and eventually settles down in the scour hole under the influence of gravity. This basically creates a cycle of local entrainment and deposition in the scour region in which the net flux of sediment outside of this region is negligible in the equilibrium scour condition. The second peak is found at the up slope, just downstream of the deepest part of the scour hole. The possible explanation for the high value is due to the immediate acceleration of the flow 'uphill' the deposition region which causes sediment entrainment. However, due to the relatively steep slope in this area, sand slides are very likely to happen and sediments fall backwards into the scour hole which balances the net sediment movement. This analysis has shown very

6. FREE SURFACE FLOW AROUND BRIDGE ABUTMENT ON PRE-SCOUR AND EQUILIBRIUM SCOUR CONDITION

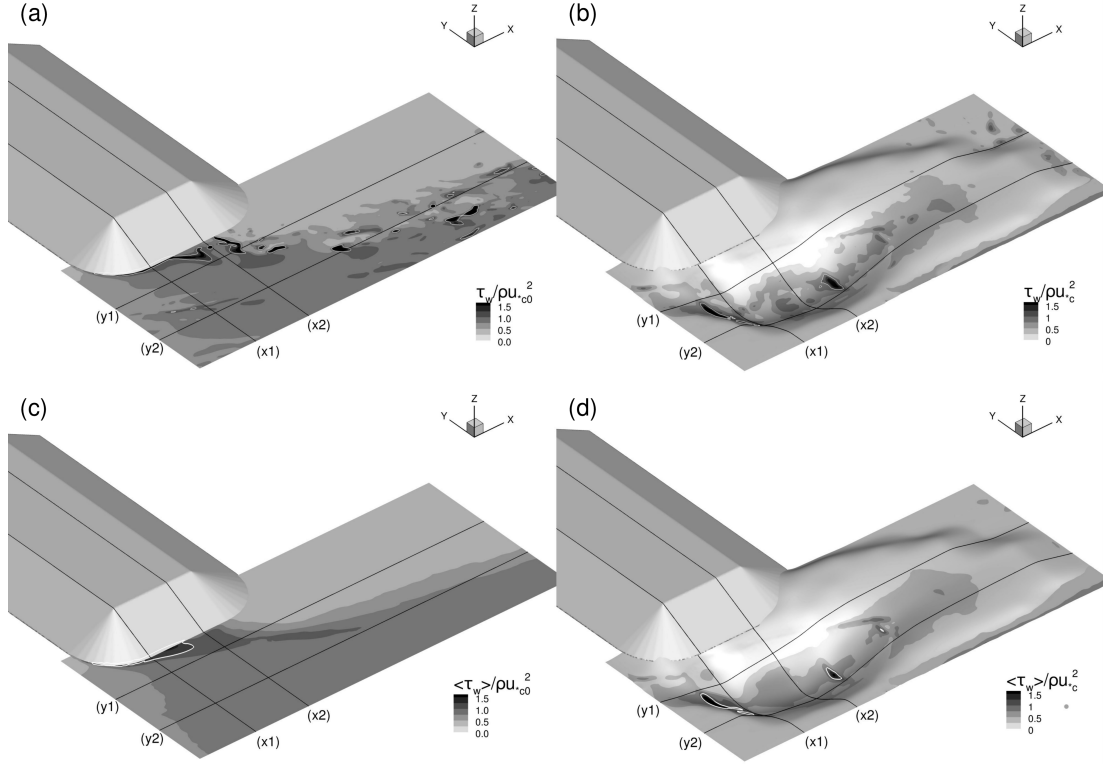


Figure 6.8: Instantaneous (top) and time-averaged (bottom) normalised bed shear stress distribution near the left abutment for FB (left) and DB (right).

clearly the huge reduction in bed shear stress over the scour region which suggests that the equilibrium scour stage was indeed achieved in the experiment.

6.3.5 Near-bed turbulent kinetic energy

Hong et al. [2015] carried out experiments and parameterized near-bed turbulent kinetic energy as one of the important ingredients of the erosion mechanism by demonstrating the relation between initial pre-scour near-bed turbulent kinetic energy and the location of the deepest scour for flow through different abutment lengths. Fig. 6.10 (a) and (b) present the near-bed nondimensional turbulent kinetic energy for FB and DB, respectively. As expected, also shown in Fig. 6.4(c), the near-bed turbulent kinetic energy (*tke*) of the flat bed simulation concentrates along the separated shear layer where most of the turbulent motion

6. FREE SURFACE FLOW AROUND BRIDGE ABUTMENT ON PRE-SCOUR AND EQUILIBRIUM SCOUR CONDITION

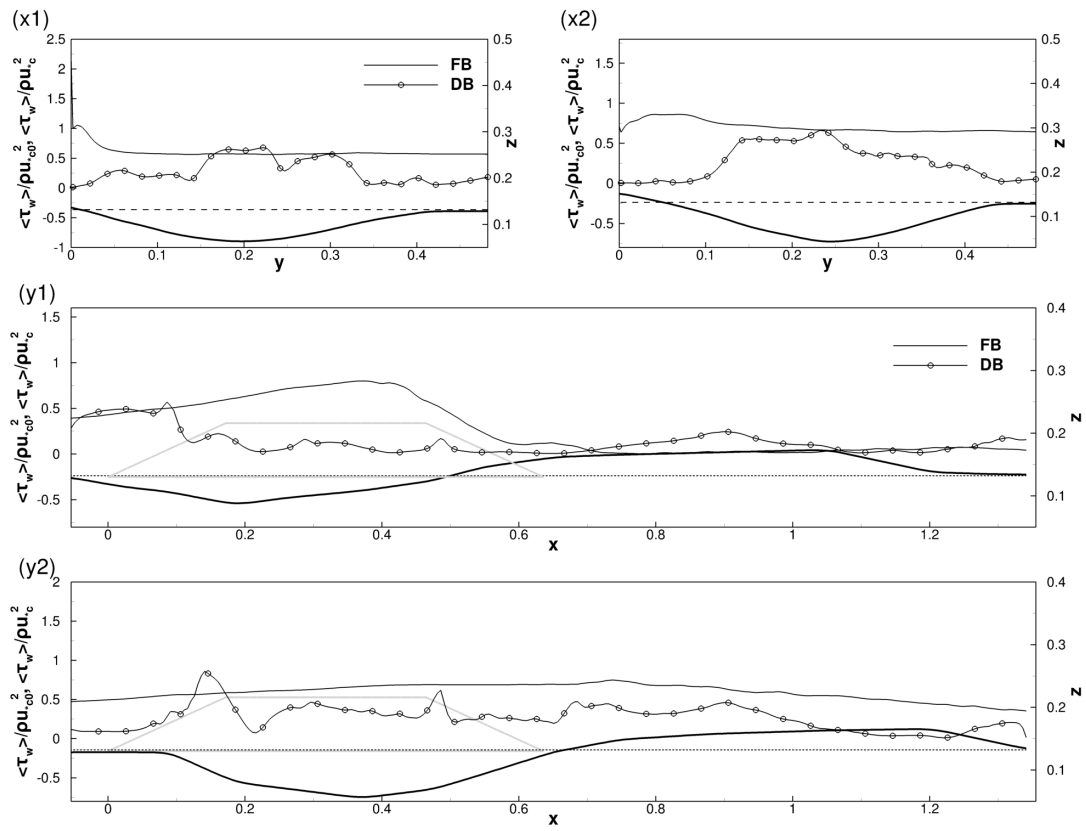


Figure 6.9: Time-averaged normalised bed shear stress profiles at transverse planes(x1)-(x2) and longitudinal planes (y1)-(y2) for FB (solid lines) and DB (circles with solid lines).

6. FREE SURFACE FLOW AROUND BRIDGE ABUTMENT ON PRE-SCOUR AND EQUILIBRIUM SCOUR CONDITION

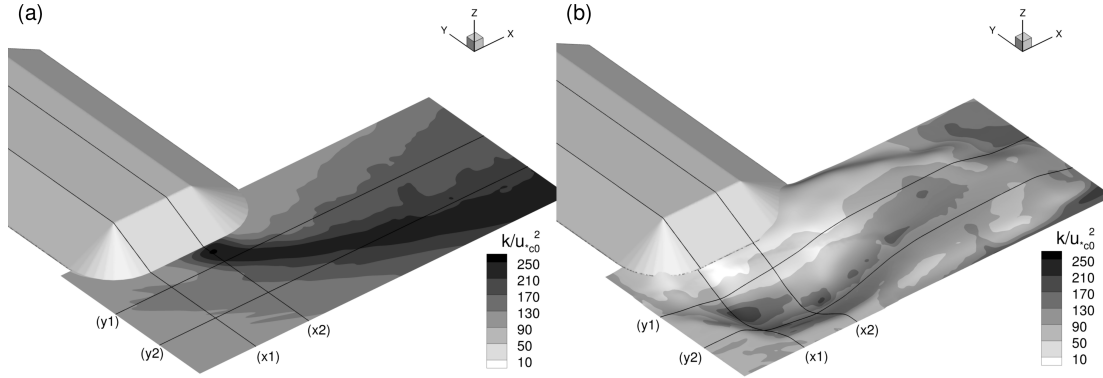


Figure 6.10: Near-bed normalised turbulent kinetic energy distribution near left abutment for (a) FB and (b) DB.

occurs. However, the high near-bed *tke* region does not coincide entirely with the time-averaged bed shear stress peak presented in Fig. 6.8(c), showing that high turbulence near-bed is not the only factor responsible for local scour but rather a combination of flow acceleration due to lateral flow contraction and turbulence caused by flow separation. Comparing the *tke* distribution between the FB and DB simulations, the strip of high *tke* region found in FB is completely absent after the scour formation. As discussed previously in Fig. 6.4(d), the *tke* peak concentrates at the downslope region of the scour hole created by the interaction between the downward plummeting flow and the low velocity pocket inside the scour. These differences in *tke* are quantified in Fig. 6.11 and the peaks in FB and DB are captured in slice (x2) and slice (x1), respectively. The maximum value of near-bed *tke* in FB reaches 250 whereas in DB, it tops at approximately 200. Focusing on the longitudinal slices, (y1) and (y2), the overall near-bed *tke* in DB is drastically lower up to 5 times smaller at a certain point (e.g. $x \approx 0.8$ in (y2)). Once again, the reduction in overall near-bed *tke* in the deformed bed simulation provides an indication on degradation in the bed erosion process, thus the equilibrium scour state.

6. FREE SURFACE FLOW AROUND BRIDGE ABUTMENT ON PRE-SCOUR AND EQUILIBRIUM SCOUR CONDITION

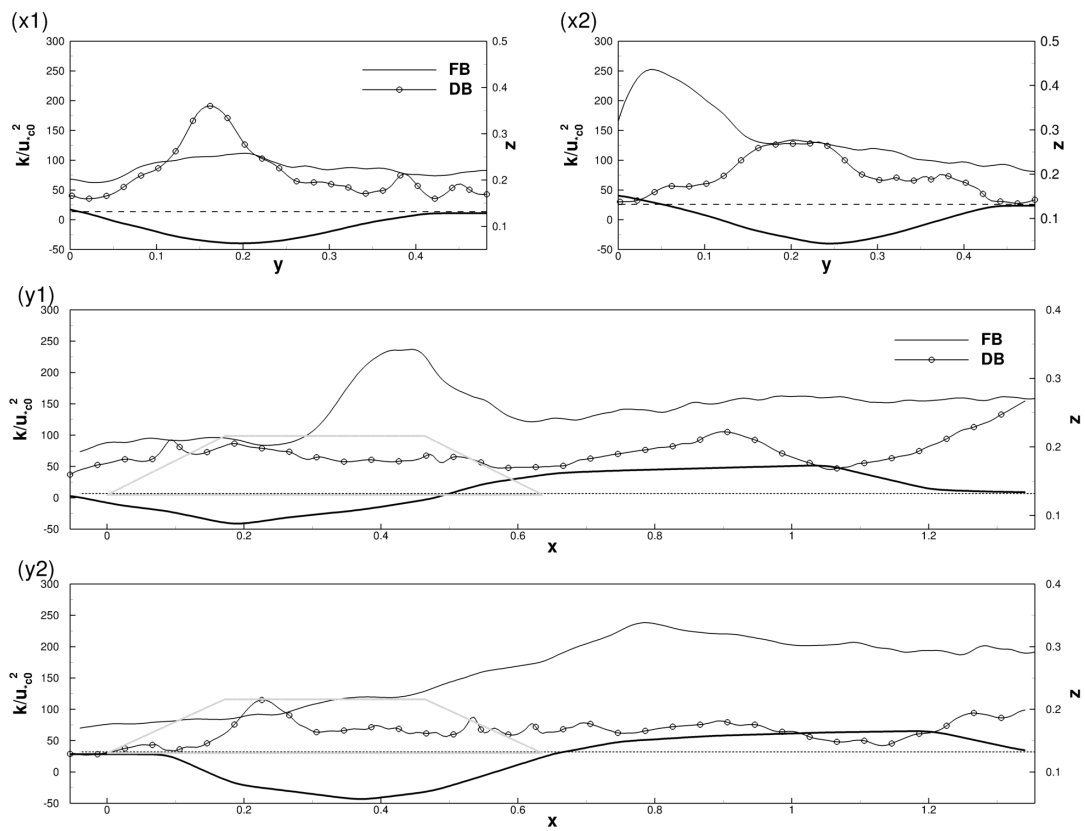


Figure 6.11: Near-bed normalised turbulent kinetic energy profiles at transverse planes(x1)-(x2) and longitudinal planes (y1)-(y2) for FB (solid lines) and DB (circles with solid lines).

6.4 Closure

The present study has employed the method of large eddy simulation (LES) to shed light on the complex flow around bridge abutments placed in a compound and asymmetric channel in different scour stages, i.e. a pre-scour condition, flat bed (FB) case and an equilibrium scour condition, deformed bed (DB) case. A free surface algorithm has been included in the LES which has allowed the prediction of the free-surface deformation of the two investigated scenarios. Experimental data has been used to validate the FB simulation and reasonable agreement of computed streamwise velocity profiles with the measured ones has been found, thus establishing the credibility of the numerical method. The flow dynamics through and behind the bridge opening on the different scour stages are visualised and quantified through 3D streamlines as well as time-averaged vertical velocity and turbulent kinetic energy (*tke*) contours which reveal several key differences: a) an increase in flow three-dimensionality for the DB case in the scour region; b) a significantly longer recirculation zone behind the left abutment in the DB case; and c) stronger vertical plunging flow into the scour region in the DB case. The changes in turbulence characteristics near the left abutment along the separated shear layer after the scour formation are reflected on the free surface deformation where in the DB case, the depression is generally more significant when compared to the FB case. The plunge/ejection actions in the scour hole appear to have generated waves/ripples diagonally downstream of the scour region. Bed shear stress contours and profiles have highlighted the significant relaxation in the DB case. The model correctly predicted the high bed shear stress region near the tip of the abutment in the FB case, where scouring process is most likely to begin. In the DB case, however, two small areas of high bed shear stress are found at the downslope and upslope regions of the scour hole. Sediment entrainments appear to be still happening in the scour but these sediments are likely prevented from escaping the scour hole by the mini recirculation zone and eventually settles down under the influence of gravity, creating a negligible net flux of sediment outside of this region. The near bed turbulent kinetic energy distributions and profiles reveal a drastic change from the FB case to DB case. In particular, the strip of high turbulent kinetic energy found in the FB case along the separated shear

6. FREE SURFACE FLOW AROUND BRIDGE ABUTMENT ON PRE-SCOUR AND EQUILIBRIUM SCOUR CONDITION

layer is completely absent in the DB case. Instead, the high tke concentrates at the scour downslope where the downward plunging flow is observed.

6. FREE SURFACE FLOW AROUND BRIDGE ABUTMENT ON
PRE-SCOUR AND EQUILIBRIUM SCOUR CONDITION

Chapter 7

Conclusions, contribution of thesis, and outlook

7.1 Conclusions

This thesis focused on using an advanced CFD model with a highly accurate free surface computation algorithm and an advanced turbulence modeling approach to explore the full dynamics of flow field around large in-stream structures which are ultimately responsible for the scour process. A refined Large Eddy Simulation (LES) code was used in conjunction with the level set method (LSM) which was specifically adopted to compute the water surface profiles around hydraulic structures. The free surface algorithm has been extensively validated, involving six flow cases which comprises of two roughness spacings that correspond to transitional and k-type roughness and three flow rates. The predictions of the LES have been shown (in Chapter 4) to be in reasonably good agreement with the experiments in terms of the free surface position and the mean streamwise velocity. The positions of the hydraulic jumps have been well represented and has thus established the credibility of the numerical method.

To achieve a faithful representation of a natural river, the computational domain employed in Chapter 5 and 6 of this thesis consists of an asymmetrical compound geometry with a parabolic main channel, two variable-length abut-

7. CONCLUSIONS AND OUTLOOK

ments with sloped sidewalls and rounded corners, and a bridge deck. To the author's knowledge, such complex computational setup has rarely been carried out in the past, less so with the prediction of the free surface.

The effect of the bridge abutment length on the turbulence structure and flow through the bridge opening has been carefully investigated and presented in Chapter 5. Experimental data has been used to validate the simulations and very convincing agreement of computed streamwise velocity profiles and water surface elevations with the measured ones has been found. Extensive analysis by means of streamwise velocity contours, 2D and 3D streamlines, isosurfaces of Q-criterion, contours of wall-normal vorticity, probability density functions, quadrant analysis, power density spectra, and water surface elevation contours has been carried out and several key differences between the long setback abutment case (LSB) and the short setback abutment case (SSB) are identified: a) in the SSB case, there are more significant meandering of the flow downstream of the abutment, of which the frequency of the meandering effect has been captured as a prominent peak in the power spectra; b) only in the LSB case, a pair of counter-rotating vortices appears near the surface in the vicinity of the left floodplain, being reflected in the free surface deformation in the form of a persistent bulging line; c) only in the SSB case, a very well-defined interface vortex is found at the interface between the main channel and the left floodplain; and d) in the SSB case, due to the higher contraction ratio, highly accelerated jet-like flow is dominating the turbulence which is fairly one-dimensional and persists over a substantial distance downstream of the abutment while convecting elongated shear layer vortices before they roll-up to become large scale vortices. These findings attempt to contribute to the design of resilient hydraulic structures especially on considering the shape and size of an abutment.

A study on the complex flows around bridge abutments placed in a compound and asymmetric channel in different scour stages, i.e. a pre-scour condition, flat bed (FB) case and an equilibrium scour condition, deformed bed (DB) case has been presented in Chapter 6. The LES-computed results for the FB case are validated against the experimental data and reasonable agreement has been found. Through 3D streamlines and contours of vertical velocity and turbulent kinetic energy, the DB case reveals an increase in the three-dimensionality of the

flow around the left abutment in the scour region when compared with the flat bed case. A tiny recirculation bubble is found inside the scour hole which completely disrupts the separated shear layer. A strong plunging/ejection motion is observed in the scour hole and, interestingly, appears to have generated waves/ripples on the water surface diagonally downstream of the scour region. Focusing on the near bed quantities, i.e. bed shear stress and near bed turbulent kinetic energy, the DB case shows a significant relaxation at the vicinity of the left abutment, indicating a drastic reduction in sediment activities.

7.2 Contributions of Thesis

The contribution of the current thesis to the field of computational fluid dynamics (CFD) and ultimately the field of hydraulics engineering are listed as below:

- from a numerical point of view, the computational domain presented in this thesis is the most realistic representation of a bridge in a natural river to date. It consists of an asymmetrical compound geometry with a parabolic main channel, variable-length spill-through abutments with sloped sidewalls and rounded corners, and a bridge deck. These hydraulic structures are represented by Lagrangian nodes using the immersed boundary method (IBM).
- the use of the level set method (LSM) has enabled the prediction of the water surface deformation around the realistic bridge abutment setup for the first time. Temporal variations of the free surface are captured and exported as animations which allow frame-to-frame analysis on the transient nature of the water surface.
- the extensive use of the LSM as an interface capturing tool to simulate various Froude number flows (up to $Fr = 1.02$ locally). A comprehensive validation case of simulating flow over square bars of different spacings and relative submergence is carried out which shows reasonably well agreement from the LES results when compared with experiment data.

- the novel way of quantifying and visualising the shedding behaviour of coherent structures springing off the abutment tip through the combination of power spectra of velocity fluctuations, wall-normal vorticity contours and water surface deformations. Such analysis allows the authors to track and visualise the life cycle of the coherent structures, starting from the vortex generation at the abutment tip, followed by the vortex being convected downstream and lastly broken down into smaller energy dissipating eddies.
- a very detailed analysis on the changes in flow dynamics around bridge abutments from pre-scour condition to equilibrium scour conditions are carried out. The unique differences between the cases are reflected on the 3D streamlines, velocity profiles, contours of bed shear stress and turbulent kinetic energy, and the water surface pattern.

7.3 Outlook

The present study has demonstrated the capability of the computational model in predicting the complex flow around bridge abutments in a realistic compound channel. In the author's view, there are promising research routes that can extend further the investigation accomplished in this thesis. To achieve a reasonable accuracy in the simulations of such large computational domains, very high computational cost has to be incurred. Therefore, local mesh refinement (LMR) can be a great addition to the current setup to increase the mesh resolution near the hydraulic structures and gradually increases the mesh size in the direction away from the structures. Ideally, the employment of mesh resolution as fine as a direct numerical simulation (DNS) is preferred.

The 'free flow' flooding scenario is the only flooding condition adopted in the present study where the maximum water depth is not perturbed by the bridge. In more extreme flooding conditions, water depth might rise to the level of the bridge or even above the bridge level, forming a 'submerged orifice' flow and 'overtopping' flow, respectively. According to experimental work by [Hong et al. \[2015\]](#), such extreme flooding scenarios result in very different scour patterns when compared with the free flow case, probably due to the presence of vertical

7. CONCLUSIONS AND OUTLOOK

contraction flow in the higher depth cases. Future works on investigating the flow field around bridge abutments under these flooding conditions would be a natural next step of the current study.

The motivation of the current thesis builds around the problem of scour formation around hydraulic structures. Thus, it is the ultimate goal of a numerical modeler to be able to accurately model the phenomena of sediment transport and essentially predict the maximum scour depth. An euler-lagrange model can be implemented to the current LES code to individually track the movement of a sediment under turbulent condition. The combination of LES with an euler-lagrange model has rarely been successfully carried out before possibly due to the expected high computational cost. Perhaps, future advancement in supercomputing power would make this feasible.

7. CONCLUSIONS AND OUTLOOK

References

- B. Alessandrini and G. Delhommeau. A multigrid velocity-pressure-free surface elevation fully coupled solver for calculation of turbulent incompressible flow around a hull. In *Twenty-First Symposium on Naval Hydrodynamics*, 1997. [34](#)
- V. Armenio. An Improved MAC Method (SIMAC) for Unsteady High-reynolds Free Surface Flows. *international Journal of Numerical Methods in Fluids*, 24(2):185–214, jan 1997. ISSN 02712091 (ISSN). doi: 10.1002/(SICI)1097-0363(19970130)24:2<185::AID-FLD487>3.0.CO;2-Q. [36](#)
- C. J. Baker. Laminar Horseshoe Vortex. *Journal of Fluid Mechanics*, 95(pt 2): 347–367, 1979. ISSN 00221120. doi: 10.1017/S0022112079001506. [10](#)
- C. J. Baker. The turbulent horseshoe vortex. *Journal of Wind Engineering and Industrial Aerodynamics*, 6(1-2):9–23, jul 1980. ISSN 01676105. doi: 10.1016/0167-6105(80)90018-5. [10](#)
- R. Bakhtyar, D. A. Barry, L. Li, D. S. Jeng, and A. Yeganeh-Bakhtiary. Modeling sediment transport in the swash zone: A review, jul 2009. ISSN 00298018. [38](#)
- A. K. Barbhuiya and S. Dey. Local scour at abutments: A review. *Sadhana*, 29(5):449–476, 2004. ISSN 0256-2499. doi: 10.1007/BF02703255. [9](#)
- J. C. Bathurst. Flow Resistance Estimation in Mountain Rivers. *Journal of Hydraulic Engineering*, 111(4):625–643, 1985. ISSN 0733-9429. doi: 10.1061/(ASCE)0733-9429(1985)111:4(625). [61](#)

REFERENCES

- B. Biglari and T. W. Sturm. Numerical Modeling of Flow Around Bridge Abutments in Compound Channel. *Journal of Hydraulic Engineering*, 124(2):156–164, 1998. [16](#)
- S. K. Bomminayuni and T. Stoesser. Turbulence Statistics in an Open-Channel Flow over a Rough Bed. *Journal of Hydraulic Engineering*, 137(11):1347–1358, 2011. ISSN 0733-9429. doi: 10.1061/(ASCE)HY.1943-7900.0000454. [31](#), [42](#)
- J. P. Boris and D. L. Book. Flux-corrected transport. I. SHASTA, a fluid transport algorithm that works. *Journal of Computational Physics*, 11(1):38–69, jan 1973. ISSN 10902716. doi: 10.1016/0021-9991(73)90147-2. [36](#)
- S. F. Bradford. Numerical Simulation of Surf Zone Dynamics. *Journal of Waterway, Port, Coastal, and Ocean Engineering*, 126(1):1–13, 2000. ISSN 0733-950X. doi: 10.1061/(ASCE)0733-950X(2000)126:1(1). [38](#)
- F. Bressan, F. Ballio, and V. Armenio. Turbulence around a scoured bridge abutment. *Journal of Turbulence*, 12(3):1–24, 2011. ISSN 14685248. doi: 10.1080/14685248.2010.534797. [12](#)
- M. Breuer. *Direkte Numerische Simulation und Large-Eddy Simulation turbulenter Strömungen auf Hochleistungsrechnern*. 2002. [xix](#), [43](#)
- J. M. Buffington. The Legend of a F. Shields. *Journal of Hydraulic Engineering*, 125:376–387, 1999. [17](#)
- A. H. Cardoso and R. Bettess. Effects of Time and Channel Geometry on Scour. *Journal of Hydraulic Engineering*, 125(4):388–399, 1999. [107](#)
- J. E. Cater and J. J. R. Williams. Large eddy simulation of a long asymmetric compound open channel. *Journal of Hydraulic Research*, 46(4):445–453, 2008. doi: 10.3826/jhr.2008.3134. [14](#)
- M. Cevheri, R. McSherry, and T. Stoesser. A local mesh refinement approach for largeeddy simulations of turbulent flows. *International Journal for Numerical Methods in Fluids*, 82(5):261–285, 2016. [42](#), [58](#)

REFERENCES

- J. Chabert and P. Engeldinger. Study of scour around bridge piers. *Rep. Prepared for the Laboratoire National d'Hydraulique*, 1956. xviii, 20, 21
- Y. C. Chang, T. Y. Hou, B. Merriman, and S. Osher. A level set formulation of Eulerian interface capturing methods for incompressible fluid flows. *Journal of Computational Physics*, 124(2):449–464, 1996. ISSN 00219991. doi: 10.1006/jcph.1996.0072. 34, 35, 38
- A. J. Chorin. Numerical Solution of the Navier-Stokes Equation. *Mathematics of computation*, 42(3):490–507, 1968. ISSN 1572-9125. doi: 10.1023/A:1021973025166. 45
- A. Chrisohoides and F. Sotiropoulos. Experimental visualization of Lagrangian coherent structures in aperiodic flows. *Physics of Fluids*, 15(3), mar 2003. ISSN 10706631. doi: 10.1063/1.1540111. 12
- E. D. Christensen. Large eddy simulation of spilling and plunging breakers. *Coastal Engineering*, 53(5-6):463–485, apr 2006. ISSN 03783839. doi: 10.1016/j.coastaleng.2005.11.001. 38
- S. E. Coleman, V. I. Nikora, S. R. McLean, and E. Schlicke. Spatially Averaged Turbulent Flow over Square Ribs. *Journal of Engineering Mechanics*, 133(2):194–204, 2007. ISSN 0733-9399. doi: 10.1061/(ASCE)0733-9399(2007)133:2(194). 55
- B. Dargahi. The turbulent flow field around a circular cylinder. *Experiments in Fluids*, 8(1-2):1–12, oct 1989. ISSN 07234864. doi: 10.1007/BF00203058. xviii, 10, 11
- W. J. Devenport and R. L. Simpson. Time-dependent and time-averaged turbulence structure near the nose of a wing-body junction. *Journal of Fluid Mechanics*, 210(23):23–55, 1990. ISSN 14697645. doi: 10.1017/S0022112090001215. 10
- S. Dey and A. K. Barbhuiya. 3D flow field in a scour hole at a wing-wall abutment. *Journal of Hydraulic Research*, 44(1):33–50, 2006. ISSN 0022-1686. doi: 10.1080/00221686.2006.9521659. 13

REFERENCES

- W. E. Dietrich and P. Whiting. Boundary shear stress and sediment transport in river meanders of sand and gravel. pages 1–50. American Geophysical Union (AGU), 1989. ISBN 0270-9600. doi: 10.1029/WM012p0001. [61](#)
- M. Dixen, B. M. Sumer, and J. Fredsoe. Numerical and experimental investigation of flow and scour around a half-buried sphere. *Coastal Engineering*, 73:84–105, 2013. ISSN 00221120. doi: 10.1017/S0022112005004507. [29](#)
- Y. Dubief and F. Delcayre. On coherent-vortex identification in turbulence. *Journal of Turbulence*, 1(January):1–22, 2000. ISSN 1468-5248. doi: 10.1088/1468-5248/1/1/011. [87](#)
- D. Enright, R. P. Fedkiw, J. H. Ferziger, and I. Mitchell. *A Hybrid Particle Level Set Method for Improved Interface Capturing*, volume 183. Academic Press, nov 2002. ISBN 0001401106. doi: 10.1006/jcph.2002.7166. [39](#)
- C. Escauriaza and F. Sotiropoulos. Lagrangian model of bed-load transport in turbulent junction flows. *Journal of Fluid Mechanics*, 666:36–76, jan 2011. ISSN 00221120. doi: 10.1017/S0022112010004192. [29](#)
- R. Ettema, T. Nakato, and M. Muste. Estimation of Scour Depth At Bridge Abutments. Technical Report January, The University of Iowa, Iowa, 2010. [xviii](#), [8](#), [9](#), [121](#)
- E. A. Fadlun, R. Verzicco, P. Orlandi, and J. Mohd-Yusof. Combined immersed-boundary finite-difference methods for three-dimensional complex flow simulations. *Journal of computational physics*, 161(1):35–60, 2000. [49](#)
- J. Farmer, L. Martinelli, and A. Jameson. A Fast Multigrid Method of Solving the Nonlinear Ship Wave Problem with a Free Surface. In *6th International Conference on Numerical Ship Hydrodynamics*, 1993. [34](#)
- J. H. Ferziger and M. Peric. *Computational Methods for Fluid Dynamics*. 2002. ISBN 3540420746. doi: 10.1016/S0898-1221(03)90046-0. [30](#), [46](#)
- C. Fischenich and M. Landers. Computing scour. *Ecosystem Management and Restoration*, (2):1–4, 2000. [20](#)

REFERENCES

- B. Fraga and T. Stoesser. Influence of bubble size, diffuser width, and flow rate on the integral behavior of bubble plumes. 121:3887–3904, 2016. ISSN 21699275. doi: 10.1002/2014JC010066. Received. [42](#)
- B. Fraga, T. Stoesser, C. C. K. Lai, and S. A. Socolofsky. A LES-based Eulerian-Lagrangian approach to predict the dynamics of bubble plumes. *Ocean Modelling*, 97:27–36, 2016. ISSN 14635003. doi: 10.1016/j.ocemod.2015.11.005. [42](#)
- S. Fukuoka. *Advances in river sediment research: proceedings of the 12th International Symposium on River Sedimentation, ISRS 2013, Kyoto, Japan, 2-5 September 2013*. 2013. ISBN 978-1-315-85658-2 978-1-138-00062-9. [29](#)
- M. Fulgosi, D. Lakehal, S. Banerjee, and V. De Angelis. Direct numerical simulation of turbulence in a sheared air-water flow with a deformable interface. *Journal of Fluid Mechanics*, 482(482):319–345, 2003. ISSN 00221120. doi: 10.1017/S0022112003004154. [35](#)
- V. R. Gopala and B. G. van Wachem. Volume of fluid methods for immiscible-fluid and free-surface flows. *Chemical Engineering Journal*, 141(1-3):204–221, 2008. ISSN 13858947. doi: 10.1016/j.cej.2007.12.035. [36](#)
- M. Griebel and M. Klitz. CLSVOF as a fast and mass-conserving extension of the level-set method for the simulation of two-phase flow problems. *Numerical Heat Transfer, Part B: Fundamentals*, 71(1):1–36, 2017. ISSN 15210626. doi: 10.1080/10407790.2016.1244400. [39](#)
- F. H. Harlow and J. E. Welch. Numerical calculation of time-dependent viscous incompressible flow of fluid with free surface. *Physics of Fluids*, 8(12):2182–2189, 1965. ISSN 10706631. doi: 10.1063/1.1761178. [35](#)
- C. W. Hirt and B. D. Nichols. Volume of fluid (VOF) method for the dynamics of free boundaries. *Journal of Computational Physics*, 39(1):201–225, jan 1981. ISSN 10902716. doi: 10.1016/0021-9991(81)90145-5. [36](#)

REFERENCES

- B. R. Hodges and R. L. Street. On Simulation of Turbulent Nonlinear Free-Surface Flows. *Journal of Computational Physics*, 151(2):425–457, may 1999. ISSN 00219991. doi: 10.1006/jcph.1998.6166. [30](#), [34](#)
- S. H. Hong. *Prediction of Clear-Water Abutment Scour Depth in Compound Channel for Extreme Hydrologic Events*. PhD thesis, Georgia Institute of Technology, dec 2012. [79](#)
- S. H. Hong, T. W. Sturm, and T. Stoesser. Clear Water Abutment Scour in a Compound Channel for Extreme Hydrologic Events. *Journal of Hydraulic Engineering*, 141(6), 2015. [75](#), [76](#), [107](#), [122](#), [132](#)
- T. Y. Hou, J. S. e. Lowengrub, and M. J. Shelley. Removing the stiffness from interfacial flows with surface tension. *J. Comput. Phys.*, 114:312–338, 1994. [34](#)
- T. Y. Hou, J. S. Lowengrub, and M. J. Shelley. Boundary Integral Methods for Multicomponent Fluids and Multiphase Materials. *Journal of Computational Physics*, 169(2):302–362, 2001. ISSN 00219991. doi: 10.1006/jcph.2000.6626. [34](#)
- B. E. Hunt. *Monitoring Scour Critical Bridges*. Transportation Research Board, 2009. ISBN 978-0-309-41665-8. doi: 10.17226/22979. [xviii](#), [3](#), [4](#)
- H. Jasak and H. Weller. Interface tracking capabilities of the inter-gamma differencing scheme. *Department of Mechanical Engineering, Imperial College of Science, Technology and Medicine*, (2):1–9, 1995. [36](#)
- M. S. Jensen, B. Juul Larsen, P. Frigaard, L. DeVos, E. D. Christensen, E. Asp Hansen, T. Solberg, B. H. Hjertager, and S. Bove. Offshore Wind Turbines situated in Areas with Strong Currents. Technical report, 2006. [17](#), [119](#)
- G. S. Jiang and C. W. Shu. Efficient implementation of weighted ENO schemes. *Journal of Computational Physics*, 126(1):202–228, jun 1996. ISSN 00219991. doi: 10.1006/jcph.1996.0130. [45](#)
- S. Kang and F. Sotiropoulos. Large-Eddy Simulation of Three-Dimensional Turbulent Free Surface Flow Past a Complex Stream Restoration Structure. *Jour-*

REFERENCES

- nal of Hydraulic Engineering*, 141(10):04015022, 2015. ISSN 0733-9429. doi: 10.1061/(ASCE)HY.1943-7900.0001034. [39](#)
- S. Kang, I. Borazjani, J. A. Colby, and F. Sotiropoulos. Numerical simulation of 3D flow past a real-life marine hydrokinetic turbine. *Advances in Water Resources*, 39:33–43, apr 2012. ISSN 03091708. doi: 10.1016/j.advwatres.2011.12.012. [49](#)
- S. Kara, T. Stoesser, and T. W. Sturm. Turbulence statistics in compound channels with deep and shallow overbank flows. *Journal of Hydraulic Research*, 50(5):482–493, 2012. ISSN 0022-1686. doi: 10.1080/00221686.2012.724194. [14](#), [76](#), [108](#)
- S. Kara, M. C. Kara, T. Stoesser, and T. W. Sturm. Free-Surface versus Rigid-Lid LES Computations for Bridge-Abutment Flow. *Journal of Hydraulic Engineering*, 141(9), 2015a. [xix](#), [13](#), [32](#), [33](#)
- S. Kara, T. Stoesser, T. W. Sturm, and S. Mulahasan. Flow dynamics through a submerged bridge opening with overtopping. *Journal of Hydraulic Research*, 53(2):186–195, 2015b. ISSN 0022-1686. doi: 10.1080/00221686.2014.967821. [xviii](#), [14](#), [38](#)
- A. Khosronejad, S. Kang, and F. Sotiropoulos. Experimental and computational investigation of local scour around bridge piers. *Advances in Water Resources*, 37:73–85, 2012. ISSN 03091708. doi: 10.1016/j.advwatres.2011.09.013. [28](#)
- J. Kim and P. Moin. Application of a fractional-step method to incompressible Navier-Stokes equations. *Journal of Computational Physics*, 59(2):308–323, jun 1985. ISSN 10902716. doi: 10.1016/0021-9991(85)90148-2. [45](#)
- G. Kirkil, S. G. Constantinescu, and R. Ettema. Coherent Structures in the Flow Field around a Circular Cylinder with Scour Hole. *Journal of Hydraulic Engineering*, 134(5):572–587, 2008. ISSN 0733-9429. doi: 10.1061/(ASCE)0733-9429(2008)134:5(572). [12](#)

REFERENCES

- M. Koken. Coherent structures around isolated spur dikes at various approach flow angles. *Journal of Hydraulic Research*, 49(6):736–743, 2011. ISSN 00221686. doi: 10.1080/00221686.2011.616316. [12](#)
- M. Koken. Coherent structures at different contraction ratios caused by two spill-through abutments. *Journal of Hydraulic Research*, pages 1–9, 2017. ISSN 00221686. doi: 10.1080/00221686.2017.1354930. [13](#), [14](#)
- M. Koken and G. Constantinescu. An investigation of the flow and scour mechanisms around isolated spur dikes in a shallow open channel: 1. Conditions corresponding to the initiation of the erosion and deposition process. *Water Resources Research*, 44(8):1–19, 2008a. ISSN 00431397. doi: 10.1029/2007WR006489. [9](#), [12](#), [28](#)
- M. Koken and G. Constantinescu. An investigation of the flow and scour mechanisms around isolated spur dikes in a shallow open channel: 2. Conditions corresponding to the final stages of the erosion and deposition process. *Water Resources Research*, 44(8), 2008b. ISSN 00431397. doi: 10.1029/2007WR006489. [28](#)
- M. Koken and G. Constantinescu. An investigation of the dynamics of coherent structures in a turbulent channel flow with a vertical sidewall obstruction. *Physics of Fluids*, 21(8), 2009. doi: 10.1063/1.3207859. [12](#), [32](#)
- M. Koken and G. Constantinescu. Flow and turbulence structure around a spur dike in a channel with a large scour hole. *Water Resources Research*, 47(12): 1–19, 2011. ISSN 00431397. doi: 10.1029/2011WR010710. [12](#), [28](#)
- M. Koken and G. Constantinescu. Flow and Turbulence Structure around Abutments with Sloped Sidewalls. *Journal of Hydraulic Engineering*, 140(7): 04014031, 2014. ISSN 0733-9429. doi: 10.1061/(ASCE)HY.1943-7900.0000876. [12](#), [14](#)
- M. Koken and M. Gogus. Effect of spur dike length on the horseshoe vortex system and the bed shear stress distribution. *Journal of Hydraulic Research*, 53(2):196–206, mar 2015. ISSN 00221686. doi: 10.1080/00221686.2014.967819. [12](#)

REFERENCES

- S. Komori, R. Nagaosa, Y. Murakami, S. Chiba, K. Ishii, and K. Kuwahara. Direct numerical simulation of three-dimensional openchannel flow with zero-shear gas-liquid interface. *Physics of Fluids A: Fluid Dynamics*, 5(1):115–125, 1993. ISSN 0899-8213. doi: 10.1063/1.858797. [31](#)
- R. T. F. Kwan and B. W. Melville. Local scour and flow measurements at bridge abutments. *Journal of Hydraulic Research*, 32(5):661–673, 1994. ISSN 0022-1686. doi: 10.1080/00221689409498707. [9](#), [12](#)
- K. Lam and S. Banerjee. On the condition of streak formation in a bounded turbulent flow. *Physics of Fluids A: Fluid Dynamics*, 4(2):306–320, 1992. ISSN 08998213. doi: 10.1063/1.858306. [31](#), [32](#)
- E. M. Laursen. An analysis of relief bridge scour. *Journal of the Hydraulics Division*, 1963. [22](#), [107](#)
- S. O. Lee and T. W. Sturm. Effect of Sediment Size Scaling on Physical Modeling of Bridge Pier Scour. *Journal of Hydraulic Engineering*, 135(10):793–802, 2009. ISSN 0733-9429. doi: 10.1061/(ASCE)HY.1943-7900.0000091. [20](#)
- A. Leonard. Energy Cascade in Large-Eddy Simulations of Turbulent Fluid Flows. *Turbulent Diffusion in Environmental Pollution Proceedings of a Symposium held at Charlottesville*, Volume 18,:237–248, jan 1975. ISSN 00652687. doi: [http://dx.doi.org/10.1016/S0065-2687\(08\)60464-1](http://dx.doi.org/10.1016/S0065-2687(08)60464-1). [41](#)
- S. Leonardi, P. Orlandi, R. J. Smalley, L. Djenidi, and R. A. Antonia. Direct numerical simulations of turbulent channel flow with transverse square bars on one wall. *Journal of Fluid Mechanics*, 491(491):229–238, 2003. ISSN 00221120. doi: 10.1017/S0022112003005500. [61](#)
- C. Lin, J. Han, C. Bennett, and R. L. Parsons. Case History Analysis of Bridge Failures due to Scour. *Climatic Effects on Pavement . . .*, pages 1–13, 2014. [3](#)
- Y. Liu, T. Stoesser, H. Fang, A. Papanicolaou, and A. G. Tsakiris. Turbulent flow over an array of boulders placed on a rough, permeable bed. *Computers and Fluids*, 158:120–132, 2016. ISSN 00457930. doi: 10.1016/j.compfluid.2017.05.023. [42](#)

REFERENCES

- J. Longo, F. Stern, and Y. Toda. Mean-flow measurements in the boundary layer and wake and wave field of a Series 60 $C_b = 0.6$ ship model - Part 2: Scale effects on near field wave patterns and comparisons with inviscid theory. *Journal of Ship Research*, 37(1):16–24, 1993. ISSN 00224502. [34](#)
- S. S. Lu and W. W. Willmarth. Measurements of the structure of the Reynolds stress in a turbulent boundary layer. *Journal of Fluid Mechanics*, 60(03):481, 1973. ISSN 0022-1120. doi: 10.1017/S0022112073000315. [94](#)
- P. Lubin, S. Glockner, O. Kimmoun, and H. Branger. Numerical study of the hydrodynamics of regular waves breaking over a sloping beach. *European Journal of Mechanics, B/Fluids*, 30(6):552–564, nov 2011. ISSN 09977546. doi: 10.1016/j.euromechflu.2011.01.001. [38](#)
- S. McKee, M. F. Tomé, V. G. Ferreira, J. A. Cuminato, A. Castelo, F. S. Sousa, and N. Mangiavacchi. The MAC method. *Computers and Fluids*, 37(8):907–930, 2008. ISSN 00457930. doi: 10.1016/j.compfluid.2007.10.006. [36](#)
- R. McSherry, K. V. Chua, T. Stoesser, and S. Mulahasan. Free surface flow over square bars at intermediate relative submergence. *Journal of Hydraulic Research*, pages 1–19, 2018. ISSN 0022-1686. doi: 10.1080/00221686.2017.1413601. [42](#)
- B. W. Melville. Local scour at bridge piers. *Journal of Hydraulic Engineering*, 118(4):615–631, 1992. ISSN 1753-7789. doi: 10.1680/iicep.1989.2004. [107](#)
- B. W. Melville. Pier and Abutment Scour: Integrated Approach. *Journal of Hydraulic Engineering*, 123(2):125–136, 1997. ISSN 0733-9429. doi: 10.1061/(ASCE)0733-9429(1998)124:7(769). [9](#)
- B. W. Melville and S. Coleman. *Bridge Scour*. 2000. [xviii](#), [20](#), [22](#), [24](#), [27](#)
- T. Ménard, S. Tanguy, and A. Berlemont. Coupling level set/VOF/ghost fluid methods: Validation and application to 3D simulation of the primary break-up of a liquid jet. *International Journal of Multiphase Flow*, 33(5):510–524, may 2007. ISSN 03019322. doi: 10.1016/j.ijmultiphaseflow.2006.11.001. [39](#)

REFERENCES

- E. Meyer-Peter and R. Müller. Formulas for Bed-Load Transport. *Proceedings of the 2nd Meeting of the International Association of Hydraulic Research*, pages 39–64, 1948. doi: 1948-06-07. [28](#)
- H. Miyata, T. Sato, and N. Baba. Difference solution of a viscous flow with free-surface wave about an advancing ship. *Journal of Computational Physics*, 72(2):393–421, oct 1987. ISSN 0021-9991. doi: 10.1016/0021-9991(87)90090-8. [34](#)
- H. Miyata, M. Zhu, and O. Watanabe. Numerical Study on a Viscous Flow with Free Surface Waves about a Ship in Steady Straight Course by a Finite Volume Method. *Jnl. Ship Research*, 36(4), 1992. [34](#)
- R. Morales and R. Ettema. Insights from Depth-Averaged Numerical Simulation of Flow at Bridge Abutments in Compound Channels. *Journal of Hydraulic Engineering*, 139(5):470–481, 2013. ISSN 0733-9429. doi: 10.1061/(ASCE)HY.1943-7900.0000693. [14](#)
- B. D. Nichols and C. W. Hirt. Calculating three-dimensional free surface flows in the vicinity of submerged and exposed structures. *Journal of Computational Physics*, 12(2):234–246, feb 1973. ISSN 10902716. doi: 10.1016/S0021-9991(73)80013-0. [34](#)
- F. Nicoud and F. Ducros. Subgrid-scale stress modelling based on the square of the velocity gradient tensor. *Flow, turbulence and Combustion*, 62(3):183–200, 1999. [42](#)
- V. Nikora, D. Goring, I. McEwan, and G. Griffiths. Spatially Averaged Open-Channel Flow over Rough Bed. *Journal of Hydraulic Engineering*, 127(2):123–133, 2001. ISSN 0733-9429. doi: 10.1061/(ASCE)0733-9429(2001)127:2(123). [60](#)
- W. F. Noh and P. Woodward. SLIC (Simple Line Interface Calculation). In *Fifth International Conference on Numerical Methods in Fluid Dynamics*, pages 330–340. Springer, Berlin, Heidelberg, 1976. ISBN 978-3-540-08004-6. doi: 10.1007/3-540-08004-X_336. [36](#)

REFERENCES

- S. Osher and R. Fedkiw. *Level Set Methods and Dynamic Implicit Surfaces*, volume 153 of *Applied Mathematical Sciences*. Springer New York, New York, NY, 2003. ISBN 978-1-4684-9251-4. doi: 10.1007/b98879. [48](#)
- S. Osher and J. A. Sethian. Fronts propagating with curvature-dependent speed: Algorithms based on Hamilton-Jacobi formulations. *Journal of Computational Physics*, 79(1):12–49, nov 1988. ISSN 10902716. doi: 10.1016/0021-9991(88)90002-2. [38](#), [47](#)
- P. Ouro, C. A. Wilson, P. Evans, and A. Angeloudis. Large-eddy simulation of shallow turbulent wakes behind a conical island. *Physics of Fluids*, 29(12), 2017. doi: 10.1063/1.5004028. [42](#)
- J. Paik and F. Sotiropoulos. Coherent structure dynamics upstream of a long rectangular block at the side of a large aspect ratio channel. *Physics of Fluids*, 17(11):1–14, 2005. ISSN 10706631. doi: 10.1063/1.2130743. [12](#), [32](#)
- Y. Pan and S. Banerjee. A numerical study of free-surface turbulence in channel flow. *Physics of Fluids*, 7(7):1649–1664, 1995. ISSN 10706631. doi: 10.1063/1.868483. [31](#)
- D. Peng, B. Merriman, S. Osher, H. Zhao, and M. Kang. A PDE-Based Fast Local Level Set Method. *Journal of Computational Physics*, 155(2):410–438, 1999. ISSN 00219991. doi: 10.1006/jcph.1999.6345. [39](#)
- C. S. Peskin. Flow patterns around heart valves: A numerical method. *Journal of Computational Physics*, 10(2):252–271, 1972. ISSN 10902716. doi: 10.1016/0021-9991(72)90065-4. [49](#)
- C. Polatel. Large-scale roughness effect on free-surface and bulk flow characteristics in open-channel flows. *Civil & Environmental Engng.*, PhD(July):208, 2006. [37](#)
- RAIB. Rail Accident Report: Failure of Bridge RDG1 48 between Whitton and Feltham. Technical Report November 2009, 2010. [xviii](#), [2](#)
- H. C. Raven. A Solution Method for the Nonlinear Ship Wave Resistance Problem. Technical report, 1996. [34](#)

REFERENCES

- H. C. Raven and E. H. van Brummelen. A new approach to computing steady free-surface viscous flow problems. *1st MARNET-CFD workshop*, 1999. [34](#)
- W. Rodi, G. Constantinescu, and T. Stoesser. *Large-eddy simulation in hydraulics*. Crc Press, 2013. [41](#), [42](#), [45](#)
- G. Russo and P. Smereka. A Remark on Computing Distance Functions. *Journal of Computational Physics*, 163(1):51–67, sep 2000. ISSN 00219991. doi: 10.1006/jcph.2000.6553. [39](#)
- M. Sanjou and I. Nezu. Large eddy simulation of compound open-channel flows with emergent vegetation near the floodplain edge. *Journal of Hydrodynamics*, 22(5):582–586, 2010. doi: 10.1016/S1001-6058(09)60256-0. [37](#)
- J. Shi, T. G. Thomas, and J. J. Williams. Free-surface effects in open channel flow at moderate Froude and Reynold’s numbers. *Journal of Hydraulic Research*, 38(6):465–474, 2000. ISSN 00221686. doi: 10.1080/00221680009498300. [37](#)
- A. Shirole and R. Holt. Planning for a comprehensive bridge safety assurance program. In *Transport Research Record*, volume 1290, pages 137–142, 1991. ISBN 0309050677. [3](#)
- K. M. Singh, N. D. Sandham, and J. J. R. Williams. Numerical Simulation of Flow over a Rough Bed. *Journal of Hydraulic Engineering*, 133(4):386–398, 2007. ISSN 0733-9429. doi: 10.1061/(ASCE)0733-9429(2007)133:4(386). [31](#)
- F. Sotiropoulos and X. Yang. Immersed boundary methods for simulating fluid-structure interaction, feb 2014. ISSN 03760421. [49](#)
- F. S. Sousa, N. Mangiavacchi, L. G. Nonato, A. Castelo, M. F. Tomé, V. G. Ferreira, J. A. Cuminato, and S. McKee. A front-tracking/front-capturing method for the simulation of 3D multi-fluid flows with free surfaces. *Journal of Computational Physics*, 198(2):469–499, 2004. ISSN 00219991. doi: 10.1016/j.jcp.2004.01.032. [36](#)
- T. Stoesser. Physically Realistic Roughness Closure Scheme to Simulate Turbulent Channel Flow over Rough Beds within the Framework of LES. *Jour-*

REFERENCES

- Journal of Hydraulic Engineering*, 136(10):812–819, 2010. ISSN 0733-9429. doi: 10.1061/(ASCE)HY.1943-7900.0000236. [42](#)
- T. Stoesser and V. Nikora. Flow structure over square bars at intermediate submergence: Large Eddy Simulation study of bar spacing effect. *Acta Geophysica*, 56(3):876–893, 2008. [31](#), [42](#)
- T. Stoesser and W. Rodi. LES of bar and rod roughened bed channel flow. In *The 6th. International Conference*, 2004. [54](#), [67](#)
- T. Stoesser, R. McSherry, and B. Fraga. Secondary Currents and Turbulence over a Non-Uniformly Roughened Open-Channel Bed. *Water*, 7(9):4896–4913, 2015. [42](#)
- T. W. Sturm. *Open Channel Hydraulic*. Text book series in Water resources and Environmental Engineering, 2001. [xviii](#), [17](#), [18](#), [22](#), [119](#)
- T. W. Sturm. Scour around Bankline and Setback Abutments in Compound Channels. *Journal of Hydraulic Engineering*, 132(1):21–32, 2006. ISSN 07339429. doi: 10.1061/(ASCE)0733-9429(2006)132:1(21). [22](#)
- T. W. Sturm and N. S. Janjua. Clear-water Scour Around Abutments in Floodplains. *Journal of Hydraulic Engineering*, 120(8):956–972, 1994. [22](#)
- T. W. Sturm, R. Ettema, and B. W. Melville. Evaluation of Bridge-Scour Research: Abutment and Contraction Scour Processes and Prediction. *NCHRP Web Document*, 27(September):106, sep 2011. doi: 10.17226/22841. [xviii](#), [22](#), [23](#), [24](#), [25](#)
- J. Suh, J. Yang, and F. Stern. The effect of air-water interface on the vortex shedding from a vertical circular cylinder. *Journal of Fluids and Structures*, 27(1):1–22, 2011. ISSN 08899746. doi: 10.1016/j.jfluidstructs.2010.09.001. [38](#)
- B. M. Sumer and J. Fredsøe. *The Mechanics of Scour in the Marine Environment*, volume 17 of *Advanced Series on Ocean Engineering*. WORLD SCIENTIFIC, apr 2002. ISBN 978-981-02-4930-4. doi: 10.1142/4942. [9](#)

REFERENCES

- M. Sussman and E. G. Puckett. A Coupled Level Set and Volume-of-Fluid Method for Computing 3D and Axisymmetric Incompressible Two-Phase Flows. *Journal of Computational Physics*, 162(2):301–337, 2000. ISSN 00219991. doi: 10.1006/jcph.2000.6537. [39](#)
- M. Sussman, P. Smereka, and S. Osher. A Level Set Approach for Computing Solutions to Incompressible Two-Phase Flow, 1994. ISSN 00219991. [39](#), [48](#)
- T. G. Thomas, D. C. Leslie, and J. J. Williams. Free surface simulations using a conservative 3D code. *Journal of Computational Physics*, 116(1):52–68, 1995. ISSN 00219991. doi: 10.1006/jcph.1995.1005. [37](#)
- Y. Toda, F. Stern, and J. Longo. Mean-flow measurements in the boundary layer and wake and wave field of a Series 60 $C_b = 0.6$ ship model - Part 1: Froude numbers 0.16 and 0.316. *Journal of Ship Research*, 1992. [34](#)
- M. F. Tomé, A. C. Filho, J. A. Cuminato, N. Mangiavacchi, and S. Mckee. GENSMAC3D: A numerical method for solving unsteady three-dimensional free surface flows. *International Journal for Numerical Methods in Fluids*, 37(7):747–796, dec 2001. ISSN 02712091. doi: 10.1002/flid.148. [36](#)
- O. Ubbink. *Numerical prediction of two fluid systems with sharp interfaces*. PhD thesis, 1997. [36](#)
- M. Uhlmann. An immersed boundary method with direct forcing for the simulation of particulate flows. *Journal of computational physics*, 209(2):448–476, 2005. [49](#)
- E. H. Van Brummelen, H. C. Raven, and B. Koren. Efficient Numerical Solution of Steady Free-Surface Navier Stokes Flow. *Journal of Computational Physics*, 137:120–137, 2001. doi: 10.1006/jcph.2001.6880. [34](#)
- A. E. P. Veldman and M. E. S. Vogels. Axisymmetric liquid sloshing under low-gravity conditions. *Acta Astronautica*, 11(10-11):641–649, oct 1984. ISSN 00945765. doi: 10.1016/0094-5765(84)90048-1. [36](#)

REFERENCES

- J. A. Viecegli. A computing method for incompressible flows bounded by moving walls. *Journal of Computational Physics*, 8(1):119–143, aug 1971. ISSN 10902716. doi: 10.1016/0021-9991(71)90039-8. [36](#)
- G. Voulgaris and J. H. Trowbridge. Evaluation of the acoustic doppler velocimeter (ADV) for turbulence measurements. *J. Atmospheric and Oceanic Technology*, 15(2):272–289, 1998. ISSN 0739-0572. doi: 10.1175/1520-0426(1998)015<0272:EOTADV>2.0.CO;2. [76](#)
- Z. Wang, J. Yang, and F. Stern. Comparison of Particle Level Set and CLSVOF Methods for Interfacial Flows. In *46th AIAA Aerospace Sciences Meeting and Exhibit*, Reston, Virginia, jan 2008. American Institute of Aeronautics and Astronautics. ISBN 978-1-62410-128-1. doi: 10.2514/6.2008-530. [39](#)
- Z. Wang, J. Suh, J. Yang, and F. Stern. Sharp Interface LES of Breaking Waves by an Interface Piercing Body in Orthogonal Curvilinear Coordinates. *50th AIAA Aerospace Sciences Meeting including the New Horizons Forum and Aerospace Exposition*, jan 2012. doi: 10.2514/6.2012-1111. [39](#)
- K. Wardhana and F. C. Hadipriono. Analysis of Recent Bridge Failures in the United States. *Journal of Performance of Constructed Facilities*, 17(3):144–150, 2003. ISSN 0887-3828. doi: 10.1061/(ASCE)0887-3828(2003)17:3(144). [3](#)
- Y. Watanabe and H. Saeki. Three-Dimensional Large Eddy Simulation of Breaking Waves. *Coastal Engineering Journal*, 41(3-4):281–301, sep 1999. ISSN 2166-4250. doi: 10.1142/S0578563499000176. [38](#)
- Y. Watanabe and H. Saeki. Velocity field after wave breaking. *International Journal for Numerical Methods in Fluids*, 39(7):607–637, jul 2002. ISSN 02712091. doi: 10.1002/flf.345. [38](#)
- Z. Xie, B. Lin, and R. A. Falconer. Turbulence characteristics in free-surface flow over two-dimensional dunes. *Journal of Hydro-Environment Research*, 8(3):200–209, 2014. ISSN 15706443. doi: 10.1016/j.jher.2014.01.002. [37](#), [38](#)

REFERENCES

- M. S. Yalin and E. Karahan. Inception of Sediment Transport. *Journal of the Hydraulics Division*, 105(11):1433–1443, 1979. [17](#)
- D. Youngs. Time-Dependent Multi- material Flow with Large Fluid Distortion. *Numerical Methods for Fluid Dynamics*, (October):273–285, 1982. [36](#)
- W. Yue, C.-L. Lin, and V. C. Patel. Coherent Structures In Open-Channel Flows Over a Fixed Dune. *Journal of Fluids Engineering*, 127(5):858, sep 2005. ISSN 00982202. doi: 10.1115/1.1988345. [38](#)
- H. Zhang, H. Mizutani, H. Nakagawa, and K. Kawaike. Euler-Lagrange model for local scour and grain size variation around a spur dyke. *International Journal of Multiphase Flow*, 68:59–70, 2015. ISSN 03019322. doi: 10.1016/j.ijmultiphaseflow.2014.10.003. [29](#)